A lower limit on the magnetic field strength at the shock front of the supernova remnant HESS J1731-347

Masterarbeit

eingereicht von

Sebastian Rottenanger

Eberhard Karls Universität Tübingen
Mathematisch-Naturwissenschaftliche Fakultät
Kepler Center for Astro and Particle Physics
Institut für Astronomie und Astrophysik
Abteilung Hochenergieastrophysik

März 2015

Erklärung

Hiermit versichere ich, dass die vorliegende Arbeit von mir selbständig verfasst wurde und keine anderen als die angegebenen Hilfsmittel und Quellen benutzt wurden. Alle wörtlich oder sinngemäß aus anderen Werken übernommenen Aussagen sind als solche gekennzeichnet. Die vorliegende Arbeit war bisher weder vollständig noch in wesentlichen Teilen Gegenstand eines anderen Prüfungsverfahrens und die Arbeit wurde weder vollständig noch in wesentlichen Teilen bereits veröffentlicht.

Ort, Datum	Sebastian Rottenanger

Abstract

In this master thesis a lower limit for the magnetic field strength at the shock front of the supernova remnant HESS J1731-347 was determined by studying two synchrotron shock filaments observed in the X-ray image of the source. A limit higher than 12 μG would give evidence for hadronic cosmic ray acceleration at the shock front. The image used for the analysis was taken in April 2008 with the *Chandra* X-ray telescope. After a careful reduction of the data, which included background reduction, the core of the analysis was to fit the emission following a model expected when energy losses of the electrons, due to synchrotron emission, are taken into account. To study the influence of the point spread function (PSF) on the emission profiles, PSF simulations were done with a ray trace simulation software specific of Chandra. The obtained PSF were fitted two-dimensional. Best fit results show that the PSF is several times smaller than the studied filaments. To determine the morphology of the X-ray structures also a two-dimensional fit was performed. The results indicate that one of the filaments, the north-west (NW) filament, is placed at the outer shock front as part of a circle with its origin at the central compact object (CCO). The results of the two-dimensional fit were used as input coordinates for a one-dimensional fit of the emission profiles projected along the filament, based on an exponential function. The best fit results for the filament near the CCO include the possibility of a very wide emission profile with a magnetic field strength lower than 12 μG. Results for this filament are therefore not conclusive. To improve the estimate on the the filament width, the NW filament at the outer shock front was modeled with a fit function which considers that the observed surface brightness of the remnant has to be a projection of the radial emissivity. With that, the width of the intrinsic profile at the source is only $\sim$1/7 of the observed width. The best fit results give a width of $10.35^{+1.69}_{-1.39}$ arc seconds. Using this result, a lower limit on the magnetic field at the shock front was calculated with different models including both the diffusion and convection motion of electrons at the shock front. The results show that magnetic field amplification is most likely at work in HESS J1731-347 and depending on the shock velocity, on the distance of the source and the model used, the magnetic field could be in the range of at least more than 50 μG.

Zusammenfassung

In dieser Masterarbeit wurde eine Untergrenze für die Magnetfeldstärke an der Schockfront des Supernova-Überrestes HESS J1731-347 bestimmt, indem zwei Synchrotron Schockfilamente im Röntgenbild der Quelle untersucht wurden. Eine Grenze höher als 12 μG würde Hinweise darauf geben, dass an der Schockfront hadronische kosmische Strahlung beschleunigt wird. Das Bild, welches für die Analyse benutzt wurde, entstand im April 2008 mit dem Röntgenteleskop Chandra. Nach einer sorgfältigen Datenreduktion, in der auch die Hintergrundstrahlung reduziert wurde, war der Hauptteil der Analyse die Emission mit einem Modell zu fitten, welches erwartet wird, wenn die Elektronen Energie durch Synchrotronstrahlung verlieren. Um den Einfluss der Punktspreizfunktion (PSF) auf die Emissionsprofile zu untersuchen, wurden PSF-Simulationen mit einer für Chandra spezifischen Raytracing Software durchgeführt. Die erhaltenen PSF wurden zweidimensional gefittet. Die besten Fit-Ergebnisse zeigen, dass die PSF um ein vielfaches kleiner ist als die untersuchten Filamente. Zur Bestimmung der Morphologie der Röntgenstrukturen wurde ebenfalls ein zweidimensionaler Fit durchgeführt. Die Ergebnisse deuten darauf hin, dass sich eines der Filamente, das Nordwest (NW) Filament, an der äußeren Schockfront befindet, als Teil eines Kreises, dessen Zentrum bei dem Central Compact Object (CCO) liegt. Die Ergebnisse des zweidimensionalen Fits wurden als Koordinaten für einen eindimensionalen Fit der entlang der Filamente projizierten Emissionsprofile benutzt, welcher auf einer exponentiellen Funktion basiert. Die besten Fit-Ergebnisse für das Filament nahe des CCO beinhalten die Möglichkeit eines sehr breiten Emissionsprofils mit einer Magnetfeldstärke geringer als 12 μG. Die Ergebnisse für dieses Filament sind daher nicht sehr aussagekräftig. Um die Abschätzung der Filamentbreite zu verbessern, wurde das NW Filament an der äußeren Schockfront mit einer Funktion modelliert, welche berücksichtigt, dass die beobachtete Oberflächenhelligkeit des Überrests eine Projektion der radialen Emissivität sein muss. Damit ist die eigentliche Breite des Profils in der Quelle nur $\sim$1/7 der beobachteten Breite. Die besten Fit-Ergebnisse ergeben eine Breite von $10.35^{+1.69}_{-1.39}$ Bogensekunden. Unter Benutzung dieses Ergebnisses wurde eine Untergrenze für die Magnetfeldstärke an der Schockfront mit verschiedenen Modellen berechnet, welche sowohl die Diffusions- als auch die Konvektions-Bewegung der Elektronen an der Schockfront beinhalten. Die Ergebnisse zeigen, dass sehr wahrscheinlich Magnetfeld-Verstärkung in HESS J1731-347 stattfindet und abhängig von der Schockgeschwindigkeit, dem Abstand zur Quelle und dem benutzen Modell, sich das Magnetfeld mindestens im Bereich von mehr als 50 μG befinden könnte.

Contents

1 Introduction and Overview **1**

2 The studied Source: HESS J1731-347 **4**

3 The Chandra X-ray telescope **6**
3.1 CCD X-ray detectors . . . 6
3.2 Chandra . . . 8
3.2.1 HRMA . . . 9
3.2.2 ACIS . . . 10

4 Theoretical Aspects **14**
4.1 Supernovae . . . 14
4.1.1 Supernova Type II . . . 15
4.1.2 Supernova Type I . . . 16
4.2 Supernova Remnants . . . 16
4.3 Diffusive Shock Acceleration . . . 17
4.4 Synchrotron Radiation . . . 19
4.5 Diffusion of electrons in a fully ionized plasma . . . 21
4.6 Cosmic Rays . . . 22
4.7 Synchrotron Shock Filaments . . . 24
4.8 Point Spread Function . . . 25
4.9 Exposure Map . . . 27
4.10 Background in Observations . . . 28

5 Data Reduction **30**
5.1 Background Reduction . . . 30
5.2 Exposure Correction . . . 36
5.3 Simulating the PSF . . . 40

6 Fitting of the Filaments **46**
6.1 2D fitting with Sherpa . . . 46
6.2 Fit with Convolution of an Exponential Profile and the PSF . . . 53
6.3 Projection Effect on the Image . . . 60

7 Results **68**
7.1 A lower limit on the magnetic field strength at the shock front . . . 68

8 Discussion and Outlook **75**

List of Figures

2.1 Early *HESS* and *ROSAT* images of HESS J1731-347 . . . 4
2.2 HESS J1731-347 in radio, X-ray and TeV . . . 5

3.1 The grade system for detected events with *Chandra* . . . 8
3.2 The *Chandra* space telescope . . . 9
3.3 The *High Resolution Mirror Array* of *Chandra* . . . 10
3.4 The *HRMA* off-axis PSF . . . 10
3.5 *ACIS* detector in the focal plane . . . 12
3.6 *ACIS* effective area . . . 13
3.7 The *Science Instrument Module* . . . 13

4.1 Onion structure of a 25 solar mass star . . . 15
4.2 Evolution stages of a shell-like supernova remnant . . . 17
4.3 Diffusive shock acceleration . . . 18
4.4 Motion of a charged particle in a magnetic field . . . 20
4.5 Cosmic ray spectrum . . . 23
4.6 Extensive air shower . . . 24
4.7 X-ray image of Cas A and plot of theoretical shock filament emission profile . . . 26
4.8 Airy function approximated with a Gaussian and the Rayleigh limit . . . 27
4.9 Normalized particle background spectra for different telescopes . . . 29

5.1 *Chandra* counts image of HESS J1731-347 . . . 31
5.2 Spectra extracted from the *Chandra* image of HESS J1731-347 and from the 2005 *Blank Sky* background image . . . 33
5.3 Excluded 5x5 grade events . . . 35
5.4 Background image multiplied by scaling factor . . . 36
5.5 Dithering pattern of *Chandra* during an observation . . . 37
5.6 Weighted exposure map . . . 37
5.7 Two color *Chandra* image of HESS J1731-347 . . . 38
5.8 Fitted spectrum of HESS J1731-347 . . . 39
5.9 Exposure corrected and uncorrected image of HESS J1731-347 in comparison . . . 40
5.10 Marked position for the PSF simulations . . . 42
5.11 *MARX* simulations of the PSF . . . 42
5.12 Fit of simulated PSF for a point-like source . . . 43
5.13 Principle of fitting the emission profile of the filaments . . . 44
5.14 Fit of simulated PSF for a circular source . . . 44

6.1 Filaments selected for two dimension fit . . . 48

6.2 Selected fit regions for two dimensional fit in *Sherpa* 49
6.3 Two dimensional fits of two shock filaments 52
6.4 Fit of the average background in the 2005 *Blank Sky* background image 57
6.5 One dimensional fit of the filament near the CCO, using a convolution with the PSF . . . 58
6.6 One dimensional fit of the NW filament, using a convolution with the PSF 59
6.7 Projection of 3D SNR on image 60
6.8 Effect of summing up a filament with the wrong geometrical model 61
6.9 Comparison of simulated and measured emission profiles for the NW filament 63
6.10 NW filament emission profile fitted with function considering the projection 64
6.11 peak of NW filament emission profile fitted with function considering the projection . . . 65
6.12 Comparison of best fit profile with PSF 67

7.1 Lower limit for the magnetic field strength at the shock front of HESS J1731-347 if the distance is 3.2 kpc 71
7.2 Lower limit for the magnetic field strength at the shock front of HESS J1731-347 if the distance is 5.2 kpc 73

Chapter 1

Introduction and Overview

At the beginning of the 20th century cosmic rays were first discovered when it was realized that there is other radiation on earth than natural radioactivity. This was discovered when electroscopes discharged in an environment shielded from the natural radioactivity on earth. The next evidence was found in 1912 and 1913 when Hess and Kolhörster measured the ionization of the atmosphere in a balloon at different altitudes (Hess 1912). The results showed that the ionization increases with altitude, clearly suggesting a radiation component from outside the earth. Results from measurements during a total eclipse excluded the possibility for the sun to be the source. In the 1920s Millikan named the particles "cosmic rays" and proposed that they were γ-rays as by-product of fusion of hydrogen. However, in 1929 an experiment by Kolhörster and Bothe, which includes two coincidence counters with a thick gold plate between them, showed events in both counters (Bothe & Kolhörster 1929). This is only possible if the cosmic rays are charged particles.

There are different sources considered as potential origins of cosmic rays. Active galactic nuclei (AGN), super massive black holes in the center of galaxies, are considered sources for cosmic rays from outside the galaxy and for the very high energy cosmic rays up to 10^{21} eV. Pulsars, pulsating neutron stars with a very high magnetic field, are also considered sources of galactic cosmic rays. For galactic cosmic rays it was already calculated in 1934 by Baade and Zwicky (Baade & Zwicky 1934) that supernovae can provide enough energy output to explain the cosmic ray energy density in the galaxy. The acceleration process expected for this is the second order Fermi acceleration, named after the physicist Enrico Fermi. It is explained in more detail in section 4.3 and describes how particles are accelerated by diffusing through the shock and back, in a stochastic process.

The galactic cosmic rays with energies up to the knee at about 10^{15} eV in the cosmic ray spectrum (see section 4.6) are then expected to come from supernova remnants (SNR). Only a few bright non-thermal shell-type TeV SNRs have been discovered up to now (Yang, Rui-zhi et al. 2014). One of these is HESS J1731-347, which was discovered in 2008 as a TeV source and is described in more detail in chapter 2. The fact that shell-type SNRs are observed in TeV γ-rays is evidence for particle acceleration.

There are two different possibilities for the origin of these γ-ray photons: the so called leptonic and the hadronic scenarios (as for example discussed in case of HESS J1731-347 in Yang, Rui-zhi et al. (2014)). In the leptonic case, the γ-rays originate from inverse compton scattering of cosmic microwave background photons through electron-photon scattering. For very high electron cosmic ray energies in the range of TeV, the scattering is suppressed by the Klein-Nishina-effect. For a high magnetic field strength at the shock front of the SNR the leptonic case is also suppressed because of strong synchrotron cooling of the electrons (Tanaka et al. 2008).

In the hadronic scenario the accelerated hadrons, mainly protons, interact through inelastic scattering with the surrounding nuclei and produce π^0 which then decay into γ-rays. To accelerate protons at the

SNR shock front to TeV energies, the magnetic field there has to be amplified to values significant higher than 12μG from the compression of the interstellar medium because of the shock. If not, the protons will escape from the acceleration region because of a too big gyroradius $\propto 1/B$.
As explained above, the magnetic field at the shock front plays an important role in the acceleration of cosmic ray particles in a SNR. Therefore in this work a lower limit of the magnetic field strength at the shock front of the SNR HESS J1731-347 is calculated using X-ray synchrotron emission at the shock front. This will help to characterize the conditions for the acceleration of particles at the shock front and could help to create spectral energy distribution models for the γ-ray spectrum including the leptonic and hadronic scenarios. Furthermore, the limit will give evidence if the acceleration of hadronic particles is possible in HESS J1731-347 at all. How this limit is determined together with an outline of the work is now described.
In chapter 2 the studied source HESS J1731-347 is discussed. In chapter 3 the *Chandra* X-ray telescope is presented together with the X-ray CCD detectors that are used in it. Some important concepts used in the analysis are introduced and discussed.
For the understanding of the topic, of the analysis and of the main results, several specific topics are introduced in chapter 4: First the supernova itself and then the remaining supernova remnant are discussed to explain the origin of HESS J1731-347 and how it will evolve with time. Then the diffusive shock acceleration of particles is explained to show how cosmic rays can reach TeV energies before escaping from the shock region. How the observed X-ray synchrotron emission in HESS J1731-347 is produced is also presented, using electrodynamics. The process of diffusion of charged particles in a magnetic field plays an important role in the calculation of the limit on the magnetic field strength, therefore it is explained together with the case of a turbulent magnetic field. Then again cosmic rays are discussed, but this time more emphasis is put on their properties. The last part of chapter 4 is dedicated to four important topics for the data analysis. The theory on synchrotron shock filaments is discussed, what shape the emission profile should have and how it can be used to calculate a lower limit on the magnetic field strength at the shock front. Also the origin of the point spread function (PSF) which broadens the image structures is discussed and how it can be approximated by a gaussian function. Then the exposure map used to exposure correct the image in the analysis part is discussed theoretically by showing how the conversion from counts to flux is performed. Since a background reduction is done in the image in the analysis part, the different background influences in an observation are also discussed.
The data reduction for preparing the study of the spatial properties of the *Chandra* image of HESS J1731-347 is presented in chapter 5. First the background in the image is studied and reduced using the software package *CIAO*. For this the energy range is limited to part where the synchrotron emission is higher than the background emission, potential particle events are excluded and an image of a background observation is prepared for being fitted in a later chapter to model the background. To exposure correct the image, a spectrum is extracted from the image and studied. With the spectral parameters, a weighted exposure map is produced and the observation image divided by it. To study the size and influence of the PSF, images are simulated at the positions of the studied X-ray structures in the observation image. These are then fitted with the fitting software *Sherpa* included in *CIAO*.
In chapter 6 the shock filaments in the image are studied using the obtained data. The filaments are fitted two dimensional to determine the morphology of the structures. A fit function consisting of the convolution of a gaussian PSF with an exponential fit function is used to fit the X-ray emission profiles, including the influence of the PSF. Using the fit results for the morphology, the filaments are fitted one dimensional as a projection along the filament. Also, the background observation is fitted here in the same way to get a model for the background. After this, a different model, which assumes that the observed profile is a projection of the intrinsic 3-dimensional emission profile on the image plane, is used. With this model the emission profile is fitted and compared to simulated projection profiles.

In chapter 7 the fitted width of the X-ray synchrotron emission profile is used to calculate a lower limit on the magnetic field at the shock front of HESS J1731-347. This is done by using the length scale of the cosmic ray distribution at the shock front in a model which considers that the electrons move away from the shock front by diffusion and by convection. Two special cases are treated where the electrons mainly suffer synchrotron losses while moving only either with diffusion or by convection. The results of these different models are calculated with different published shock velocities and compared.
At the end, a conclusion and an outlook is given based on the results of this work.

Chapter 2

The studied Source: HESS J1731-347

In this work, the supernova remnant HESS J1731-347 is studied. It was first discovered in TeV in observations with the *HESS* telescope (Aharonian et al. 2008), a Cherenkov telescope array located in Namibia. At the time of discovery, it was still an unidentified source, since no counterpart in other wavelengths was known and the observation time of 14h was not enough for a good resolution of the structure (see figure 2.1(a)). However, in 2008 a counterpart in radio was discovered as the supernova remnant G353.6-0.7 (Tian et al. 2008) which is shown in figure 2.2 (left). The TeV source overlaps the whole radio source, confirming it as a counterpart (Tian et al. 2008). Furthermore, the all-sky survey of the *ROSAT* X-ray Observatory of 1993 shows a diffuse X-ray emission (see figure 2.1(b)) with the same morphology as the lower half of the radio SNR (Tian et al. 2008). Only the lower half being visible could be due to the fact that the absorption increases towards the upper half of the image (Tian et al. 2008; Abramowski et al. 2011). Later observations in X-ray with *XMM-Newton* and a new observation with *HESS* with four times the initial exposure time, both shown in figure 2.2, showed a similar morphology as the radio observation in the overlapping regions, confirming their association (Abramowski et al. 2011).

The TeV γ-ray morphology of HESS J1731-347 was identified as being of a shell-type (Abramowski

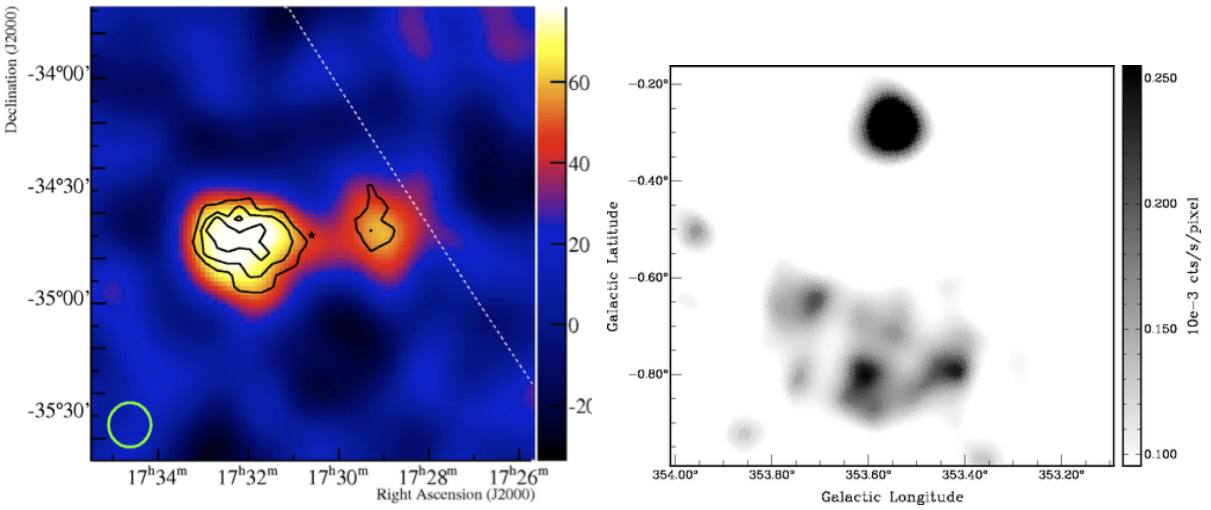

Figure 2.1: The first two images made of HESS J1731-347. Left: *HESS* TeV image smoothed with a gaussian. (Aharonian et al., 2008) Right: X-ray *ROSAT* image, exposure-corrected in the 0.1-2.4 keV band and smoothed with a Gaussian. (Tian et al., 2008) Only lower part of the remnant visible due to absorption.

et al. 2011). The angular radius of the remnant in radio is given in Tian et al. (2008) as ≈0.25°. In Abramowski et al. (2011) a fit of the radial γ-ray profile was done and the best fit angular radius is given by 0.27°, in agreement with the radio result. At the center a central compact object (CCO) can be seen (Klochkov et al. 2013).

The emission observed from HESS J1731-347 includes radio, X-ray and γ-rays. The X-ray emission was identified as synchrotron emission, but also in the radio and γ-ray emission clearly identified non-thermal emission was found (Abramowski et al. 2011). The extended X-ray emission is concentrated in arc-like structures like it is often seen in shell-type SNR (Abramowski et al. 2011), with parts of them also visible in radio and γ-ray.

Concerning the distance of HESS J1731-347 from the earth, in Abramowski et al. (2011) a lower limit of 3.2 kpc was estimated. This was done by comparing the absorption in the observation with that of the foreground and using galactic rotation curve models. In Abramowski et al. (2011) also an estimate on the position in the Galaxy and on the upper limit of the distance is done: Assuming that, because of the density of massive stars, supernovae are more likely to happen in the spiral arms of the galaxy, HESS J1731-347 could either be in the Scutum-Crux arm at a distance of ≈3 kpc or in the Norma arm, located at a distance of ≈4.5 kpc. There is also the Sagittarius arm at 12 kpc, but this distance would lead to a much higher luminosity and size than that of other TeV shell-type SNR, so it is more likely that HESS J1731-347 is near the first two arms. Another estimate on the distance was recently calculated in Fukuda et al. (2014) as 5.2 kpc.

In Abramowski et al. (2011) an upper limit for the density of the medium surrounding HESS J1732-347 was derived. Because of the lack of thermal X-ray emission in the observation, a thermal component was added to the X-ray spectrum assuming a non equilibrium ionization state with an ionization timescale and electron plasma temperature typical for young SNR. Depending on the temperature, they get either a density of 1 cm^{-3} or 10^{-2} cm^{-3} as a result. However the value of 1 cm^{-3} is unlikely because the shock speed would be one order of magnitude lower than in other SNR with measured synchrotron radiation. Using a density of 10^{-2} cm^{-3} they give a rough estimate of 3000 km s^{-2} for the shock speed and ≈2500 y for the age of HESS J1731-347.

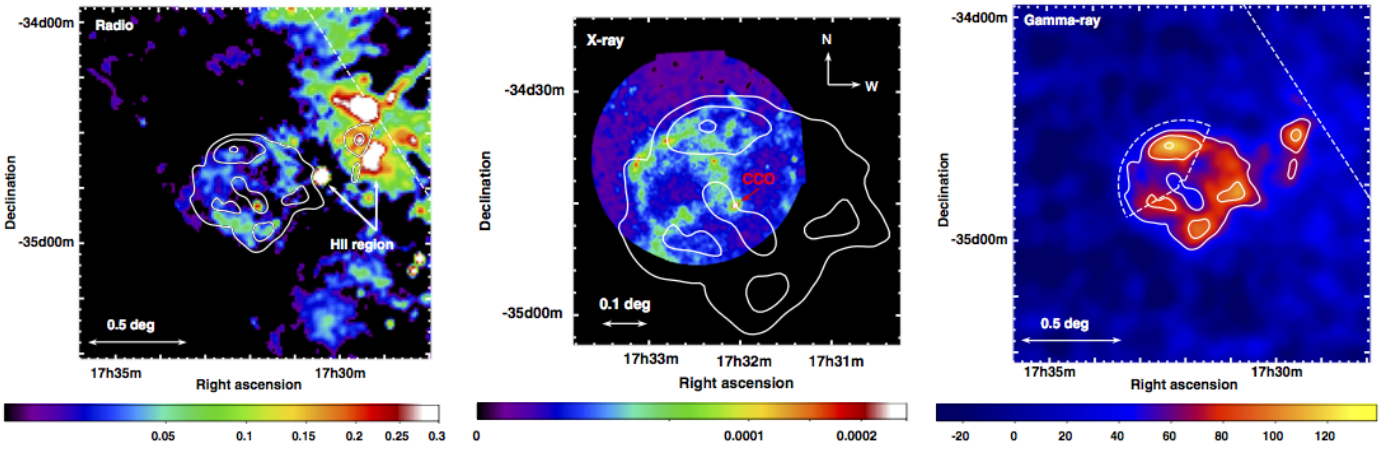

Figure 2.2: Three images of HESS J1731-347 in radio, X-ray and γ-ray.The radio (left) and γ-ray (right) image show the whole remnant, while the X-ray image is zoomed in and shows details of the shell. Left: *ATCA* radio image at 1.4 GHz. Middle: *XMM-Newton* image showing the energy band of 0.5-4.5 keV. The CCO inside the SNR is marked with a red arrow. Right: *HESS* TeV γ-ray image, smoothed with a Gaussian. (Abramowski et al., 2011)

Chapter 3

The Chandra X-ray telescope

The observation used in the analysis of this work was done with *Chandra*, an X-ray telescope. Since it is important to understand the telescope and its properties for the data analysis, the *Chandra* telescope will be discussed in this chapter based on the *Chandra Proposers' Observatory Guide* (Chandra X-ray Center 2013) and Arnaud et al. (2011). The *Chandra* detector is a X-ray detector, therefore in the beginning these detectors and especially CCD detectors will be discussed.

3.1 CCD X-ray detectors

In X-ray astronomy, as the name implies, observations are done by observing X-rays. This is done with X-ray detectors. A detector needs to have different important properties to give the best observational results. The incoming X-rays have to be converted into an electronic signal and then into data for analysis. This data should include information like the X-ray photon energy, the time when the X-ray was detected, the position on the detector and the detector should also be able to count the number of arrived X-rays as well as be able to distinguish between single events. Concerning the distinguishing of single events, the detector also needs to be able to distinguish the different kinds of events, since not only X-rays but also other particles can be detected. Apart from detecting events, another important property of a detector is to be able to survive the conditions in space. In space, it needs to operate in a very cold environment and vacuum and can also be hit by particle showers and single high energetic particles. However, the detecting material fulfilling these conditions also needs to have a broad energy range.
While there are other possible detectors, the in astronomy most popular detector design for the energy range of 0.5 keV to 10 keV, meeting these conditions, is the CCD detector. It is usually made out of silicon as detecting material, giving the detector a broad energy range. In the case of *Chandra*, the energy range is from less than 0.1 keV up to 10.0 keV in X-rays, however, also optical photons can be detected. CCDs (Charge-coupled-devices) were invented in 1969 at Bell Laboratories in New Jersey. CCDs consist of coupled capacitors. When a X-ray photon interacts through photoelectric absorption with the semiconducting silicon layer, electron-hole pairs are created. The electrons then, with the help of an electric field, are collected in pixels. In silicon each creation of an electron-hole pair requires an energy of about 3.7 eV. Therefore by counting the number of electrons produced in the event, the energy of the incident photon can be measured. Since the pixels are coupled in an array, each pixel row is read out by transferring the charge of one pixel to the next until the charge reaches a readout amplifier which measures and digitizes the charge. Here the number of electrons is stored as the pulse height amplitude (PHA) which linearly depends on the number of electrons and therefore also on the incident photon energy.

As the absorption probability of the photon in the semiconductor layer is constant per unit length, the probability of absorption is sensitive to the thickness of the layer. The inverse of the absorption probability is the mean absorption depth, which gives the mean depth of absorption of a photon in the layer. It is a function of the photon energy and therefore, the energy range of the detector is very sensitive to the thickness of the semiconductor layer. Photons with an energy too low interact at the surface and are not correctly detected and photons with a too high energy go through the layer without being detected.
However, before a photon can even reach the photo-sensitive semiconductor layer, it has to go through several dead layers of gates and insulators. Therefore the probability of a photon to be detected as an event with the detector is given by the Quantum efficiency QE, which depends on the photon energy.
As explained above, the lower the photon energy, the lower the probability of detection with the CCD design explained above. To improve the low energy performance of a CCD, instead of the above discussed so called front-illuminated (FI) CCD, a back-illuminated (BI) CCD can be used. It works like a flipped front-illuminated CCD and begins with the photo-sensitive region after just a very thin dead layer. By making the photo-sensitive region even thinner, the low energy performance is further improved. However, this design leads to less QE in the high energy range. By exposing the detecting layer to the radiation instead of the dead layers containing the electronics first, the danger of the CCD getting damaged is minimized. The *Chandra* ACIS detector consists of several front- and back-illuminated CCDs.
The time resolution of a X-ray CCD is limited by its readout time. While in other areas of use, CCDs are used to collect many photons in one pixel before the readout, astronomical X-ray CCDs are used in photon-counting mode. This way each individual photon event can be detected. In case of *Chandra*, the whole CCD consisting of 1024x1024 pixels is read out by four readout nodes with each having a readout frequency of 100 kHz (10^5 pixels per second), which means that reading out the whole image takes about 3 seconds. This has to be considered when observing a source with a known flux, since this can lead to the later discussed pileup problem if more than one photon per pixel is collected during the readout time. To improve the time resolution, only a fraction of the pixels in the image can be read out, but at the cost of image size.
When the pixels are read out as explained above, each PHA is compared to a predefined threshold to determine wether the event is a real source event or not. Additionally the PHAs of the surrounding pixels are recorded. In *Chandra* this is either a 3x3 pixel island in the *FAINT* mode or a 5x5 island in the *VFAINT* mode. Like shown in figure 3.1 this information is used to calculate a grade value, classifying the event. When analyzing the observational data, this is used to reject events which have a too high grade. While X-ray photons are expected to mainly have a PHA higher than the threshold in the center pixel, cosmic rays and other charged particles will also have high enough PHAs in the outer pixels because of producing additional electron-hole pairs.
Although CCDs are widely used in astronomy, they can have some problems which have to be considered when analyzing the data. The already mentioned pile-up due to high source flux per pixel is one of the problems. When two or more photons are detected in one pixel at the same readout time, these N photons are considered as one event. This makes the energy higher and since events at lower energies are lost while one high energy event is detected, pile-up effects harden the spectrum. In the HESS J1731-347 observation used in this work, this should not be a problem, since the source flux per pixel is low in this diffuse source.
Another problem is Charged transfer inefficiency (CTI) which all space-used CCDs suffer. It describes the phenomenon of charge lost in charge traps during the transport to the readout amplifier which leads to loosing electrons and therefore the event is detected with less energy. These traps are caused either by the manufacturing process or by radiation damage, which is why CCDs normally have a shield that can be used for protection if dangerous radiation or particles are expected. The *Chandra* ACIS front-illuminated CCDs where damaged due to low energy protons and therefore significantly suffer of CTI. This can be

corrected when the data is prepared for analysis. Also it is possible to try to locate the source near to the readout amplifiers to reduce CTI. This however increases the PSF (see section 3.2.2).

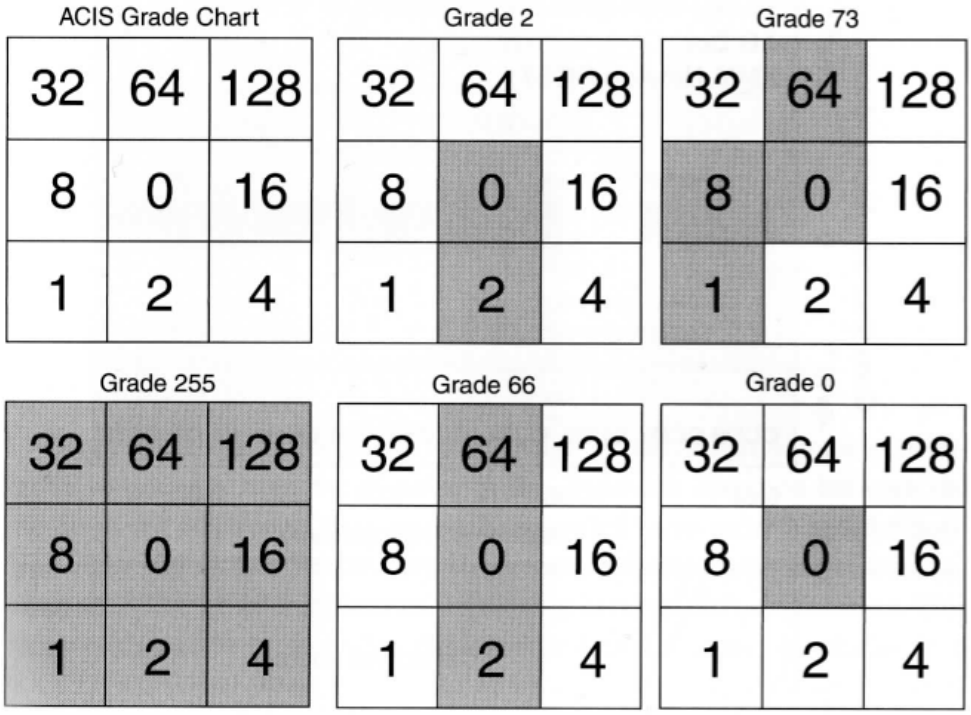

Figure 3.1: The grade system for a 3x3 pixel island. The pixel with the highest PHA compared to the threshold is defined as the middle pixel with a grade number of 0. The other grey pixels also have PHAs higher than the threshold. The full grade of an event is calculated as the sum of all grade numbers of pixels inside this 3x3 island with PHAs higher than the threshold. The calculated grade is a code that gives the positions of the activated pixels. (Arnaud et al. 2011)

3.2 Chandra

The *Chandra* X-ray space telescope (see figure 3.2) is one of *NASA*'s four great observatories, together with the *Hubble* Space Telescope (optical), the *Compton* Gamma-Ray Observatory and the *Spitzer* Space telescope (infrared). It was launched on July 23, 1999 from the Kennedy Space Center on board of the Space Shuttle Columbia. It is maintained and controlled from the ground by the *Chandra* X-ray Center (CXC), the Operations Control Center (OOC) and the Engineering Support Center (ESC). *Chandra* orbits the earth in a highly elliptical orbit with an apogee height of about 140000 km. With this it is outside of the radiation belts most of the time which grants an observation time of 63.5h per orbital period. To protect the detectors from radiation damage, a particle detector is mounted at the telescope, searching the environment of *Chandra* for charged particles. Furthermore, to hinder low energy electrons up to 100 keV from hitting the focal plane, a magnetic baffle is installed inside the telescope.
Chandra was built using the same optical principle of previous X-ray telescopes like the *Einstein* and *ROSAT* telescopes, but provides an angular resolution one order of magnitude higher. The *High Resolution Mirror Array* (*HRMA*), *Chandra*'s optical system, is built in a Wolter type I configuration, focusing the incoming X-rays into one focal point on the detector.
Chandra has two different detectors: The *Advanced CCD Imaging Spectrometer* (*ACIS*) and the *High Resolution Camera* (*HRC*). The *ACIS* consists of a 4 CCD array for imaging (*ACIS-I*) with 4 FI CCDs and a 6 CCD array with 2 BI and 4 FI CCDs for imaging and spectroscopy (*ACIS-S*). For improved

spectroscopy resolution, the *ACIS-S* can be used with the *High-Energy Transmission Grating Spectrometer* (*HETG*) which has a resolution of $E/\Delta E$ up to 1000 for energies within 0.4 keV and 10.0 keV. The *ACIS* is discussed in more detail below as it was used in the observation of HESS J1731-347.
The *HRC* consists of two micro channel plates. The *HRC-I* is used for wide-field imaging and has the largest field of view and highest image resolution on *Chandra*, but has a low spectral resolution. The other is the *HRC-S* which is used to read out the *Low Energy Transmission Grating Spectrometer* (*LETG*). Between low energies of 0.08 keV to 0.2 keV it provides the highest spectral revolution in *Chandra*.

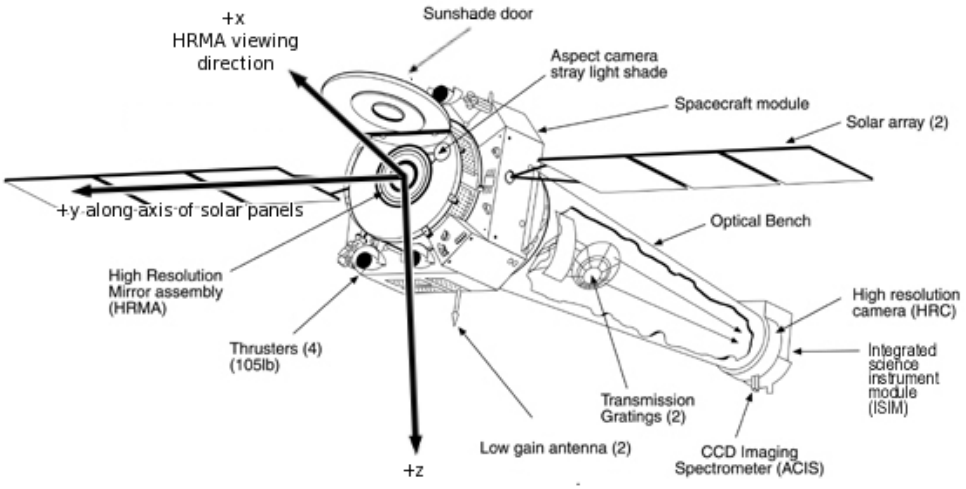

Figure 3.2: The *Chandra* space telescope. (Chandra X-ray Center 2013)

3.2.1 HRMA

The *HRMA* is based on the Wolter type I principle and consists of 4 pairs of concentric iridium coated mirrors (see figure 3.3) with the front pair mirror direction based on a paraboloid curve and the back mirror direction oriented on a hyperboloid curve. When an on-axis beam enters the telescope, it is reflected at both mirrors and focused in a point at a shorter focal length than with just a paraboloid oriented mirror. This means that the telescope can be built shorter and also the shorter focal length focuses the image on a smaller detector area, giving a better signal-to-noise-ratio. Normally, X-rays hitting a material either penetrate it or are absorbed within the material. However, for small grazing angles on metal surfaces, X-rays can be totally reflected, with the incident angle being the reflection angle.
The unobscured geometrical aperture of the *HRMA* of *Chandra* is 1145 cm^2. The obstruction of the mirror supporting structure is less than 10%. However, the effective area of the *HRMA* depends on the X-ray energy, since reflectivity, as well as the total reflection angle depend both on the photon energy.
The optical axis of the *HRMA* and therefore of *Chandra* is defined as the direction of the sharpest PSF. As explained in section 4.8, theoretically the on-axis PSF can be described as the diffraction image of a source and gives the smallest possible image in case of a point source. For off-axis sources, the size of the PSF is not only a consequence of diffraction. For off-axis angles the PSF is much larger than on-axis and a function of both the X-ray energy and the off-axis angle (see figure 3.4). The increase in PSF size is because of two reasons: Mirror aberrations lead to a broadening of the PSF, strongly dependent on the off-axis angle and the energy, and additionally the X-ray scattering $\propto E^2$ is increased for the higher X-ray energies.

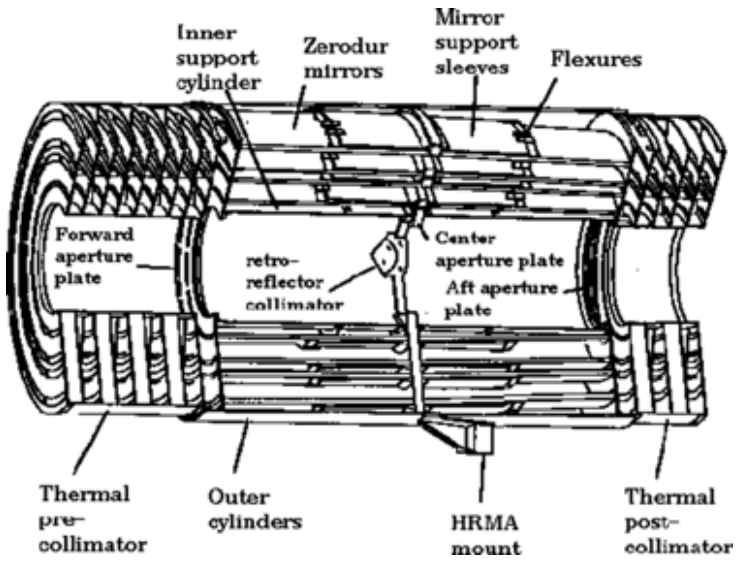

Figure 3.3: The *Chandra HRMA* with two pairs of concentric mirrors. (Chandra X-ray Center 2013)

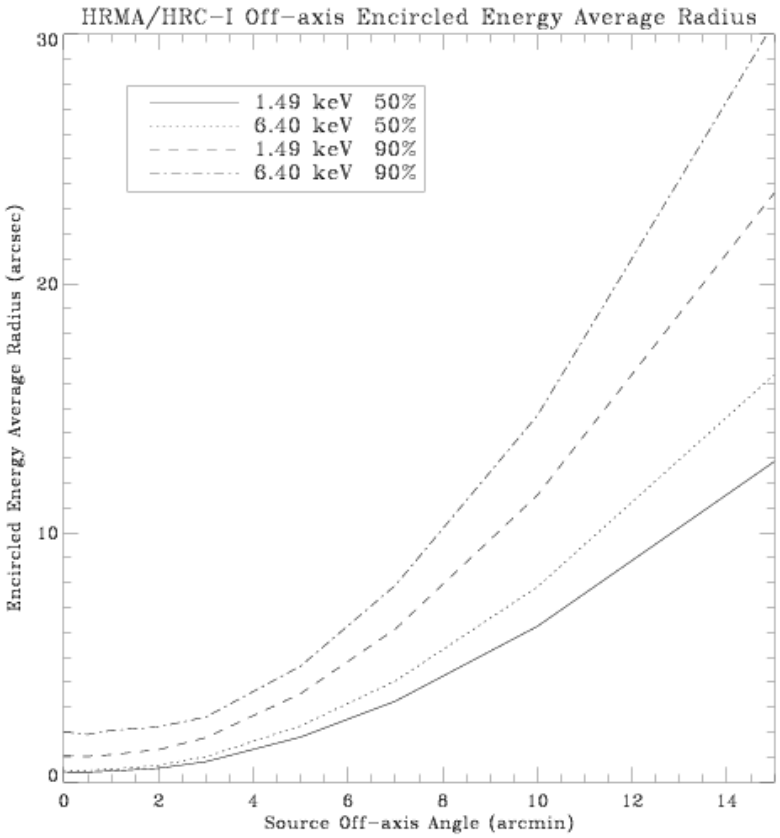

Figure 3.4: The size of the *HRMA* off-axis PSF shown for different energies and off-axis angles. The encircled energy radius gives the radius for 50% and 90% of the X-ray beam's energy to be included in the PSF. (Chandra X-ray Center 2013)

3.2.2 ACIS

The *ACIS* is one of the *Chandra* detectors. It is schematically shown in the focal plane in figure 3.5, which shows the 4 *ACIS-I* and 6 *ACIS-S* CCDs with the S1 and S3 CCDs being back-illuminated. The aimpoints for both, defined as the position of the source flux of a point source on the optical axis of the

HRMA with no offset, are also shown in figure 3.5. Of these 10 CCDs, 6 can be used at the same time, and it is recommended by the *Chandra X-ray Center* to specify 5 optional CCDs, even if only one is needed for the observation.
Each CCD contains 1024x1024 pixels with a pixel size of 23.985 microns, which corresponds to 0.492 arc seconds in the image. The on-axis optical resolution of the *ACIS* is limited by this pixel size and not by the optical capabilities of the *HRMA*. Considering the gaps between the CCDs, the size of the *ACIS-I* array is given by 16.9x16.9 arc minutes and the size of the *ACIS-S* by 8.3x50.6 arc minutes.
The effective area of the *ACIS* (see figure 3.6) is a function of the energy and the off-axis angle. It is a combination of the effective area of the *HRMA* and the QE of the detector, degrading off-axis due to vignetting. Vignetting is an optical effect which depends also on the X-ray energy and describes the ratio of the on-axis effective area compared to off-axis area. The QE of the *ACIS*, describing the probability of a photon to be detected as an event, is different for the FI and BI CCDs, but in both cases it strongly depends on the photon energy. For the FI CCDs it is higher than 30% for energies between 0.7 keV and 11.0 keV, with a maximum of about 90% near 5 keV.
The *ACIS* is mounted on the *Science Instrument Module* (*SIM*) (see figure 3.7). It is a movable bench which connects the detector with the telescope and provides the possibility to move the detector as well as thermal isolation. The detector can be moved by up to 0.8 inches along the X-axis to adjust the focal length and up to 20 inches along the Z-axis in the detector plane (see figure 3.5).
The *ACIS* can be used in two different operation modes, the Continuous Clocking (CC) Mode and the Timed Exposure (TE) Mode. In the CC mode, the spatial size of the image is reduced by one dimension and images of 1x1024 pixels are produced, which can be read out much faster than a full image of 1024x1024 pixels. The TE mode, used in the observation of HESS J1731-347, uses all 1024x1024 pixels for an image and has variable exposure times for accumulating events. These exposure times are called frame times and can be selected from 0.2 seconds up to 10.0 seconds. To read out the complete CCD still takes about 3.2 seconds, independent of the exposure time. To reduce the readout time, it is possible to select subarrays of the CCD and use less than 1024x1024 pixels for the observation. The good time intervals (GTI) are the time intervals during which detector events are accumulated.

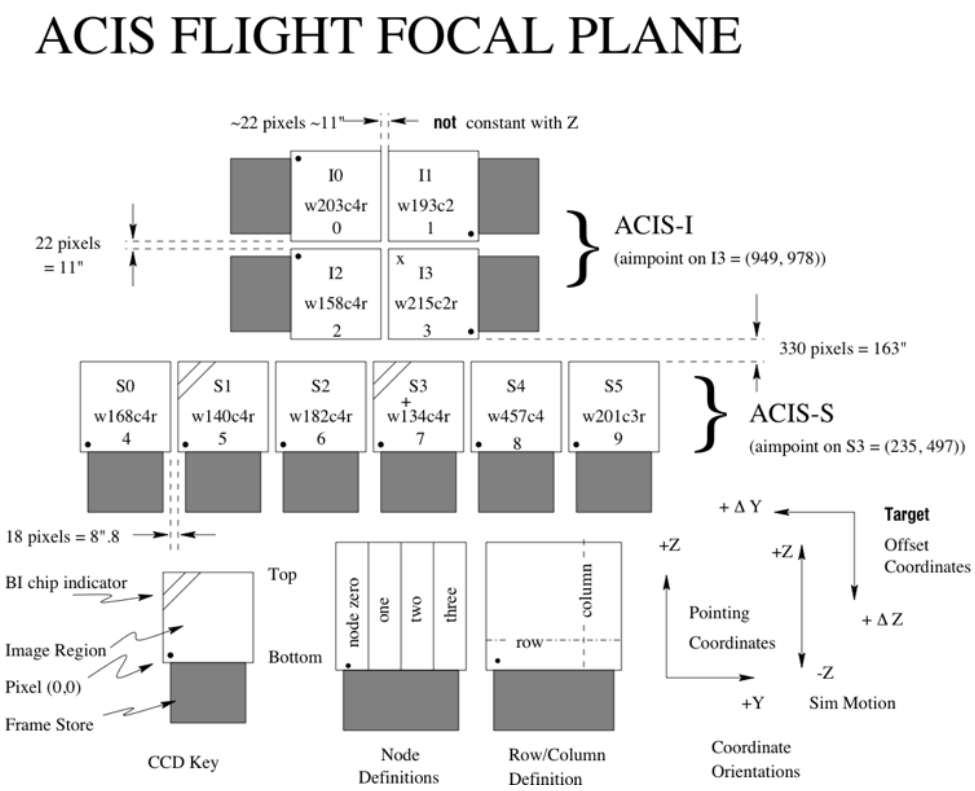

Figure 3.5: The *ACIS* detector shown schematically in the focal plane. On the lower right the coordinate system and the possible detector movement direction with the *SIM* module is shown. The not shown X direction is along the focal axis. The x and + give aim points for the *ACIS-I* and *ACIS-S*. (Chandra X-ray Center 2013)

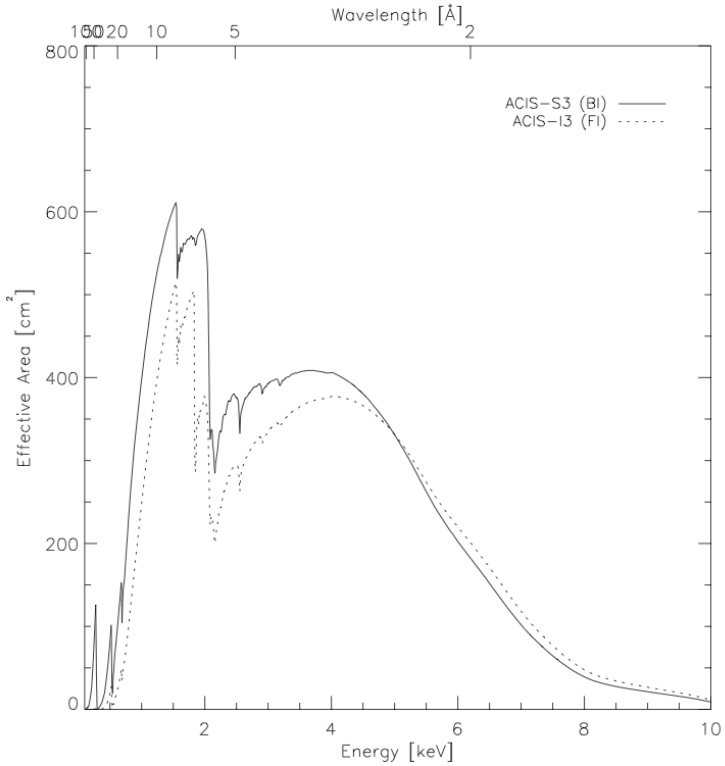

Figure 3.6: The *ACIS* effective area calculated for the *ACIS-I3* and *ACIS-S3* CCDs in dependance of the X-ray energy. The effect of the molecular containment is already included. (Chandra X-ray Center 2013)

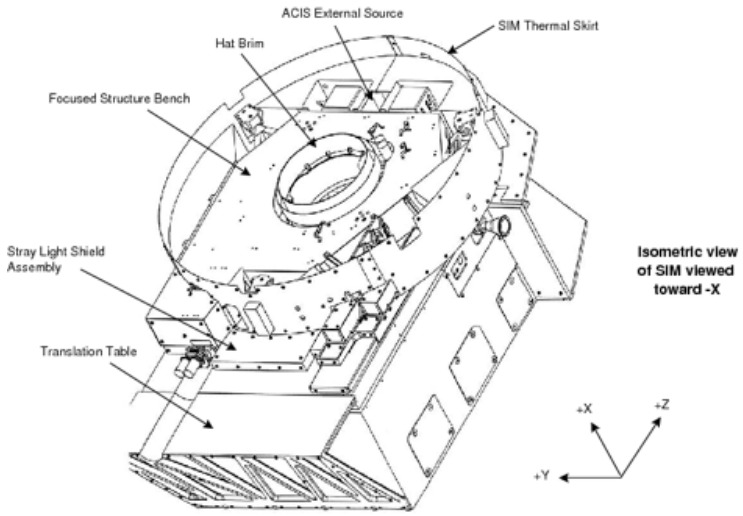

Figure 3.7: The *SIM* module which provides thermal isolation and movement to the *Chandra* detectors. (Chandra X-ray Center 2013)

Chapter 4

Theoretical Aspects

In this chapter we summarize some of the concepts that will be extensively used in the context of this work.

4.1 Supernovae

At the end of its life, a star with a mass high enough becomes a supernova, a luminous explosion which can be brighter, for a few weeks, in the optical than a whole galaxy. There are different types of supernovae, with some of them leaving a neutron star or black hole behind and some of them disrupting the star completely. In this section, following the explanations in Longair (2011), these different types of supernovae are discussed and also the evolution of stars with masses high enough to trigger supernovae.

Evolution of a Star

At the beginning a star consists mainly of Hydrogen H but also Helium He and heavier elements. Due to its high mass and therefore high pressure and temperature inside the core, burning hydrogen to helium He can take place. This core where the burning takes place consists of 7% of the star's mass. When the hydrogen in the core is exhausted, not longer providing energy to the burning process stabilizing the core, the core collapses while at the same time, the outer shell expands. The helium burning continues in the inner part of the outer shell. With the collapse of the core, the temperature inside rises. If the mass of the star is sufficiently high, this leads to helium burning as $3\ ^4\text{He} \rightarrow ^{12}\text{C}$ using the triple-α process and also burning to oxygen. Again, when the fuel in the core is exhausted, the core consisting of C and O collapses but the He burning continues in a shell outside the core until it reaches the shell of the H burning and the temperature is not sufficient for He burning anymore. If the star has not enough mass, the burning chain ends here, and the collapsed C-O core can become a white dwarf and a planetary nebula is formed when the shell around it is blown away. For lower mass stars the same can happen after the H burning phase and a He white dwarf is formed.
For higher mass stars however, the burning in the collapsed core and outside continues in the same way as described above. Each time the core collapses a new layer of a burning element is left outside the core with the star eventually getting an "onion"-like structure as shown in figure 4.1. The order of the burning to heavier elements can also be seen in figure 4.1 and it ends with Silicon Si burning to Iron Fe and Nickel Ni. With iron the fusion to heavier elements cannot continue since it has the highest binding energy of all elements, meaning that fusion to heavier elements is not energetically favorable. Therefore the core collapses but is not stabilized this time and a supernova of type II occurs.

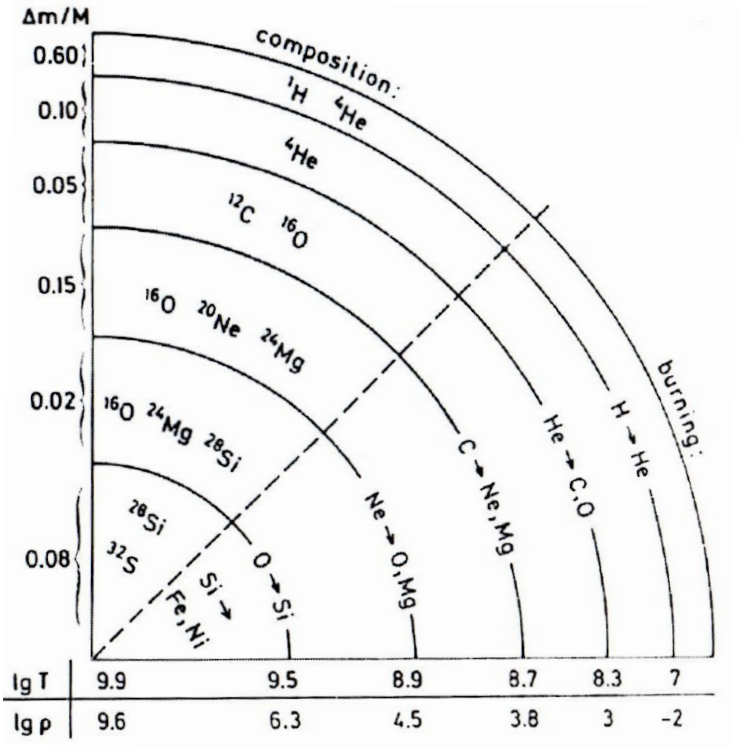

Figure 4.1: Onion structure of a 25 solar mass star. The typical values for mass fraction per shell, density in g cm^{-3} and temperature in K are shown. (Longair 2011)

.

4.1.1 Supernova Type II

Type II supernovae are core collapse supernova, where the collapse of the iron core leads to the explosion. There are different types of supernovae type II, which can be identified by different light curves. All of them have in common that Hydrogen lines are present.

In the fusion processes explained above, a lot of neutrinos are produced, which can, because of their small cross section leave the star and take energy with them. From each fusion phase to the next, the neutrino production increases greatly, leading to a much faster energy loss of the core and to an earlier collapse. For example in case of a star with 15 solar masses, the Hydrogen burning takes 11 My, the carbon burning only 2000 y and the Silicon burning only 18 d. After this a core made of Iron of about 1.5 solar masses is formed. The temperature inside the core reaches temperatures in the range of 10^9 K leading to additional energy draining reactions. The inverse β-decay in the form of

$$p + e^- \rightarrow n + \nu_e$$

leads to even more energy loss through neutrinos and also high energetic γ-rays lead to the photodisintegration of Iron into Helium

$$^{56}Fe + \gamma \rightarrow 14\,^{4}He$$

also draining energy of the core. An energy of more than 10^{46} J is released, which is about 10 percent of the core's rest mass. With this much energy loss, the core cannot maintain the pressure for stabilizing and collapses within about 1 second into a proto-neutron star. Its density is high enough to trap even the neutrinos inside. When the density of the collapsed core is high enough to reach nuclear densities it cannot be further compressed, which causes a shock wave, traveling back outside through the still infalling material. The shock wave looses energy through dissociation of nuclei, ram pressure of the

infalling material and neutrino emission, when the shock reaches regions where the density is low enough that neutrinos can escape (Pejcha & Thompson 2012). This leads to a quasi-static accretion phase with an accreting proto-neutron star surrounded by a quasi-static shock (Pejcha & Thompson 2012). The supernova is then continued by the *delayed neutrino mechanism* which describes the process of neutrinos diffusing out of the proto-neutron-star and reheating the shock which causes then the explosion (Pejcha & Thompson 2012).

4.1.2 Supernova Type I

Type I supernova are not caused by core collapse. They are believed to be caused by a white dwarf exploding in thermonuclear reactions. There are also different type I supernova, which are distinguished by different emission lines visible in their light curves. In opposite to type II, there are no Hydrogen lines visible, which is due to the fact that the type I supernova's origin is a white dwarf which has no Hydrogen shell left. A white dwarf cannot have more than about 1.4 solar masses, which is called the Chandrasekhar mass. With more mass, the electron degeneracy pressure is not enough to stabilize it and it collapses into a neutron star and is stabilized due to the neutron degeneracy pressure. A white dwarf can for example gain mass by accreting matter from a companion star. However, it is believed to be possible that due to the energy released with the fusion of Carbon and Oxygen, the star explodes in a supernova type I, before it can collapse.
Apart from being interesting objects, type I supernovae are very useful in astronomy as so called standard candles. Since the typical absolute magnitude of type I is known as -19.5 $\pm$ 0.1, it can be used to compare it to the observed magnitude, helping to determine the distance of the observed supernova.

4.2 Supernova Remnants

In this section an explanation on supernova remnants (SNR) and their evolution is given, based on Longair (2011). Supernova remnants are, as the name implies, what remains of a star after it exploded in a supernova. They are considered as sources for high energy particles with radio, γ-ray and X-ray observations as evidence. There are two different types of remnants: The *shell-like* remnant with the emission maximum at the shell region and the *crab-like* remnant with the emission maximum at the center from an emitting neutron star, also called pulsar wind nebulae (PWN). Supernova remnants are emitting in different parts of the electromagnetic spectrum. Hot gas emits in optical and infrared and very hot gas, heated by the supernova shock wave emits in X-ray via bremsstrahlung and emission from atomic transitions. A remnant also emits in radio and X-ray via synchrotron radiation, caused by high energetic electrons accelerated at the shock front. This X-ray synchrotron radiation is studied in this work. Some SNR like HESS J1731-347 are also bright in the TeV range, emitting γ-rays.
The evolution of a supernova remnant, from its formation until its end, can be described with four stages. The first stage begins right after the explosion with the star's shell being heated up by the explosion and ejected with a velocity in the range of 10^4 km/s. Since the ejected material at the beginning has much more mass than the swept up interstellar gas, the momentum of the shock is assumed to be constant and the remnant's radius is proportional to the speed of the ejected material in phase 1. With the speed being supersonic, a shock front is formed ahead of the ejected material. Between the swept up and shocked gas and the ejected material is a so called *contact discontinuity*. It describes a transition layer between plasma with different properties on both sides. The mass density in the region behind the shock is several times higher than in the region ahead of the shock. This is very important for the diffuse shock acceleration explained later.
The second stage starts when the swept up material's mass is of similar order as that of the ejected

material. Due to conservation of momentum the expansion is decelerated and according to a calculation done by Taylor end Sedov (Taylor 1950) the radius of the remnant is now given by the proportionality relation $r \propto t^{5/2}$. With the most outer parts of the ejected material first decelerated, now also material from inside the remnant is swept up here, increasing the mass density. With increasing density, the speed of sound decreases and the swept up material from outside begins to enter the remnant with supersonic speed, leading to a reverse shock. This reverse shock travels back trough the remnant to its origin, heating up material on the way, leading to thermal X-ray emission.
In the third stage, seen in remnants with an age in the range of 10^4 years, the until now not important cooling due to radiation becomes important. The dense outer shell of the expanding remnant cools down below 10^6 K and X-ray line emission of heavy ions and mainly optical emission gets important which lets the remnant further loose energy. The still hot material from further inside pushes against the cool outer shell, which is why this stage is called the *snow-plow* phase.
In the last stage, the expansion has lost nearly all of its momentum and becomes subsonic. The cooled material of the remnant is mixed with the interstellar medium and the remnant vanishes. The evolution and stages of a *shell-like* supernova remnant can be seen in figure 4.2, showing the remnant's radius versus its age.

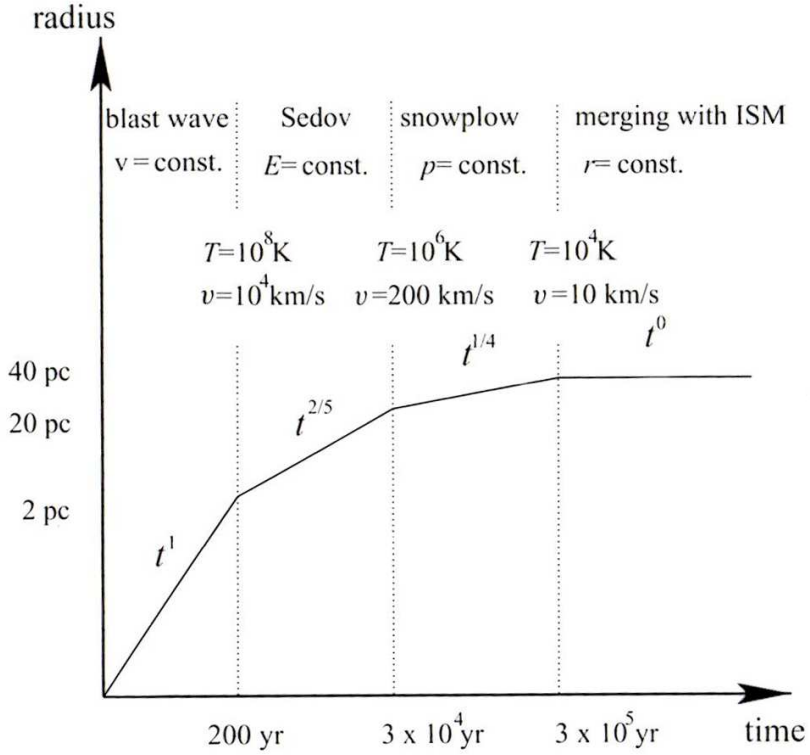

Figure 4.2: The evolution stages for a typical shell-like SNR showing the radius of the remnant vs. its age. (Rosswog & Brüggen 2007)

4.3 Diffusive Shock Acceleration

Supernova remnants are considered as one of the sources for cosmic high energy particles. The acceleration of these particles is expected to take place at the shock front. This process is called diffusive shock acceleration or first order Fermi acceleration since this kind of acceleration was first introduced by Fermi (Fermi 1949).

For the acceleration to take place, a strong shock like in a supernova remnant is needed which propagates through the medium. Behind the shock on the so called *downstream* side is the compressed interstellar medium and before the shock is the uncompressed interstellar medium on the so called *upstream* side. On both sides of the shock, relativistically high energy particles are expected, moving much faster than the shock speed. The conditions at the shock front can be seen in figure 4.3. In figure 4.3(a) the shock

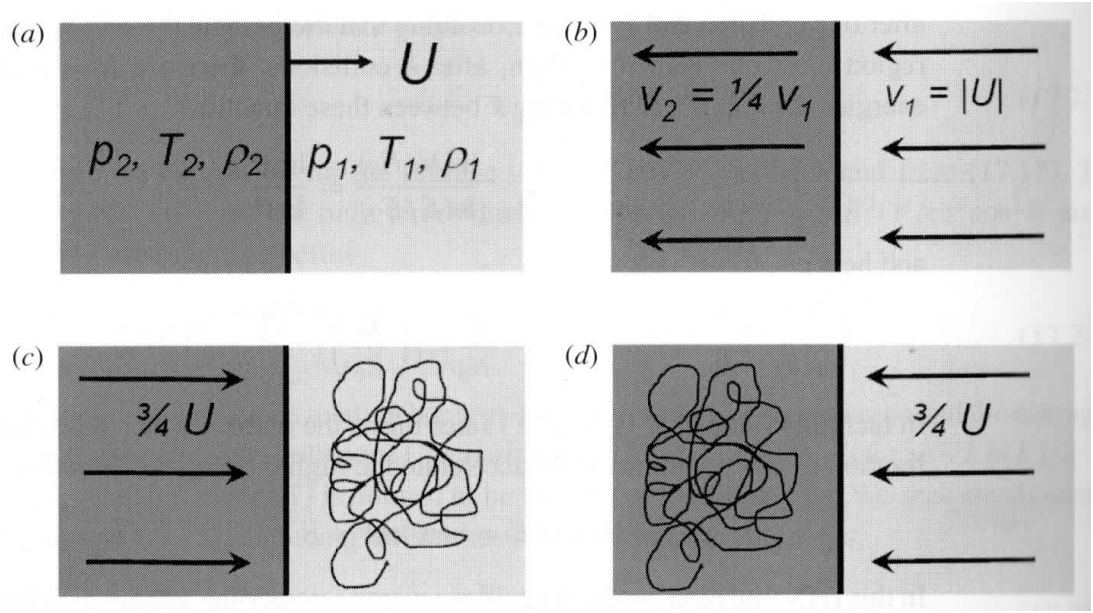

Figure 4.3: The conditions at the shock front with the dark grey area as the *downstream* side and the light grey area as the *upstream* side. (a) shows the shock front moving with velocity U through matter. The pressure, temperature and mass density are different on both sides of the shock front. In (b) the velocity of the matter on the *upstream* and *downstream* side is shown in the shock frame with the shock at rest. (c) shows the velocity of the *downstream* matter when the *upstream* side is at rest with the velocity of the *upstream* particles isotropic. In (d) the same is shown when the *downstream* side is at rest. (Longair 2011)

moves with velocity U through the medium. Like shown for example in Longair (2011), with a specific heat capacity of $\gamma = 5/3$ the ratio between the densities is $\rho_2/\rho_1 = 4$ in case of a strong shock. With the conservation of mass

$$\rho_1 v_1 = \rho_1 U = \rho_2 v_2 \tag{4.1}$$

this means that in the rest frame of the shock like shown in figure 4.3(b) the matter on the *upstream* side flows with a velocity of $v_1 = U$ into the shock region and leaves with a velocity of $v_2 = \frac{1}{4}v_1$. Looking at the shock front from either the *downstream* rest frame or the *upstream* rest frame like shown in figure 4.3(c) and (d) this means that in both cases the region of one side approaches the region of the other side with a relative velocity of $v = 3/4U$. Another important point is that on both sides, turbulences in the magnetic field are present and scattering of the particles with the magnetic field takes place. Considering now a particle from ahead of the shock in the *upstream* region diffusing through the shock, its velocity vector gets randomized and gets isotropic with respect to the particles motions in the *downstream* region. With this the particle can again diffuse through the shock front and this can be repeated. With the two sides approaching each other, the particle gains energy every time it crosses the shock front and never loses energy. This can be shown by doing a Lorentz transformation. With the velocity of the approaching side of $v = 3/4U$ the energy E' of the particle with initial energy E after crossing the shock front is given by (Longair 2011)

$$E' = \gamma_v (E + p_x v) \tag{4.2}$$

with p_x being perpendicular to the shock front. Since $v \ll c$ and therefore the shock being non-relativistic, $\gamma_v = 1$. The crossing particle however is considered relativistic with $E = pc$ and with $p_x = p\cos\theta$, the energy change ΔE and the fractional energy change $\Delta E/E$ of the particle can be written as:

$$\Delta E = pv\cos\theta \qquad \frac{\Delta E}{E} = \frac{v}{c}\cos\theta \tag{4.3}$$

Averaging $\cos\theta$ over the range of 0 to $\pi/2$ which equals 2/3 (Longair 2011), leads to an average fractional energy increase for crossing the shock twice, to the other side and back, of

$$\left\langle \frac{\Delta E}{E} \right\rangle = \frac{4}{3}\frac{v}{c} = \frac{U}{c}. \tag{4.4}$$

This means that after k cycles the particle with initially an energy of E_0 has then an energy E_k of

$$E_k = \left(1 + \left\langle \frac{\Delta E}{E} \right\rangle\right)^k \cdot E_0 = \left(1 + \frac{U}{c}\right)^k \cdot E_0. \tag{4.5}$$

However, an accelerated particle cannot gain infinite energy this way. There is a probability given by the fraction of particles leaving the shock per unit time for the particle to get away from the shock front. This can be calculated by comparing the number of particles which cross the shock every time $\frac{1}{4}Nc$ (Longair 2011), with N as the number density of the particles, and the number of particles which are swept away from the shock every cycle $\frac{1}{4}NU$ (Longair 2011). By dividing them one gets the fraction of lost particles as U/c which is also the escape probability. Assuming a typical shock velocity of 3000 km/s would result in an escape probability of about 1%. As shown in equation 4.4 this is then also the amount of energy gained per cycle. Comparing these numbers at first look it seems as the acceleration does not give the particles much energy during the process. However, statistically there are a few particles which can stay much longer in the shock region and gain much more energy. This can also be seen in the differential energy spectrum of the particles which is given as (Longair 2011)

$$\frac{N(E)}{dE} \propto E^{-2}. \tag{4.6}$$

Once a particle is away from the shock front, the shock and the particle move away relatively from each other, so the particle cannot be accelerated again.
There are two reasons why the magnetic field at the shock front has to be high enough as condition for acceleration to happen. As explained above, the particles scatter with the magnetic field and are therefore directed back to the other side of the shock front. This change of sides is needed for the acceleration and therefore the magnetic field has to be high enough for the scattering process. The other reason is the gyroradius r_g of a charged particle with charge q in a magnetic field B given by $r_g = \frac{\gamma m_0 v_\perp}{|q|B}$. The gyroradius gives the radius of the circular motion of a moving charged particle in a magnetic field due to the Lorentz force. The lower the magnetic field, the bigger the radius, giving a particle with an energy high enough the possibility to escape from the shock region without being accelerated. This means that the magnetic field has to be high enough to confine the particles in the shock region while they cross the shock front and are accelerated.

4.4 Synchrotron Radiation

In this work the synchrotron emission of high energetic electrons in the magnetic field at the shock front of the supernova remnant HESS J1731-347 is studied. From classical electrodynamics it is known that this is due to the Lorentz force: Charged particles moving in a magnetic field with a velocity component

perpendicular to the magnetic field (see figure 4.4), are accelerated in a direction perpendicular to both the magnetic field and the initial velocity component. The particles do not gain energy in the process and the energy of the movement in the initial direction is radiated as synchrotron emission. Since the electrons have an energy in the TeV range this has to be treated relativistically and the equation of motion for an electron with mass m_e and charge e moving in an uniform and static magnetic field $\vec{B}$ with velocity $\vec{v}$ becomes:

$$\gamma m_e \frac{d\vec{v}}{dt} = e(\vec{v} \times \vec{B}) \tag{4.7}$$

with γ as the Lorentz factor. With $\vec{v} = \vec{v_\perp} + \vec{v_\parallel}$ like shown in figure 4.4 and $\vec{v_\parallel} \times \vec{B} = 0$ the acceleration

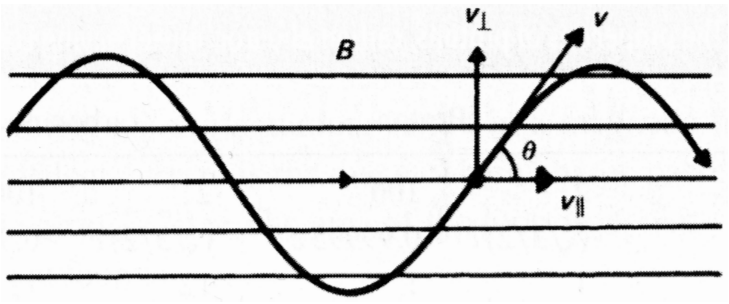

Figure 4.4: Motion of a charged particle with velocity v in a uniform and static magnetic field B. Adopted from (Longair 2011).

perpendicular to the electron's motion can be written with equation 4.7 as

$$\frac{dv_\perp}{dt} = a_\perp = \frac{e|v_\perp||B|}{\gamma m_e} = \frac{e|v||B|}{\gamma m_e}\sin\theta \tag{4.8}$$

with θ as the angle between $\vec{v}$ and $\vec{B}$ as shown in figure 4.4. Using the relativistic version of Larmor's formula, which describes the total energy loss rate of an accelerated charged particle, equation 4.8 can be inserted and in case of only perpendicular acceleration the total loss rate is given as (Longair 2011):

$$-\frac{dE}{dt} = \frac{\gamma^4 e^2}{6\pi\epsilon_0 c^3}|a_\perp|^2 = \frac{e^4 B^2}{6\pi\epsilon_0 c m_e^2}\frac{v^2}{c^2}\gamma^2\sin^2\theta \tag{4.9}$$

By using the relation $c^2 = (\mu_0\epsilon_0)^{-1}$, $U_{mag} = B^2/2\mu_0$ as the energy density of the magnetic field and $\frac{e^4}{6\pi\epsilon_0^2 c^4 m_e^2} = \sigma_T$ as the Thomson cross section, equation 4.9 can be written as:

$$-\frac{dE}{dt} = 2\sigma_T c U_{mag}\left(\frac{v}{c}\right)^2\gamma^2\sin^2\theta \tag{4.10}$$

Averaging over the pitch angle θ the average energy loss rate results in (Longair, 2011)

$$-\frac{dE}{dt} = \frac{4}{3}\sigma_T c U_{mag}\left(\frac{v}{c}\right)^2\gamma^2. \tag{4.11}$$

With $\left(\frac{v}{c}\right)^2 \approx 1$ for highly relativistic electrons and with $\gamma^2 = \frac{E^2}{m_e^2 c^4}$ equation 4.11 can be integrated by separation of variables which results in

$$E(t) = \frac{E_0}{1 + t/\tau} \approx \frac{E_0}{1 + E_0 B^2 t/635} \tag{4.12}$$

as a relation for the electron energy changing with time when radiating and having an initial energy E_0. $\tau = \frac{3m_e^2 c^3}{4\sigma_T U_{mag} E_0}$ is the synchrotron loss time after which the electron has lost half of its energy.

4.5 Diffusion of electrons in a fully ionized plasma

As described in section 4.3, the electrons move by diffusion from one side of the shock to the other during the acceleration process. Diffusion in plasma describes the motion of plasma due to unequally distributed numbers of particles in the plasma or an unequal temperature distribution in the plasma. Diffusion can be described by a random walk (Inan & Golkowski 2011). This means that all particles start at $x = 0$ and change their position by Δx each time step Δt. While the average position of the particles $\langle x \rangle$ stays constant with time, the variance of the particle position $\langle x^2 \rangle$ grows linearly with time (Inan & Golkowski 2011). The reason of diffusion is a force given by the pressure gradient (Inan & Golkowski 2011)

$$F = -\nabla p = -k_B T \nabla N \tag{4.13}$$

with the pressure p described by the perfect gas law with T as the temperature of the particles and N as the number density of the particles in the plasma. Assuming that the momentum equation, due to frictional drag force by particle collisions, is in a steady state, it can be written as (Inan & Golkowski 2011)

$$-\nabla p = -k_B T \nabla N = mvN\vec{u} \tag{4.14}$$

with $\vec{u}$ as the plasma fluid velocity and mv as the particle momentum. The flux Γ of particles from a region with higher particle density to a region with lower density can therefore be written as (Inan & Golkowski 2011)

$$\Gamma = N\vec{u} = -\frac{k_B T}{mv}\nabla N = -D\nabla N \tag{4.15}$$

with $\Gamma = -D\nabla N$ known as Fick's first law where ∇N describes the gradient of density and D is the diffusion coefficient which describes the amount or strength of the diffusion process.
In case of a fully ionized plasma in a magnetic field like the plasma at the shock front of a SNR, the diffusion of the plasma can be described as the diffusion of a single conducting fluid (Inan & Golkowski 2011). The steady state of the magnetic forces and the forces due to a pressure gradient can be written similar to equation 4.14 as (Inan & Golkowski 2011)

$$\nabla p = \vec{J} \times \vec{B} \tag{4.16}$$

with $\vec{J} = \sigma(\vec{E} + \vec{u} \times \vec{B})$ as the current density. Calculating the cross-product of the current density $\vec{J}$ with the magnetic field vector $\vec{B}$ and inserting the result in equation 4.16 gives

$$\vec{u}_\perp = \frac{\vec{E} \times \vec{B}}{B^2} - \frac{\nabla p}{\sigma B^2} \tag{4.17}$$

as the plasma fluid velocity perpendicular to the magnetic field lines. The first part on the right side of equation 4.17 is the velocity due to the electromagnetic forces while the second part describes the velocity due to diffusion. Using the diffusion part and calculating the flux by inserting the perfect gas equation, a comparison with Fick's first law

$$\Gamma = N\vec{u}_\perp = -\frac{N\nabla p}{\sigma B^2} = -\frac{Nk_B T}{\sigma B^2}\nabla N = -D_\perp \nabla N \tag{4.18}$$

shows that the diffusion coefficient for a fully ionized plasma in a magnetic field is given by

$$D_\perp = \frac{Nk_B T}{\sigma B^2}. \tag{4.19}$$

Normally however, not the $D_\perp \propto 1/B^2$ dependence is found in experiments, but a faster diffusion given by the Bohm diffusion coefficient (Inan & Golkowski 2011)

$$D_{\perp,\mathrm{Bohm}} = \frac{k_B T}{16 q B} \tag{4.20}$$

with q as the charge of the diffusing particles. It is an experimental result that was found by Bohm in 1949 (Bohm et al. 1949). It is believed that it is caused by plasma turbulences (Inan & Golkowski 2011) which is not considered in the classical theory above.

4.6 Cosmic Rays

HESS J1731-347 is considered as a source for cosmic rays. Therefore in this section we give a brief introduction on cosmic rays and their most relevant properties.
Cosmic rays are the only particles detected on the earth from sources outside the solar system. They consist 98% of protons and nuclei and 2% of electrons. These 98% are divided in 87% protons, 12% helium nuclei and 1% heavier nuclei (Longair 2011).
Cosmic rays were first discovered in 1912 and 1913 by Hess and Kolhörster who measured the atmosphere's ionization and discovered that the ionization increases higher up in the atmosphere, which means that the radiation has to come from above the atmosphere. After their discovery, cosmic rays were used for a long time to perform particle experiments, and while particle experiments are now performed with built accelerators, nature can still produce higher particle energies as shown in figure 4.5. It shows the power-law distribution of the cosmic rays measured by various experiments from 10^{12} eV up to 10^{21} eV. However, no cosmic ray has been detected until now with an energy of 10^{21} eV. The noticeable features in the spectrum are the *knee* at about 10^{15} eV and the *ankle* at about 10^{18} eV. The *knee* is considered as the limit for cosmic rays accelerated in supernova remnants. Cosmic rays with higher energies are expected to be accelerated in other ways inside the galaxy like large-scale galactic winds or to originate from sources outside the galaxy. However it is still not certain where they come from, especially the cosmic rays with energies beyond the *ankle*.
The abundance of elements in the cosmic rays is mostly similar to the elemental abundance in the solar system, however there are a few differences. The cosmic rays contain less hydrogen and helium relative to the heavier elements. Also the elements lithium, beryllium, boron and also a few elements with less protons next to iron are far more abundant in the cosmic rays compared to the solar system abundances. The reason for the overabundance of these elements is the spallation of heavier elements. This means that the heavier elements collide with cold interstellar matter on their way to earth, getting divided by this into less heavy elements and making their abundance higher.
To define a confinement volume as well as to try to explain the *knee* in the spectrum in figure 4.5, the, in section 4.3 introduced, gyroradius can be used:

$$r_g = \frac{\gamma m_0 v_\perp}{|q| B} \tag{4.21}$$

With this, the limit of about 10^{18} eV can be interpreted as the energy where cosmic rays can leave the galaxy because of their big enough gyroradius and therefore not longer being confined in the galaxy by the galactic magnetic field. For a galactic magnetic field strength of $3{\cdot}10^{-10}$ T, the gyroradius of a proton with an energy of 10^{18} eV is roughly as big as the thickness of the galaxy (Longair 2011). With an energy of 10^{20} eV the trajectory of a cosmic ray is barely influenced by the magnetic field (Longair 2011).
However, with cosmic rays at these high energies the distance of the origin of the observed ray is limited by the *GZK*-effect (Greisen-Kuzmin-Zatsepin). In the rest frame of high energy cosmic rays the photons

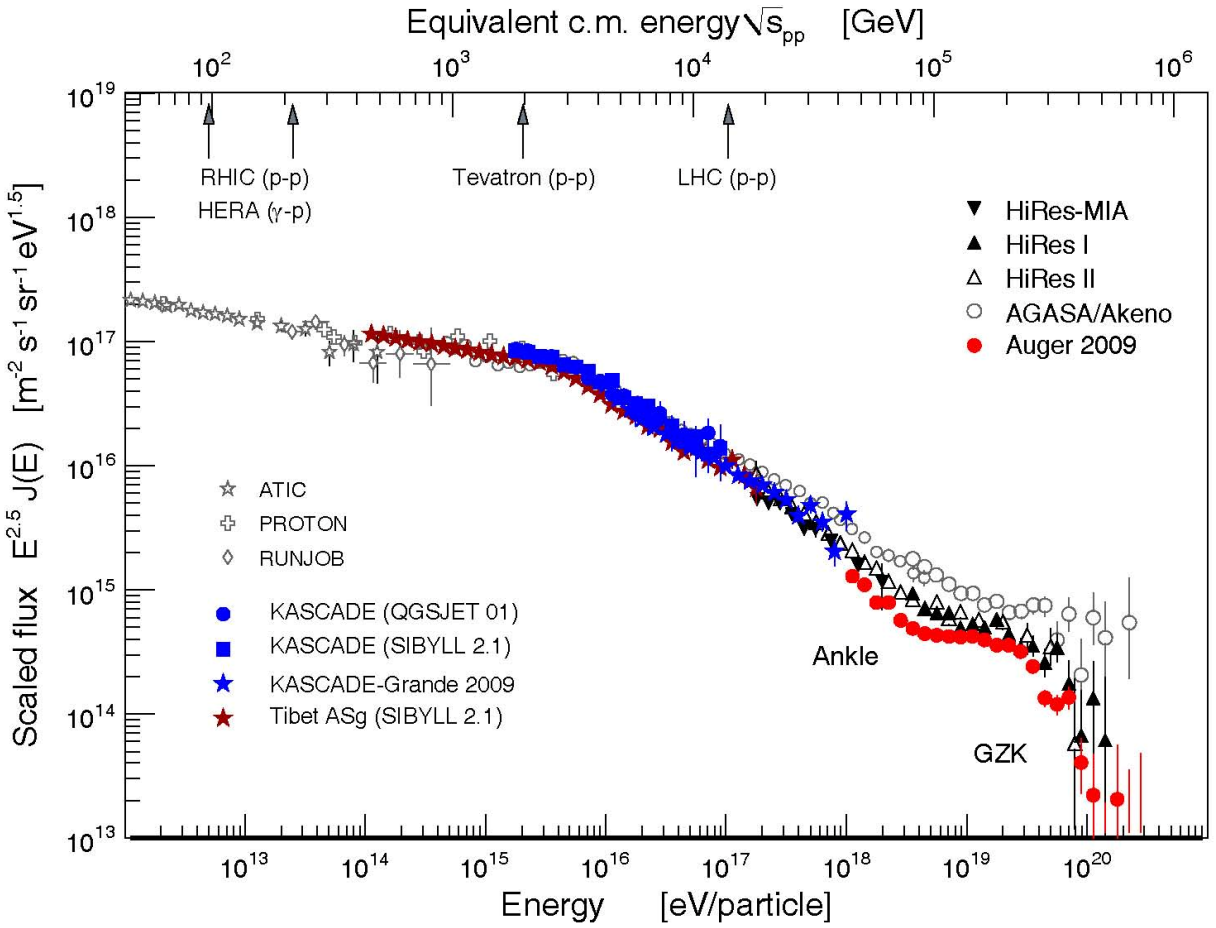

Figure 4.5: Cosmic ray spectrum, showing observations of different experiments. The *Knee* at about 10^{15} eV and the marked *Ankle* at about 10^{18} eV indicate a change in the shape of the spectrum. For a comparison of the reachable energies, accelerator experiments are marked on the upper energy axis. (Matthiae 2010)

of the cosmic microwave background have a very high energy. The threshold photon energy in the proton rest frame for creating pions when the protons are hit by photons lies at 200 MeV. This threshold is reached with a proton energy of about $5{\cdot}10^{19}$ eV. When the pion is created, the cosmic ray looses energy. The fraction of energy loss per pion creation reaction is 1/10. With the mean free path for this reaction of 3 Mpc and assuming that the proton looses always the same amount of energy, the traveling distance of the proton would be limited to 30 Mpc. Of course, the proton does not loose always the same amount but each time less. Still it looses each time energy as long as its energy is above $5{\cdot}10^{19}$ eV, and therefore reaches earth with much less energy than the initial energy. This leads to a decrease of the observed very high energy cosmic rays in the cosmic ray spectrum, because they are shifted to lower energies by the *GZK*-effect.

Cosmic rays are detected by observing the extensive air showers they generate when entering the atmosphere. This process is shown in figure 4.6. When the cosmic ray protons or heavier nuclei hit the atmosphere's molecules, nucleonic cascades are created. First, either neutral π^0, charged pions or secondary nucleons are created. The nucleons can then again create pions in further reactions if their energy is still high enough. The π^0 decay into two γ's which will then create electrons and positrons with pair creation. These leptons then radiate γ's which can do pair creation again if their energy is still high enough. This leads to an electromagnetic shower. The charged pions decay into muons and anti muons

which then decay into electrons and positrons and also produce electromagnetic showers. These showers at TeV can then be observed for example with the *HESS* telescope array, by detecting the Cherenkov radiation caused by the electrons and positrons when moving faster than the speed of light in the atmosphere.
The ultra-high energy (UHE) cosmic rays with energies higher than 10^{18} eV can be observed by the *Pierre Auger* Observatory and the Telescope Array. UHE cosmic rays are very rare and therefore both experiments are designed to have a very large detection area, much bigger than the one of the *HESS* telescope. Both experiments use a hybrid detection method, which includes ground detectors, measuring the distribution of the air shower on the ground, as well as fluorescence detectors which measure the fluorescence light emitted by the air shower.

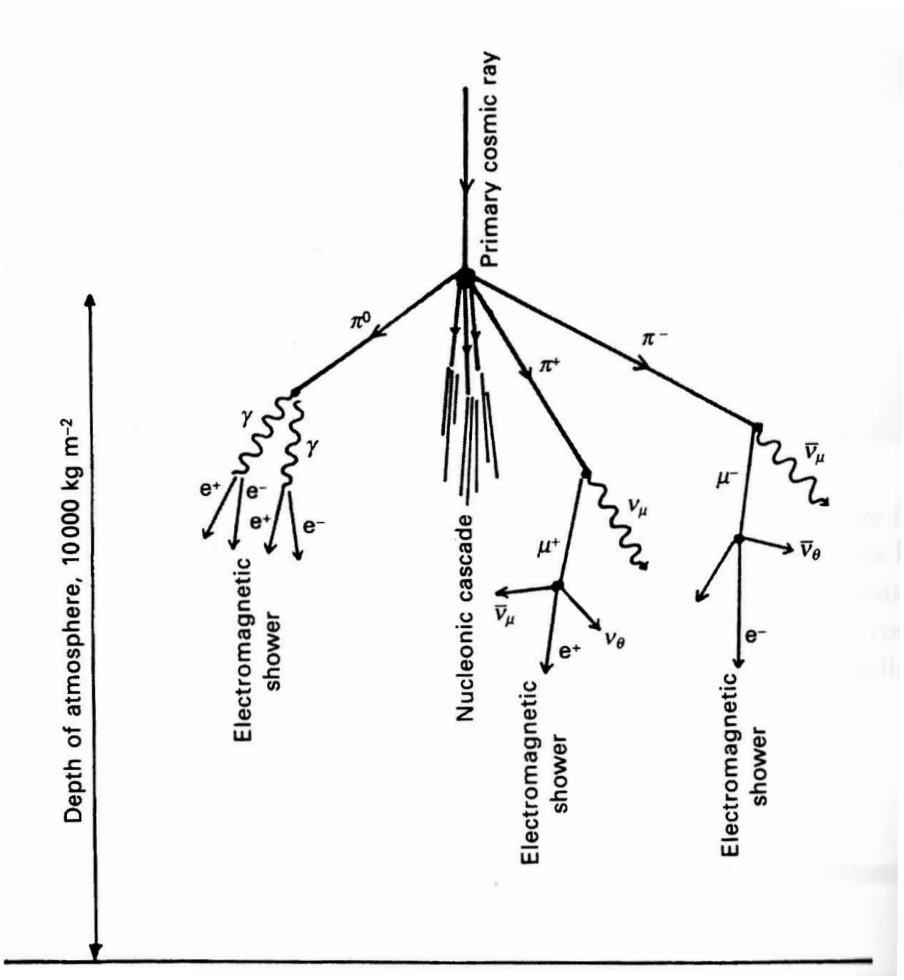

Figure 4.6: Nucleonic cascade shown shematically that is caused by a cosmic ray proton or heavier nuclei when hitting the atmosphere. (Longair 2011)

4.7 Synchrotron Shock Filaments

The lower limit on the magnetic field strength at the shock front of HESS J1731-347 is determined in this work by studying synchrotron shock filaments. To understand what these filaments are and how they can be used to calculate the magnetic field strength, an introduction to this topic is given in this section. Typical shock filaments can be seen for example as thin structures in the outer parts of Cas A in figure 4.7(a)
As explained in section 4.3, the electrons at the shock front are expected to be accelerated with diffusive

shock acceleration. The electrons and the shock front move away relatively from each other. The electrons, expected to have energies in the TeV range, move through the magnetic field at the shock front and as explained in section 4.4 this leads to synchrotron emission. The typical synchrotron frequency ν_{sync} is hereby given by (Ballet 2004)

$$\nu_{sync} = 1.82 \cdot 10^{15} B_{\mathrm{mG}} E_{\mathrm{erg}}^2 \mathrm{Hz}. \tag{4.22}$$

For a magnetic field strength at the shock front of $B = 30$ μG and electron energy of $E_e = 50$ TeV, this would result in a for HESS J1731-347 typical X-ray energy of $E_{X-ray} = 1.45$ keV. The cosmic ray electrons mainly suffer synchrotron losses near the shock front (Berezhko et al. 2003), assuming a magnetic field high enough. The one-dimensional steady-state transport equation for cosmic ray electrons which suffer synchrotron losses under the assumption of a plane shock, has an exponential cosmic ray distribution f as solution, which is given by (Berezhko et al. 2003)

$$f_i(x,p) = f(x=0,p)\exp\left(-\frac{|x|}{l_i}\right) \tag{4.23}$$

for cosmic rays with momentum p in the upstream ($i = 1$ and $x < 0$) and the downstream region ($i = 2$ and $x > 0$). It describes the distribution of the cosmic rays at the shock front in dependance of the cosmic ray momentum p and the distance x to the shock front. The width l_i of the curve is the length-scale for synchrotron losses. Assuming a simple model of a mono-energetic ensemble of electrons as it is done in the calculations in section 7.1, equation 7.2 can be written as

$$f_i(x(t)) = f(x=0)\exp\left(-\frac{|x(t)|}{l_i(\tau)}\right) \tag{4.24}$$

with τ as the in section 4.4 introduced synchrotron loss time $\tau_{loss} \propto 1/B^2$. How the length scale $l_{1/2}$ depends on τ is discussed in detail in section 7.1. Equation 4.24 describes the cosmic ray distribution in dependence of the distance to the shock front, which is a function of the time for a constant electron velocity. From equation 4.24 it can be seen that for a traveling distance x equal to the synchrotron loss length-scale l_2 in the downstream region, only the fraction of 1/e of the initial electrons with an energy E_0 still have the same energy:

$$f_2(x(\tau) = l_2) = \frac{1}{e} f(x=0) \tag{4.25}$$

The typical synchrotron frequency in equation 4.22 depends on the electron energy as $\nu_{sync} \propto E_e^2$. For mono-energetic electrons, the typical synchrotron frequency is therefore also mono-energetic. Since in this model the typical synchrotron frequency is mono-energetic and is radiated by mono-energetic electrons, the number of radiated synchrotron X-rays with this frequency also follows the relation given in equation 4.25. This means that with the simple mono-energetic model the measured X-ray synchrotron emission will show the same synchrotron loss length-scale l_2 for the downstream region as the cosmic ray distribution. Therefore the synchrotron loss length-scale for the cosmic ray electrons can be measured from the X-ray data and then be used to calculate a lower limit on the magnetic field strength at the shock front.
An emission curve similar to one of the emission curves expected from HESS J1731-347 is plotted in figure 4.7(b) and the length scale l_2 is marked.

4.8 Point Spread Function

Due to the wave nature of light and particles, the resolution of an optical system is always diffraction limited and the image of a point source can only be as small as the diffraction image of the point. The

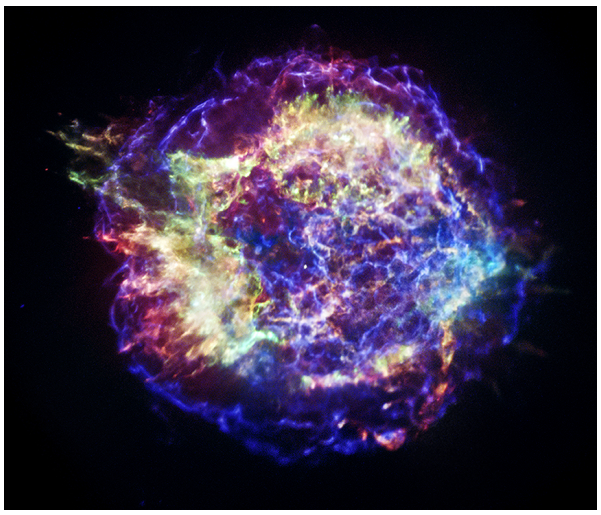

(a) 3-color X-ray *Chandra* image of Cas A

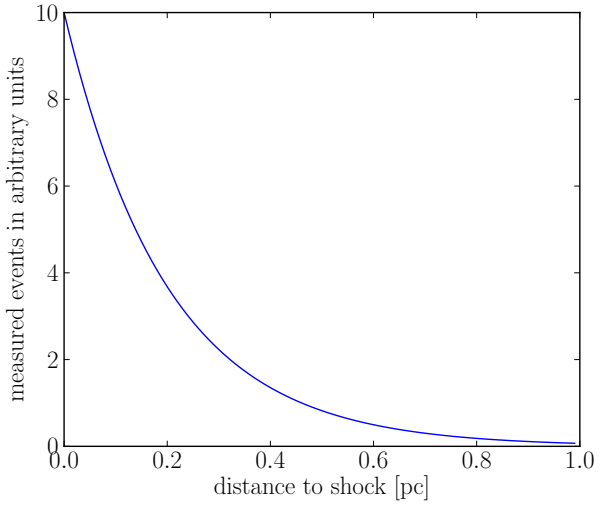

(b) Expected exponential X-ray synchrotron emission profile in the *downstream* region

Figure 4.7: Left: 3-color X-ray *Chandra* image of Cas A[1] (Red 0.5-1.5 keV; Green 1.5-2.5; Blue 4.0-6.0) showing thin synchrotron shock filaments in blue in the outer parts of the remnant. Right: Expected form of an exponential X-ray emission profile of a synchrotron shock filament in case of a mono-energetic ensemble of electrons at the shock front. The marked synchrotron loss length scale l_2 is with a width of 0.2 pc similar to the width found in one of the emission profiles found in HESS J1731-347.

theory of diffraction is based on the Huygens principle which was later extended by Fresnel. It describes that each point of a wavefront can be the source for new waves. These new waves are then super positioned into a new wavefront. The special case of Frauenhofer diffraction can be applied when the image plane is far away from the diffracting object, like it is normally for telescopes and astronomical sources. In this case, the amplitude $U(P)$ of the superposition of waves in a point $P(x, y, z)$ in the image plane, can be calculated by integrating over all areas dS on the wavefront, summing up the amplitude contributions of each point on the wavefront (Schroeder 1999):

$$U(P) = C \int_{\text{wavefront}} \exp[ik(s - R)]dS \tag{4.26}$$

R is the distance between the source and image plane along the optical axis and s is the distance between P and an arbitrary point on the wavefront. C is a constant proportional to the amplitude in that arbitrary point and $k = 2\pi/\lambda$.
For an optical system like a telescope with a circular aperture and therefore like *Chandra*, the optical system is symmetric around the optical axis and the result of equation 4.26 then gives (Schroeder 1999)

$$U(P) = CA\left(\frac{2J_1(v)}{v}\right) \tag{4.27}$$

for a system with zero obscuration, with v as a dimensionless coordinate, A as the area of the aperture and $J_1(v)$ as the first order Bessel Function. In this case, the on-axis PSF is the normalized absolute value of $U(P)$ (Schroeder 1999):

$$\text{PSF}(P) = \frac{|U(P)|^2}{C^2A^2} = \left(\frac{2J_1(v)}{v}\right)^2 \tag{4.28}$$

[1]source: http://chandra.harvard.edu/photo/2013/casa/casa.jpg

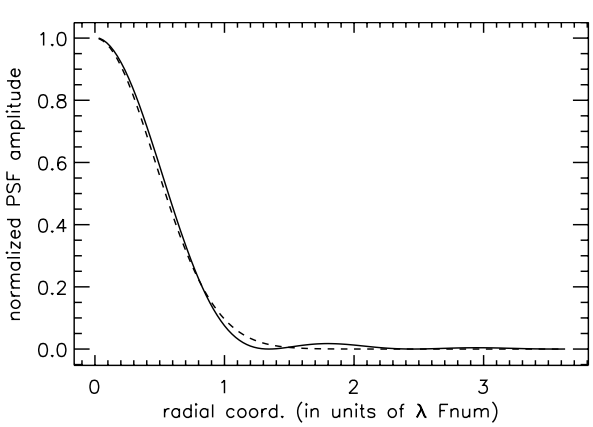

(a) Airy function (line) approximated with a Gaussian (dashed) using the condition $\sigma = \frac{0.44\lambda}{D}$ for the standard derivation of the Gaussian.

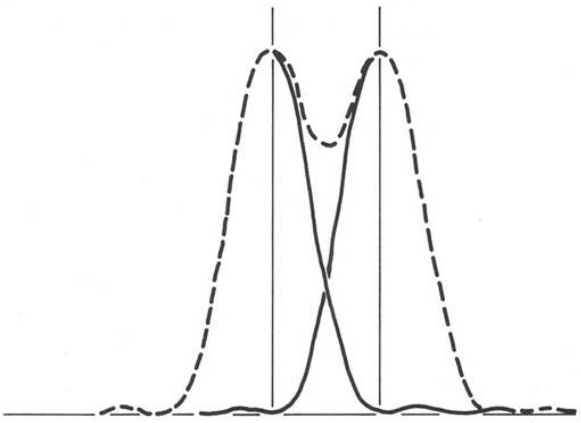

(b) Rayleigh limit, showing the minimal separation of two diffraction images to be separated into two individual images

Figure 4.8: Comparison of Gaussian and Airy curve[1] and the Rayleigh limit[2].

Equation 4.28 gives the "Airy" pattern. For off-axis sources, as explained in chapter 3 the PSF is not only influenced by diffraction but also by other effects.
If one is only interested in the middle peak of the PSF and not in the outer parts, the PSF can be approximated as a Gaussian function, as the middle peak includes 84% of the whole energy included in the beam producing the Airy pattern (Hardy 1998). A Gaussian matching the middle peak can be constructed by using a standard derivation of $\sigma = \frac{0.44\lambda}{D}$ (Hardy 1998) like shown in figure 4.8(a) with D as the diameter of the optical system's lens or mirror.
In figure 4.8(b) the Rayleigh criterion is shown, which is often the used limit for the resolution of diffraction limited optical systems. It describes that the middle peak of the diffraction images of two sources need to be at least $\frac{1.22\lambda}{D}$ apart to be separated. Since this is just a little bit more than the FWHM of $\frac{1.04\lambda}{D}$ of the Gaussian defined above, the FWHM of the PSF is often used as the resolution limit. Of course, this is the theoretical way to describe the PSF of an ideal telescope and in reality there is no perfect telescope, so the real PSF could differ to some degree from this Airy or Gaussian image. What has also to be considered is that in case of a CCD detector like the one used in *Chandra*, the pixel size could limit the resolution of the image.

4.9 Exposure Map

In section 5.2 an exposure map is used to convert the count image into a exposure corrected image in flux units. It mainly corrects variabilities in exposure in different parts of the image due to the effective area varying with position and the motion (dithering, see section 5.2) of the telescope. The exposure map can be seen as an image that serves as a conversion factor between counts and flux. The number of counts from photons with a wavelength inside a range $d\lambda$ accumulated during an effective observation time τ_{eff} which are coming from a sky coordinate $\hat{p}$ and produce a pulse height h are given as (Davis 2001)

$$C(h,\hat{p}) = \tau_{\text{eff}} \int d\lambda \, E(h,\lambda,\hat{p}) S_F(\lambda,\hat{p}). \tag{4.29}$$

[1]source: http://en.wikipedia.org/wiki/Airy_disk#Approximation_using_a_Gaussian_profile
[2]source: http://bki.net/ricc/xtra/wavelettune-filer/image002.jpg

$S_F(\lambda,\hat{p}) = \int d\hat{p}' \mathrm{PSF}(\lambda,\hat{p},\hat{p}')S(\lambda,\hat{p})$ describes the PSF smeared source flux. The exposure map E is given by (Davis 2001):

$$E(h,\lambda,\hat{p}) = \frac{1}{\tau_{\mathrm{eff}}}\int_0^{\tau} dt\, T(\sigma(\hat{p}_t,t)D(\sigma(\hat{p}_t,t),h,\lambda)M(\lambda,\hat{p}_t) \tag{4.30}$$

with $\sigma(\hat{p}_t,t)$ as the sector coordinate in dependance of the sky coordinate. $T(\sigma(\hat{p}_t,t))$ stands for the GTIs (see chapter 3) and $D(\sigma(\hat{p}_t,t),h,\lambda)$ is the probability for a photon with wavelength λ to produce a pulse height h at the detector coordinate σ. $M(\lambda,\hat{p}_t)$ is the off-axis effective area (see chapter 3) at position $\hat{p}$ for a wavelength λ.

To get statistically enough counts per pixel, the sum of counts per pulse height h is build over a range Δh:

$$C(\Delta h,\hat{p}) = \sum_{h\in\Delta h} C(h,\hat{p}) = \tau_{\mathrm{eff}}\int_{\lambda\in\Delta\lambda} d\lambda\, E(\Delta h,\lambda,\hat{p})S_F(\lambda,\hat{p}) \tag{4.31}$$

Assuming now that the effective area is relatively constant in the range Δh, then E is about constant for a wavelength λ_0 corresponding to a pulse height h inside Δh and equation 4.31 can be written as:

$$C(\Delta h,\hat{p}) = \tau_{\mathrm{eff}}E(\Delta h,\lambda_0,\hat{p})\int_{\lambda\in\Delta\lambda} d\lambda\, S_F(\lambda,\hat{p}) \tag{4.32}$$

Here $E(\Delta h,\lambda_0,\hat{p}) = E_0$ is an exposure map for a given energy band containing λ_0. With equation 4.32 the image consisting of counts can be converted to an image containing the flux:

$$\int_{\lambda\in\Delta\lambda} d\lambda\, S_F(\lambda,\hat{p}) = \frac{1}{\tau_{\mathrm{eff}}}\cdot\frac{C(\Delta h,\hat{p})}{E_0} \tag{4.33}$$

For an image containing a broad energy range however, it is unlikely that the effective area of the telescope is about constant over the energy in this range. In this case $E(\Delta h,\lambda,\hat{p})$ has to be divided into several exposure maps with each containing a wavelength range $\Delta\lambda_i$ were the effective area does not vary much. With this, equation 4.32 is written as:

$$C(\Delta h,\hat{p}) = \tau_{\mathrm{eff}}\sum_{\lambda_i} E(\Delta h,\lambda_i,\hat{p})\int_{\lambda\in\Delta\lambda_i} d\lambda\, S_F(\lambda,\hat{p}) \tag{4.34}$$

By introducing weights w_i as

$$w_i = \frac{\int_{\lambda\in\Delta\lambda_i} d\lambda\, S_F(\lambda,\hat{p})}{\int_{\lambda\in\Delta\lambda} d\lambda\, S_F(\lambda,\hat{p})} \tag{4.35}$$

equation 4.34 can be written as

$$\int_{\lambda\in\Delta\lambda} d\lambda\, S_F(\lambda,\hat{p}) = \frac{1}{\tau_{\mathrm{eff}}}\cdot\frac{C(\Delta h,\hat{p})}{E_{\mathrm{weighted}}} \tag{4.36}$$

calculating the flux image with a weighted exposure map $E_{\mathrm{weighted}} = \sum_i w_i E_i$.

4.10 Background in Observations

Instrumental Background

In astronomical observation in X-ray, not only the source events, but also background events are collected with the detector. The instrumental background can consist of different components like particle background which is due to the high energetic particles always present in space but also for example of readout noise. During the observation these particles hit either the detector directly or the surrounding materials, producing fluorescent and Bremsstrahlung X-rays, which then interact with the detector. On

the image when looking at it, these events cannot be distinguished from the real source events. However, like explained in chapter 3 each event is given a grade number which can be used to distinguish real source events from particle events. To measure this kind of background, observation with a shielded detector, or of the dark moon and dark side of the earth are done (Hickox & Markevitch 2006). This way no X-rays of sources can reach the detector. Some spectra of these measurements for different telescopes are shown in figure 4.9. As can be seen here, the background consists of a continuum part, originating from direct hits on the detector and Bremsstrahlung, and the fluorescent lines. The shape of the background spectra varies with time, since it depends on the changing particle environment and the position of the telescope in the orbit. Therefore, standard backgrounds from the measurements described above are available for the different telescopes. The standard background of a telescope can then be scaled to the background of an observation done with this telescope.

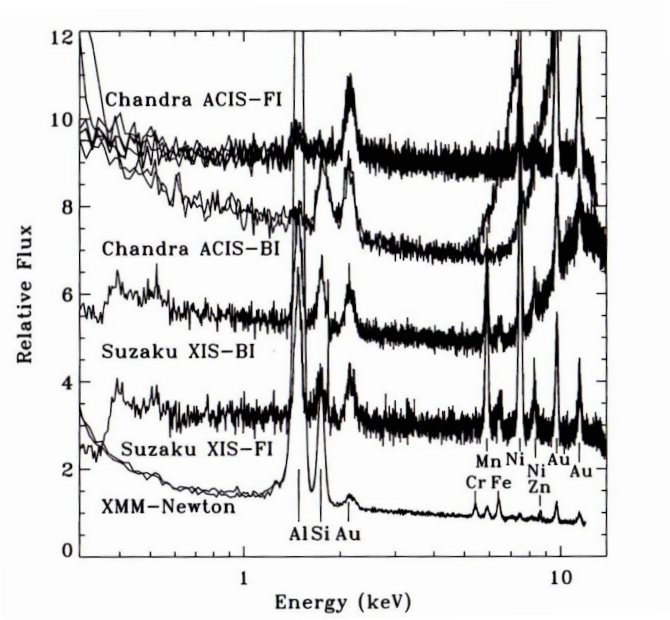

Figure 4.9: Normalized particle background spectra for different telescopes. FI: Front-illuminated, BI: Back-illuminated. (Arnaud et al. 2011)

Other Backgrounds

Apart from the particle background, there are other background influences in an observation. Not only high energetic particles, but also soft protons with an energy of about 150 keV can contaminate the observation. They are influenced by the magnetic field of the earth and their background flux therefore like with particle background also depends on the telescope's position and also its pointing direction. Soft protons are always evident in *XMM* and *Chandra* observations (Arnaud et al., 2011).
Other than that there is also an X-ray background, coming from our own galaxy as well as from extra-galactic sources. The galactic background is mainly due to the *Local Hot Bubble*, a region with hot gas, surrounding the Sun with a radius of about 100 to 200 pc and a part of it is also coming from cataclysmic variables in our galaxy. The extragalactic part is mostly coming from unresolved *Active Galactic Nuclei* (AGN).

Chapter 5

Data Reduction

In the next three sections we describe how the data in the *Chandra* image of HESS J1731-347 are prepared for the fitting of the X-ray synchrotron shock filaments, which is done in chapter 6. To obtain a reliable image, effects originating from the telescope should be excluded or studied in a way so that the result can be used in a fit.
There are three potential major effects that are studied in the following: The background, the exposure and the PSF. In section 5.1 the background in the image is studied. To this aim the energy range of the image is reduced to the range in which the X-ray synchrotron emission is the main contribution, while the higher energy range, where the background is dominating, is excluded. After this also potential high energy particle events are excluded. In chapter 6 the remaining X-ray background is included in the fit function. A background image is prepared in section 5.1, using *Chandra Blank Sky* files, background observations provided by the Chandra X-ray Center. The fit of the background is performed later in section 6.2.
In section 5.2 the image is divided by an exposure map to minimize the influence on the emission profiles of the filaments due to the varying exposure. We perform a spectral study on the image to create a weighted exposure map.
In section 5.3 the influence of the PSF on the image is studied. Depending on the size of the PSF, significant systematics can affect the width of the emission profile and therefore the result for the lower limit on the magnetic field strength. The image of the PSF is simulated at the positions of the different researched structures and is then fitted with a Gaussian to represent the PSF and to get an idea of its size.

5.1 Background Reduction

The main goal for this work is to obtain an accurate lower limit on the magnetic field at the shock fronts of HESS J1731-347. For this, the width of the X-ray synchrotron shock filaments is needed to calculate the limit. Some preliminary work was already done in Rottenanger (2013) and following these results, a more refined analysis on the width, considering different effects on the image, is done in this work. The *Chandra* image of HESS J1731-347 used in the analysis is shown in figure 5.1. The image shows a smaller part of the remnant than in the *XMM* image shown in figure 2.2, but gives a better angular resolution of the shock filaments. This is due to the smaller PSF of *Chandra* compared to the much bigger *XMM* PSF, broadening the structures and giving a worse resolution.
One of the major systematics on the image in X-ray, when observing a source, is the background, consisting of the astrophysical and the instrumental background. In this work three different methods were used to reduce the background in the analysis of the *Chandra* image.

We used the software package *CIAO* (Fruscione et al., 2006). *CIAO* (Chandra Interactive Analysis of

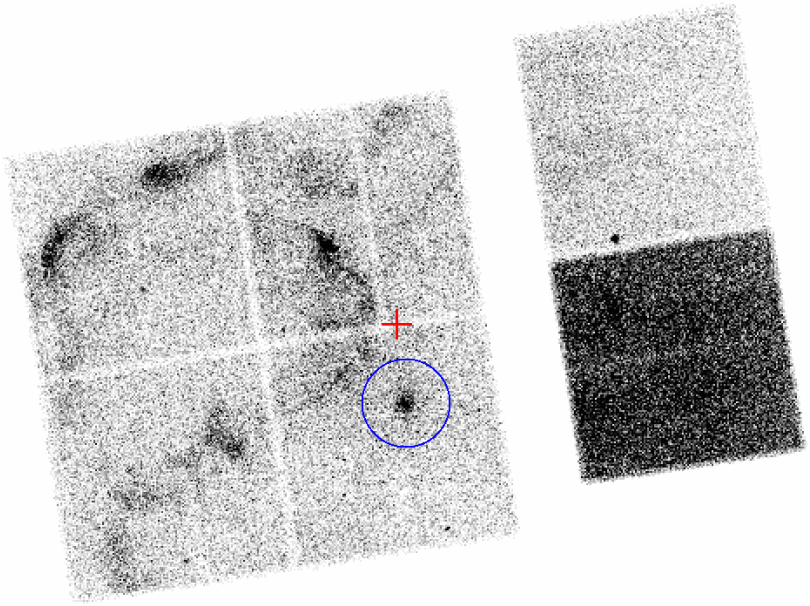

Figure 5.1: *Chandra* counts image of the supernova remnant HESS J1731-347. The image is not exposure-corrected and no background is subtracted. The CCO at the center of the SNR is marked with a blue circle and the optical axis of the observation corresponds roughly to the red +.

Observations) has been developed as an analysis tool especially for *Chandra* observations, since *Chandra* was the first astronomy mission with high resolution 4-dimensional data (Fruscione et al. 2006), including the position, time and energy of a detector event. *CIAO* can also be used for data of other telescopes and also includes the fitting tool *Sherpa* and the plotting tool *ChIPS*.
The results of a *Chandra* observation consist of different files in two folders named *primary* and *secondary* and one observation report which includes the *Chandra* parameters for the observation. Some of the parameters from the report which are used later in the analysis are given in table 5.1. These can be

Table 5.1: Some of the observation parameters given in the observation report on the *Chandra* observation of HESS J1731-347.

Principal investigator	Dr. Gerd Puehlhofer
Observation id	9139
Nominal RA [deg]	263.019117
Nominal Dec [deg]	-34.707126
Livetime [s]	29231.47
SIM focus pos [mm]	-0.781
SIM defocus [mm]	0.0014
SIM translation stage pos [mm]	-220.392
SIM translation stage offset [mm]	-13.2

downloaded from the internet once the proprietary phase of the data is over. The image data is saved in FITS files. FITS is an open standard file format, originally developed by NASA in 1981 and is the standard image format in astronomy. Its main feature is the support of multi-dimensional arrays which allows to contain a large set of data in the image.
The primary folder contains already prepared files that can be used for analysis. For the analysis in this work the relevant files in this folder were the level 2 event FITS file, which contains the detected events minus the already excluded events, and the aspect solution FITS file, which describes the orientation of

the telescope as function of time. The aspect solution file was used later in creating the exposure map. The excluded events are saved in a so called Bad pixels FITS file, the criterias for that will be explained later. In opposite to that, the secondary folder contains pure observation data with, for example, the completely unfiltered level 1 event FITS file that includes every occurred event during the observation, including the bad ones from the Bad pixels file in the primary folder.
To get the best results out of an analysis, it is necessary to use data that has been created with use of the newest calibration data. The observation of HESS J1731-347 (Observation ID 9139) used here was done in 2008 and so the data in the *primary* folder was not created with the newest one. Therefore the *chandra_repro* script provided by *CIAO* was used on the downloaded data, to create a new folder like the *primary* one, containing a new level 2 event file and a new bad pixel file. Using the *CIAO* command *dmcopy*, which can also be used to filter FITS observation data in many ways, figure 5.1 was created out of the level 2 event file with a binning factor of 8.
The image in figure 5.1 shows about a third of HESS J1731-347 with a CCO (marked with blue circle) at the center of the supernova remnant and synchrotron filaments on the outside, marking the outer shock front of the remnant. On the left, the contours of the four front-illuminated *ACIS-I* CCD chips are visible, while on the right side one front-illuminated and one back-illuminated *ACIS-S* chip can be seen. The pointing position of the telescope is roughly marked with a red cross.
This image shows the whole *Chandra* energy range between 0.15 keV and 15 keV and includes background events together with events due to synchrotron emission from the shock filaments. To reduce the background we limited the energy range in the image. For this, a spectrum was extracted from the image. This can be done in *CIAO* with the *specextract* command. To this aim, a source and a background region has to be selected first. The background region can also be selected in a separate background file.
CIAO provides so called *Blank Sky Files*. These are background observations and there are two kinds of them: Observations of high galactic latitude (Doane, 2008), which means outside of the galactic plane and therefore few actual sources, and observations with the detector shielded. Shielded observations show only quiescent background (Hickox & Markevitch, 2006), meaning interactions of high energy particles with the telescopes' materials and directly with the detector. The shielding blocks celestial X-Rays and low energy particles (Hickox & Markevitch, 2006). There are observations for different years from 1999 to 2009 and they are separated into files for the single *ACIS-I* and *ACIS-S* CCD chips. The *acis_bkgrnd_lookup* command in *CIAO* automatically looks up background files for *FITS* files that match the CCD chips used in the observation. *CIAO* recommended the *Blank Sky* observation files of 2005. These files then had to be merged into one image of all included CCD chips of the studied observation, which was done with the *dmmerge* command. For some unknown reason an attempt to merge the files of 2009 did not work. Therefore they could no be used for a comparison, which was unfortunate since chronologically they are the nearest to the observation of HESS J1731-347 of 2008. After that, for actually fitting the background image later and for using the same in *DS9* defined region for the spectrum extraction in both the real observation and the merged background observation, the pointing information in the header of the real observation's *FITS* file was added to the background file's header with the commands *dmreadpar* and *dmmakepar*. After that, the *reproject_events* command was used, which uses the aspect solution file of the real observation, to adjust the coordinates of the background events to those of the real observation's events.
For the selection of the background region, the merged image of the 2005 *Blank Sky* background was used. The selection of the region for the extraction of the spectrum can be done in *DS9* and saved as a region file. *DS9* is a software developed at the Smithsonian Astrophysical Observatory, Cambridge, that can be used to view and analyze FITS images. Even though the thermal emission originating from the CCO in the image has a lot of counts, it is a small number compared to the whole number of counts in the image and the influence on the shape of the spectrum should be negligible. Therefore the whole

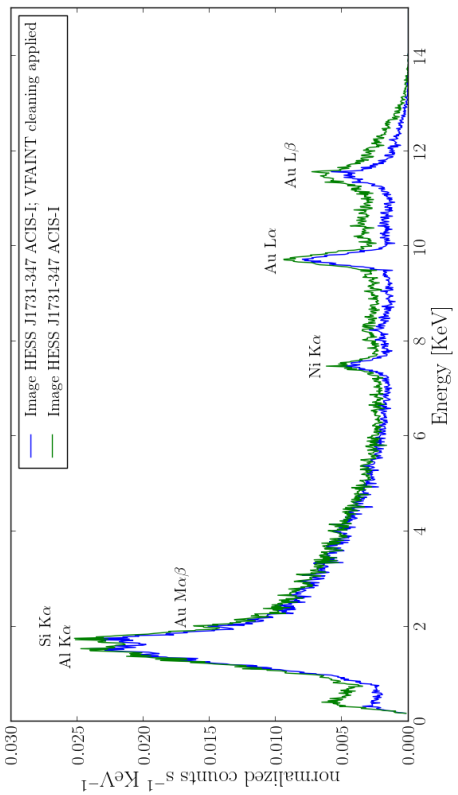

(a) Spectrum showing the whole energy range of the *Chandra* image of HESS J1731. The background is not subtracted and for comparison both the spectrum of the image with and without *VFAINT* cleaning applied (excluding 5x5 grade events) is shown.

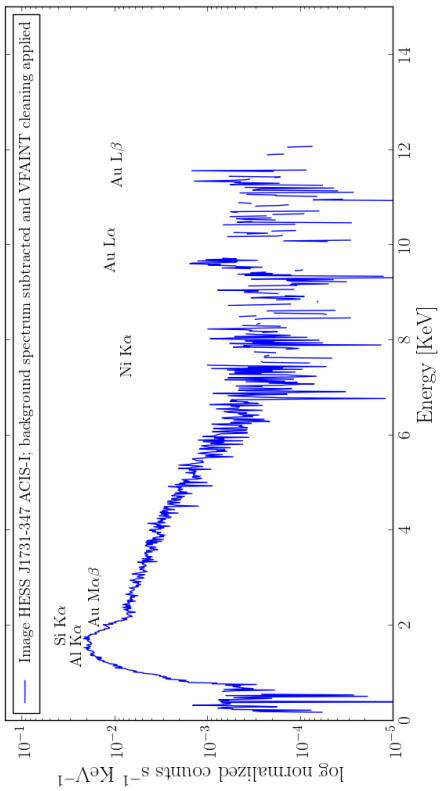

(b) Spectrum showing the whole energy range of the *Chandra* image of HESS J1731. The background is subtracted and the *VFAINT* cleaning (excluding 5x5 grade events) is applied.

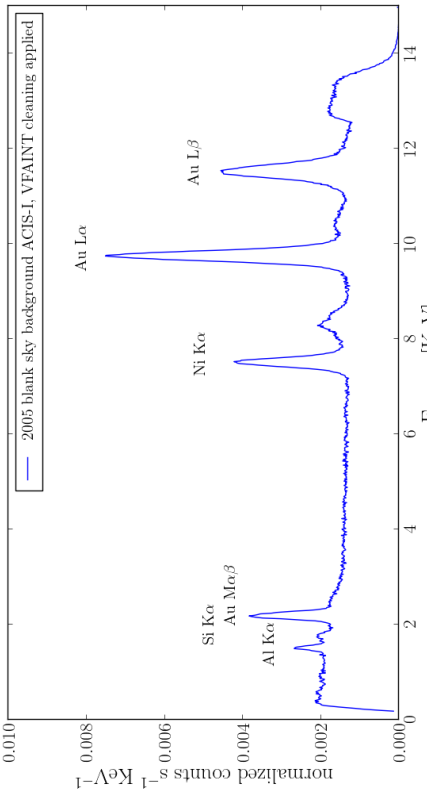

(c) Spectrum showing the whole energy range of the 2005 *Blank Sky* background image with applied *VFAINT* cleaning (excluding 5x5 grade events).

Figure 5.2: With *specextract* extracted spectra from the *ACIS-I* area in the *Chandra* image of HESS J1731-347 and in the 2005 *Blank Sky* background image for comparison of source emission and background emission.

ACIS-I region was used as source and background region.
To open the spectrum file, the software *XSPEC* (Arnaud, 1996) was used. It is a commonly used spectral fitting tool for X-Ray data and is designed to work mission independently. When loading spectral data in *XSPEC*, the background spectrum is automatically subtracted from the source spectrum. To select a reasonable energy range for the further analysis it is important to get an overview of both the image and the background spectrum. Therefore in *XSPEC* a spectrum with included background, with background subtracted and a background spectrum was prepared and the exported spectral data was then plotted in *Python*. They are shown in figure 5.2 with the below explained *VFAINT* cleaning already applied. *Python* is a programming language that is popular among scientists since it is open source and there are a lot of in science useful packages available. A big part of this work was done in *Python*, also since *Sherpa* is based on *Python*. Looking at the spectrum in figure 5.2(a), showing the image spectrum without background subtraction, there are several smaller peaks visible corresponding to emission lines of specific materials. These are fluorescence lines of *Chandra's* materials from being hit by a particle. *Chandra's* effective area is nearly zero in the range of 9 to 12keV, and therefore only high energy particles are detected in this range by interacting with the detector or *Chandra* itself. In the logarithmic plot of the spectrum with subtracted background in figure 5.2(b) what can be clearly seen from around 0.5 keV to about 6 keV is the expected absorbed power law also found in (Abramowski et al., 2011). As explained in section 4.7, it is expected that this is synchrotron emission. Therefore this is the energy range that was used for the further analysis to secure that all the synchrotron emission is included, but also the least amount of unnecessary background events. As explained in section 4.7, the model for calculating the lower limit on the magnetic field strength assumes a mono energetic electron energy at the shock front and therefore also a mono energetic X-ray energy. This means that for a very precise analysis only a small energy range around the peak of the spectrum should be used for the image. This is not possible here because the statistics would then be too bad for a precise analysis.
To further reduce the background in the image, the above mentioned *VFAINT* cleaning was used. This was possible since the observation of HESS J1731 has been taken in the so called *VFAINT* (very faint) mode. In this mode, the grade of an event (see also chapter 3) is not determined with a 3x3 pixel island as in the *FAINT* mode, but with a 5x5 island. It is then possible to flag events as bad events, for example caused by cosmic rays, if an event causes some of the outer 16 pixels to be above their threshold value. These events would not have been necessarily flagged as bad with only 3x3 pixels.
An event detected by Chandra is characterized by 32 bits that can also indicate potential problems like the event caused by a cosmic ray. Making a level 2 event file out of a level 1 file, leads to filtering out bad events with such status bits and these bad events are saved in a bad pixels file. However, this automatic process is based on the evaluation of a 3x3 pixel island grade and the 5x5 grade is not used. This is for security reasons, to not filter out source events automatically. As explained in the *CIAO* manual in bright sources there are some source events marked as potential background events and therefore flagged as bad events.
By using the *chandra_repro* command with the option *check_vf_pha*, the events that are flagged as bad based on the 5x5 grade are also filtered out when creating the new level 2 event file. This was done and to check if there were also events of the synchrotron structures filtered out, two things were done: First the spectrum of the cleaned event file was checked and second, an image with only the excluded 5x5 grade events was created. The spectrum of the the image with and without the excluded events are shown for comparison in figure 5.2(a). As also described in Vikhlinin (2014), the background is reduced in different energy ranges by a different factor, but the shape of the spectrum, especially that of the power law, is still about the same and also the peak at about 0.25keV was nearly completely excluded. The image of the excluded 5x5 events (figure 5.3) shows no noticeable structures compared to the image in figure 5.1. We were thus confident that most excluded events were background events.

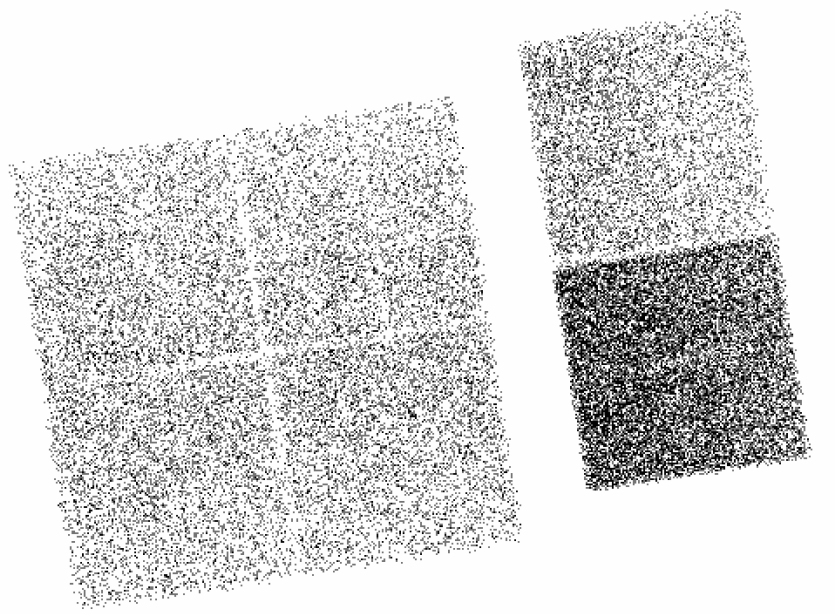

Figure 5.3: Potential particle background events that are excluded of the image when using a 5x5 grade to rate events.

After reducing the image background by limiting the energy range to that of the synchrotron emission and filtering out potential background events with the *VFAINT* mode, we fitted the background with the same method the filaments are fitted later. These background fits are shown in section 6.2. This way a model for the background can be found that can be used in the fit of a filament, to consider the background in the image. To perform a background subtraction for the purpose of imaging analysis, the *CIAO* manual recommends the so called *stowed background factor* C_{bg} by (Hickox & Markevitch, 2006) multiplied by the ratio between exposure lengths, as scaling factor between image and background data. Although not a subtraction of the background but a fit is done here, the background has to be correctly scaled to the observation to get a correctly scaled model for the background. C_{bg} compares the difference in particle background of a real observation and a background observation. As explained above, in the 9 to 12 keV range only particle background is detected. Therefore a comparison of both the source and background observation is possible in the 9 to 12 keV range. Considering the difference in exposure times t_1 (image) and t_2 (background), the complete scaling C_{scale} factor results in

$$C_{scale} = C_{bg} \cdot \frac{t_1}{t_2} = \frac{f_{9-12keV,observation} - 0.0132 f_{9-12keV,readout}}{f_{9-12keV,stowed}} \cdot \frac{t_1}{t_2} \tag{5.1}$$

with $f_{9-12keV,readout}$ being due to readout artifacts, because of the time needed to read out the CCD (Hickox & Markevitch, 2006). This count rate can be obtained from an image constructed with a *Perl* script written by Markevitch (Hickox & Markevitch, 2006). In this case, the count rate was in the range of 10^{-2} and multiplied by the fore factor of 0.0132 this is in the range of 10^{-4} smaller than the the observation count rate and therefore negligible. To obtain the count rate we restricted the energy range in both the observation image and the background image to 9-12 keV, did a *VFAINT* cleaning, and then extracted the spectra with *specextract*. After that, by loading the spectra into *XSPEC*, the count rate is automatically shown, and, in this case, it is important to make sure that the background is not subtracted by *XSPEC*. The count rate for the image of HESS J1731 is $f_{9-12keV,observation} \approx 0.5 \frac{cts}{s}$ and $f_{9-12keV,stowed} \approx 0.49 \frac{cts}{s}$ is the rate for the *Blank Sky* background image of 2005. With this, $C_{bg} \approx 1.02$ is the resulting *stowed background factor* and with $t_1 = 2.923 \cdot 10^4 s$ and $t_2 = 1.55 \cdot 10^6 s$ the scaling factor is $C_{scale} \approx 0.02$. The background image scaled with C_{scale} and with excluded 5x5 grade events, like in

the prepared observation image, is shown in figure 5.4. This is image is used later in section 6.2 to fit the background.

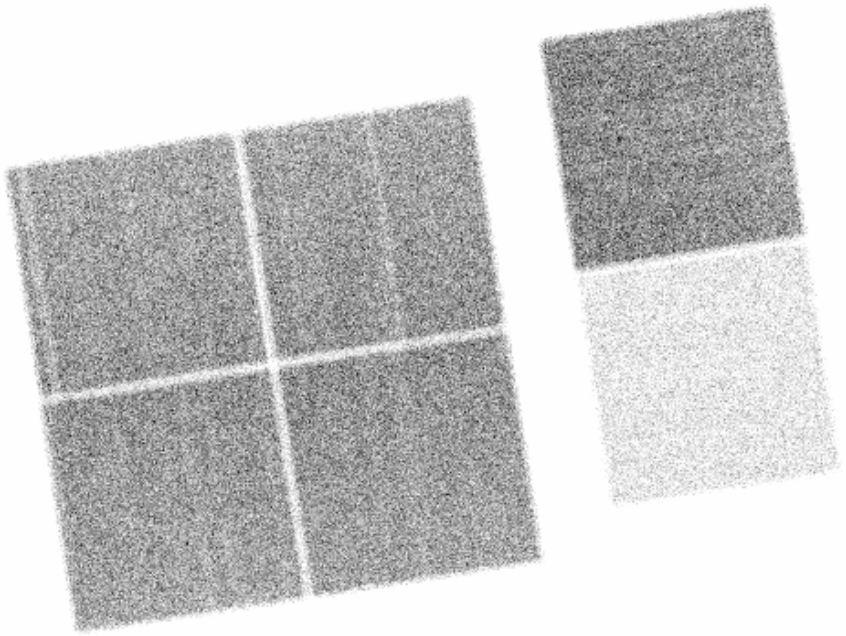

Figure 5.4: The correctly scaled background image from the 2005 *Blank Sky* observation with a energy range of 0.5 keV to 6 keV that is used to fit and model the background in the observation of HESS J1731-347. It shows the same four *ACIS-I* and two *ACIS-S* CCDs as in the real observation.

5.2 Exposure Correction

After studying the background, the next step necessary to obtain the image of HESS J1731-347 for further analysis was to exposure correct the image. This is done by dividing the image by an exposure map and considers the difference in exposure time and effective area (see also chapter 3 and section 4.9) per pixel due to several reasons. Note here that in "*CIAO* terms", the exposure map is a multiplication of the exposure map in section 4.9, including only the effective area, and the exposure time. In section 4.9 only the effective area map, here called instrument map, is included in the exposure map. The unit of the exposure map is in $cm^2 \cdot s \cdot cts/photon$. Therefore the image ($cts/pixel$) divided by the exposure map is in units of $\frac{photon}{cm^2 \cdot s \cdot pixel}$. This gives an image in units of flux instead of events per pixel. One important thing to mention, is that even tough the image used for analysis will be divided by the exposure map, the resulting units will not be in flux here but in "exposure corrected counts". The reason for this is, that there is still particle background included in the image, from the not subtracted background, and these measured events are therefore not from observed X-rays.
The difference in exposure time is a consequence of the dither mode often used in *Chandra* observations. For the reason of averaging signal inhomogeneities and protecting the detector (Nichols et al. 2010) and to avoid empty space between the chip gaps, *Chandra* moves (dithers) around the initial pointing in a Lissajous pattern with a size of typically about 20 arcsec (Nichols et al. 2010) during an observation, like the one shown in figure 5.5. By knowing the Lissajous pattern equation, *Chandra* calculates the real position of the events and corrects the coordinates. As a result of this movement, especially the pixels at the CCD chip edges do not get the same amount of exposure time as the pixels on the inner regions.
As described in chapter 3, the effective area of the *ACIS* varies with position and energy. The dependence on the energy can be seen in figure 3.6. The finished exposure map used to exposure correct the image of

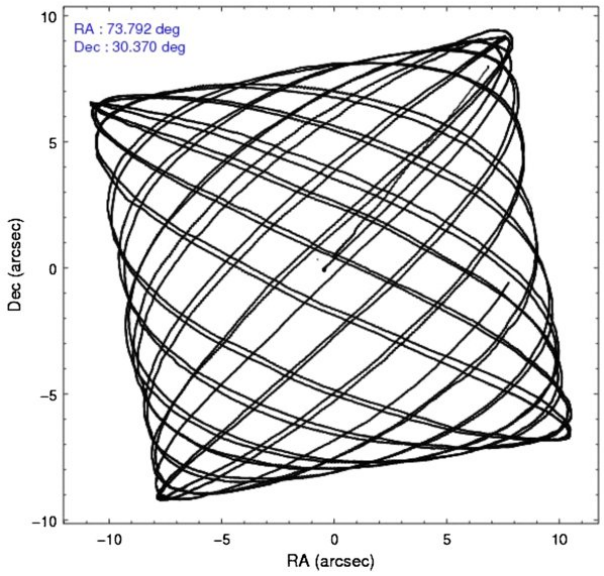

Figure 5.5: Dithering in a Lissajous pattern around the *Chandra* pointing during an observation with activated dither mode. (Nichols et al. 2010)

HESS J1731-347 can be seen in figure 5.6. It also shows how the effective area varies with the position. How it was created will be explained now.

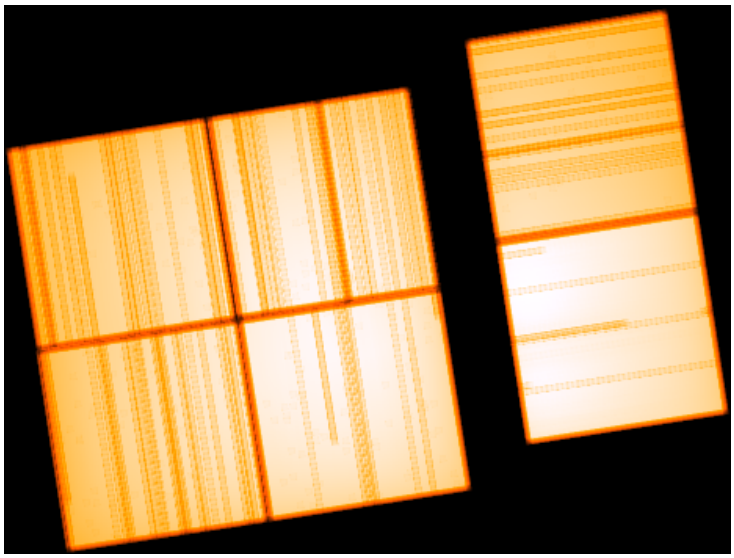

Figure 5.6: Weighted exposure map created with *CIAO* that was used to exposure correct the image of HESS J1731-347.

In section 4.9 we introduced the concept of the unweighted and weighted exposure map. The unweighted is made for one specific energy and the weighted is a superposition of exposure maps for different energies, each multiplied with a weighting factor. As explained in section 4.7 the calculation of the magnetic field strength at the shock front is done with one energy value since the model of mono-energetic electrons is assumed. Therefore an unweighted exposure map could be sufficient here to obtain an exposure corrected image. However, since we search for the synchrotron emission profiles, a weighted exposure map would be necessary if the energy distribution changes significantly inside a shock filament, distorting the real profile. To verify this, a two color image was made of the observation image, showing two different energy ranges. The two ranges were chosen so that each range contains the same amount of counts. This was

checked by loading a spectrum of the 0.5-6 keV image into *Sherpa* and calculating the number of counts inside an energy range with the command *calc_data_sum*. The image contains about 120000 counts and by choosing the two ranges 0.5-2.15 keV and 2.15-6 keV, each of them contains about 60000 counts. In figure 3.6 it can be seen that the effective area also changes significantly above 2 keV, which is another reason for choosing these two energy ranges. The resulting two color image, put together with *DS9*, can be seen in figure 5.7. Along the filaments the color is relatively constant, meaning that the energy stays in the same range. What can also be seen is that the energies get harder from left to right which is due to the change of the absorption column in this direction. Still a weighted exposure map was used since it can be easily obtained with *CIAO* and should represent the broadband distribution of energies in the image better.
With the electron cooling through synchrotron emission one would expect the spectrum to change and to get softer when moving away from the shock front. Therefore it would be more precise to split the image in several energy bands and to exposure correct every energy band separately before adding the energy bands back together. However spectral variation is also not considered in the calculation of the magnetic field and this can give a larger uncertainty than the small changes in the value of the exposure map. Extracting a spectrum at the position of the shock front showed that the peak energy is below 2.15 keV. Therefore a softer spectrum is not influenced by the observed jump of *Chandra's* effective area at 2.15 keV (see figure 3.6).

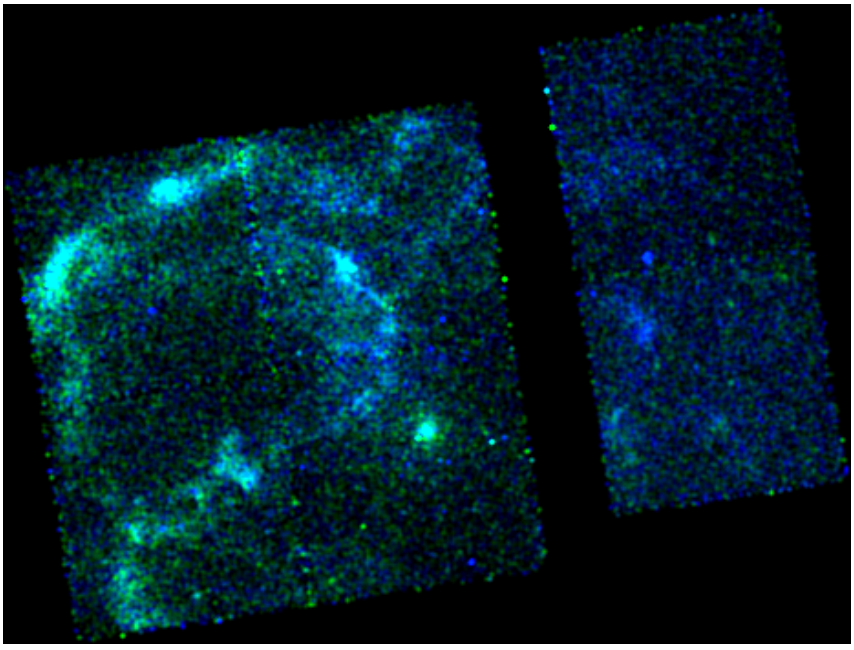

Figure 5.7: Two color image of HESS J1731-347 consisting of two images with different energy ranges: 0.5-2.15 keV (green) and 2.15-6.0 keV (blue).

Creating an exposure map can be done by using the *fluximage* script provided by *CIAO*. For creating a weighted exposure map a source spectrum is needed. To make an exposure map representing the whole source area with all filament structures, the complete *ACIS-I* area was chosen for extracting the spectrum and the same was done in the 2005 *Blank Sky* background image as background region. In case of a weighted exposure map, it is necessary to provide the script with a weights file created by the *make_instmap_weights* script. It provides the weighting factor for each energy for the instrument maps in the superposition for the weighted map. For calculating these factors, the script needs the *Sherpa* source model and an energy range together with energy bins has to be specified. In the case of HESS J1731-347 this model is an absorbed power law. *Sherpa* can also use *XSPEC* models, therefore the model

is a product of the *Sherpa* 1D power law *powerlaw1d* and the *XSPEC* absorption model *xsphabs*, which stands for photoelectric absorption. The *make_instmap_weights* script also needs the spectral index γ of the power law and the line-of-sight column density n_H for the absorption. Both can be found by fitting the source spectrum with *XSPEC* using *xsphabs*powerlaw1d* as model. The fit can be seen in figure 5.8, showing the unfolded spectrum, which gives the spectrum in units of flux. The energy range of 1-6 keV was chosen for the best fit with a reduced χ^2 of $48.68/39 = 1.248$ and therefore a null hypothesis probability of 0.138. The results for the spectral index and the absorption coefficient are $\gamma = 2.31 \pm 0.04$ and $n_H = (1.2 \pm 0.04)E{+}22$. With these values, a spectral weights file was created with *make_instmap_weights*, using an energy range of 0.5-6 keV like in the image used and energy bins of 0.1keV. The script creates a spectrum with the fit values for the chosen model and calculates the weight for each energy bin in the spectrum.

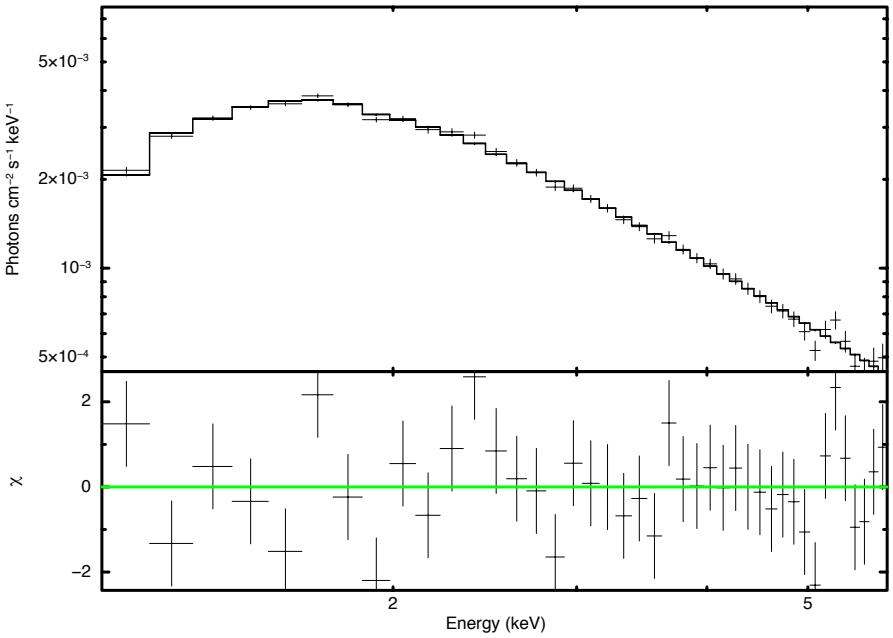

Figure 5.8: Spectrum of HESS J1731-347, showing the energy range of 1-6 keV. It was fitted with *XSPEC* ($\chi^2 = 48.68/39 = 1.248$), showing the residuals at the bottom.

After this, the *fluximage* script was used to exposure correct the image of HESS J1731-347. The script takes either a specific energy, a spectral weights file or predefined energy bands for specifying if the map is weighted or not and additionally a directory containing the observation files or an FITS file as input. The observation image with the *VFAINT* correction was used for this. *Fluximage* first creates a binned image using the event file and then takes the aspect solution file belonging to the event file, which contains the direction vs time information, and creates an aspect histogram for each CCD chip used in the observation. Instrument maps containing the effective area are also created for each CCD. Then the instruments maps are projected into the sky, using the coordinate and time information in the aspect histograms. The exposure maps created for the single CCDs are then merged together to an image fitting the observation image. The before created image is then automatically exposure corrected by dividing the image by the merged exposure map. After running *fluximage*, we have the count image, the exposure corrected image and the exposure map. With the background still included in the image,

it was also exposure corrected even though the particle background does not have to be corrected since the events it causes are not influenced by the optics. The effect of the correction on the background is studied in section 6.2 where the background is fitted by using the 2005 *Blank Sky* background image which is divided by the exposure map.
The exposure corrected image can be seen in figure 5.9 together with the uncorrected image for comparison. Comparing the images, two results can be seen: In the exposure corrected image, the events at the outer CCD edges and at the edges between the CCDs (marked with red arrow) are a lot brighter due to the corrected exposure time and the whole image looks more like one image than the images of several individual CCD chips attached together and looks also sharper. Especially the image of the bottom one of the the two CCDs on the right side, a back illuminated CCD, is no longer much brighter than the other CCDs. One major difference that cannot be seen here, but for example when loaded in *DS9* is the difference in the values of the pixels. In the further analysis, both the uncorrected and the corrected image were used, to see how the results compare.

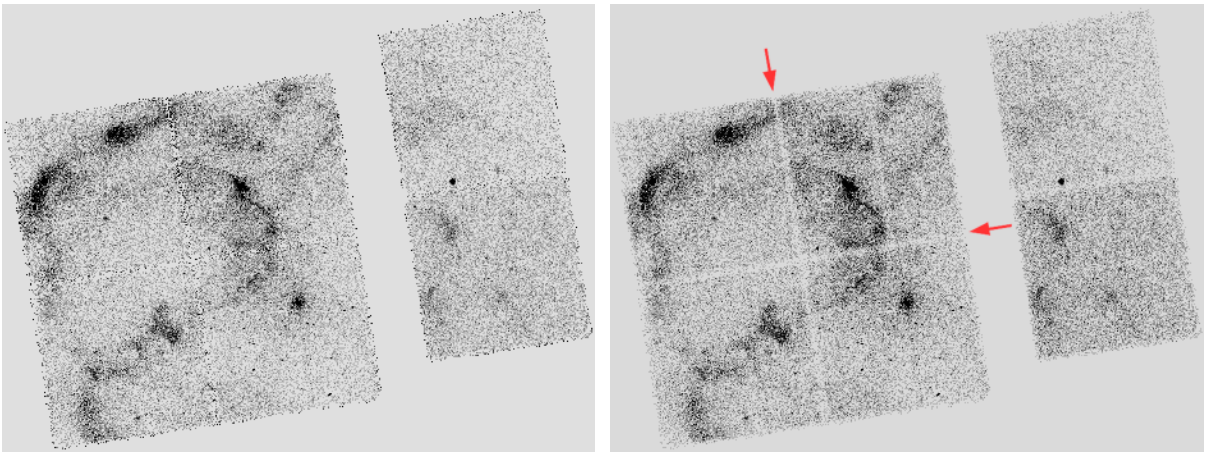

(a) Exposure corrected *Chandra* image of HESS J1731-347, containing the events from 0.5 keV to 6 keV.

(b) Uncorrected image of HESS J1731-347 with an energy range of 0.5 keV to 6 keV for comparison.

Figure 5.9: Corrected and uncorrected *Chandra* image of HESS J1731-347. In both images the *VFAINT* cleaning was applied. The position of the chip edges between the CCDs is marked with red arrows.

5.3 Simulating the PSF

As described in section 4.8, the PSF limits the resolution of a optical system since the image of a point-like source is always only as small as the size of the PSF. In the same way, the PSF influences the image of an extended source, which can be represented by a sum or integral over point sources or delta functions. To carefully estimate the width of the synchrotron emission profiles in the image, the influence of the PSF had to be considered. The size of the PSF depends on the distance to the optical axis. Since the optical axis is not near the outer shock front, the PSF size could have a major influence on the width. The resulting size of "source and PSF" is calculated by a convolution. It is impossible to do a deconvolution without knowing the source function, even when the function of the PSF is known. What is possible and what has been done in a later chapter, is fitting the emission profile with a convoluted fit function, including a constant width for the PSF. What was needed for this is the size of the PSF and an image of the PSF for a fit in *Sherpa*. Therefore in this section the PSF has been simulated and the size of it estimated in different ways.
The Chandra X-Ray Center provides a chart in the *Proposers' Observatory Guide* (Chandra X-ray Center 2013), showing the size of the PSF for the *ACIS-I* as the encircled energy radius versus the distance to

the optical axis for off-axis observations. According to the *Proposers' Observatory Guide* the PSF is asymmetric and this chart only shows the distance up to 10 arc minutes, less than the distance of the filament with respect to the optical axis. Therefore the size was simulated here to see how the sizes in the different directions differ. Furthermore, the curves in Chandra X-ray Center (2013) are calculated for different energies than the peak energy in the HESS J1731-347 image.

To get an actual image of the PSF, simulations were done with *MARX* (Model of AXAF Response to X-rays) (Wise et al. 2003). Developed at the Chandra X-Ray Center at MIT, it is a ray trace software. The results of the simulation are saved in standard FITS file. *MARX* allows the user to specify parameters like source position, position of the optical axis, dithering, quantum efficiency, source flux, observation time and also the shape of the source. The shape can be selected out of five predefined models and four options of file input, like a user defined model. In this work a point and a disk model was used. The shock filament mainly studied in this work is the north-west (NW) filament (top left in the image, corresponding to north-east in the remnant) shown in figure 5.10 in the upper left. It is about 13 arc minutes away from the optical axis, also roughly shown in figure 5.10. Here the PSF could already be at a size where it influences the image significantly. Therefore a point source was simulated at the filaments position, to get an image of the actual PSF, and a disk structure which was used as a circle like shown in figure 5.10. This was done to simulate the PSF of the actual filament since it is believed to be also a part of a circle. A point was also simulated at the position marked with a $\star$ in figure 5.10, since the filament structure there was also under study. However this structure lies near the CCO, about 1 to 3 arcmin away from the optical axis, and therefore the small PSF should not have much influence on the width.

For all simulations several parameters had to be inserted into the *marx.par* parameter file. For both the same parameters were used, except for the source position. The source positions used for the simulations are marked in figure 5.10 by a + and $\star$ for the point simulations and by a circle, marking the radius and the circle's center for the circle simulation. These parameters can be directly obtained in *DS9* when marking the structures.

The position of the *SIM* module during the observation (see also chapter 3) as well as the coordinates of the optical axis were obtained from the observation report in the downloaded folder with the observation files (see also table 5.1). Testing several values showed that the Z offset of the *SIM* module has the opposite sign in the report than in *MARX*. For the exposure time, $2.923 \cdot 10^4$ seconds was selected as in the real observation and the radius for the disk was set to 112.5 arc seconds. For the dithering model, FILE input was selected and the aspect solution file of the real observation was used. The last thing to decide were the source spectral parameters. For the spectrum, also FILE input was selected and the spectrum of HESS J1731-347 was used. The source flux ($photons/(cm^2 \cdot s)$) was set to 0.1. The reason for that was to have about 100 times the amount of average counts as in the real image in the filament, because of better statistics when fitting the PSF image. To get this flux value, simulations with different flux values were done and compared with the real observation image. The simulated points and circle can be seen in figure 5.11. The images have the same binning like the observation image in figure 5.10 with a binning factor of 8.

Considering that a point and a circle without extension was simulated, without the PSF these structures should have a maximum extension of one pixel. As the simulated point PSF at the position of the NW filament is so wide spreaded and the width of the circle is a lot more than one pixel, it can be already seen that the PSF has a considerable size at this position on the image. As expected, the size of the PSF at the position near the CCO is only a few pixels. These structures were modelled by fitting them with a gaussian PSF model.

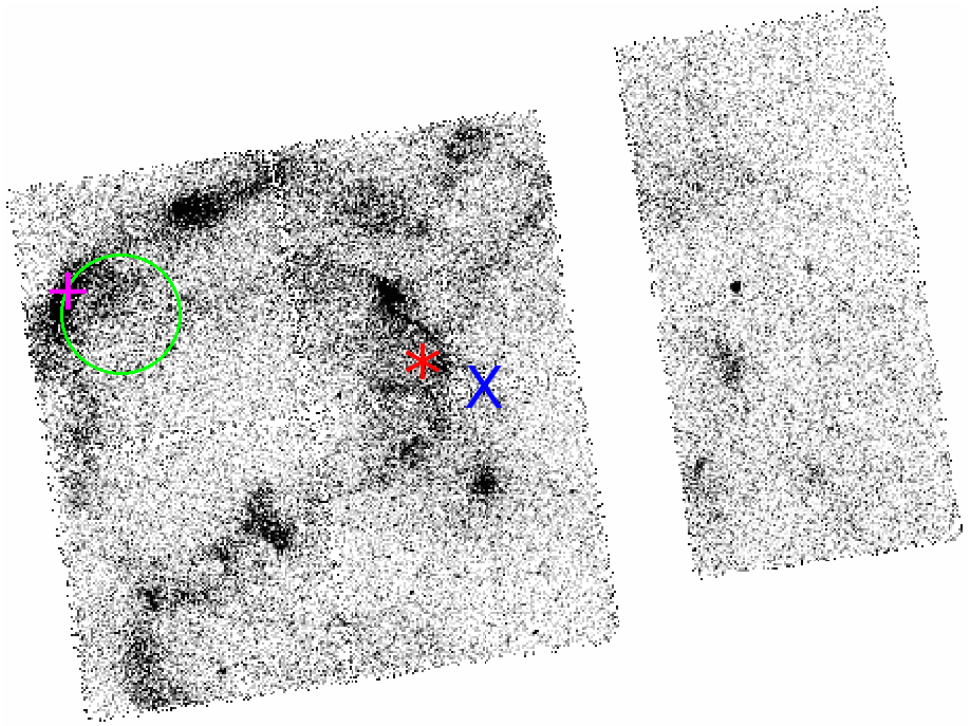

Figure 5.10: Image of HESS J1731-347, showing the markings for the PSF simulation at the structures we are interested in. The + and ⋆ mark the point simulations and the circle marks the circle simulation. The optical axis of the observation is roughly at the position of the X.

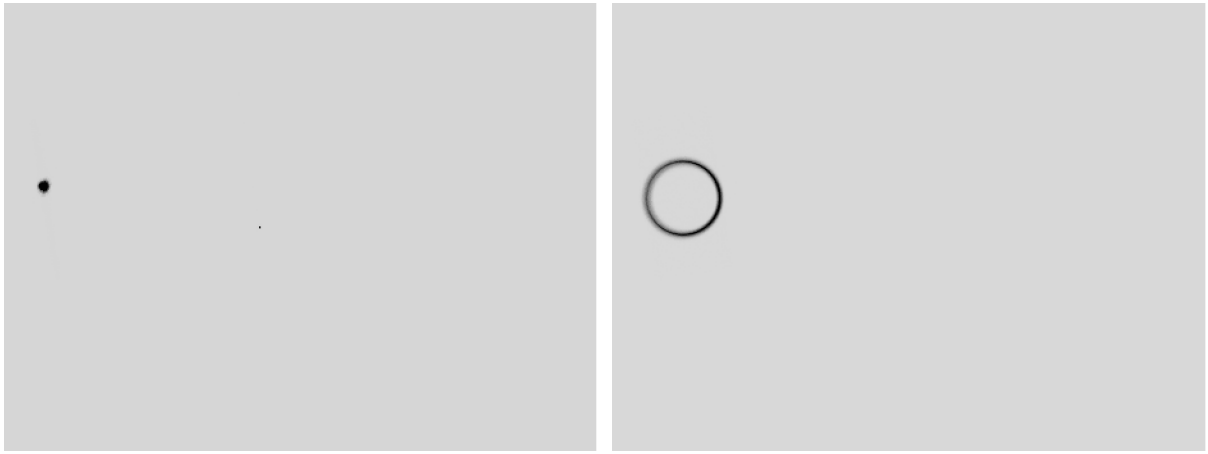

(a) simulated point structures (b) simulated circle

Figure 5.11: With *MARX* simulated structures, showing the size of the PSF at this position.

As fit function, a two-dimensional elliptical rotated Gaussian was used, given by

$$A \cdot exp\left(-\left(\frac{(x(\alpha)-x_0(\alpha))^2}{2\sigma_x^2}+\frac{(y(\alpha)-y_0(\alpha))^2}{2\sigma_y^2}\right)\right). \tag{5.2}$$

The Gaussian is transformed into a rotated coordinate system, rotated by an angle α, by multiplying the coordinates (x, y) and center coordinates (x_0, y_0) with a rotation matrix. The fitting was done in *Sherpa*. For the fit C statistics and the neldermead algorithm was used, since these worked best when comparing the fit algorithms and results. The simulated point structure on the upper left together with the fitted Gaussian and a contour plot of both can be seen in figure 5.12. The best fit standard deviation in y

direction in the rotated system is $\sigma_y = 9.6''$ and in the x direction $\sigma_x = 8.4''$. In average this gives a width of $\sigma_{avg} = 9''$. For the right point the fitting was difficult because of the small size and the distribution of most counts in a small number of pixels, even with less binning. With a binning factor of 2, most counts are concentrated in a square of 4 pixels with a length of about 2 arc seconds. Considering the minimum resolution of *Chandra* of FWHM $\leq 0.5'' \approx 2.35\sigma_{\min}$ (Chandra X-ray Center 2013), a bit more than 1/3 of the side length of this square was selected as the size of the PSF, corresponding to $\sigma = 0.75''$ as a conservative value for the width for the small PSF structure.

Here the concept of the encircled energy fraction (EEF) is introduced. In section 4.8 it was explained that the PSF can be represented by an Airy or Gaussian function. The EEF is the fraction of energy included in a PSF when integrating these functions over a circular area given by the so called Encircled Energy Radius (EER). Of course, when using the Gaussian PSF approximation, this is only accurate when staying inside the Airy middle peak. Integrating a symmetric 2d Gaussian over σ_{avg} as EER gives EEF= 0.46. This value of 0.46 is equal for all 2d Gaussians when integrated over the standard deviation as EER, so the connection between EER and EEF can be used as a general concept to compare the size of the PSF on basis of the standard deviation. This concept will be used later when comparing different PSF sizes. One has to be careful when comparing PSF sizes like this, because not only the position in the focal plane but also the energy of the X-rays change the size of the PSF.

The fit of the simulated circle is done in the exact same way as the real structure later. The simulation of a 1 pixel sharp circle shows smearing due to the PSF, and a fit of the circle provides a fit of the PSF in the circle. This way the same PSF is fitted as the one that should be present inside the NW filament in the real observation and this gives the size of the PSF that has to be considered when the real filament is fitted. The data of the structure in the real image was fitted in the same way as in Rottenanger (2013) by summing up the data of the pixels along the structure, sorting them by the radius and then normalizing them on the number of elements per radius to calculate the normalized average counts. By doing this, one gets a one-dimensional projection of the two-dimensional profile. This principle is schematically shown in figure 5.13. This is done for getting better statistics since the counts are not very high in the real observation. More on the normalization is discussed in section 6.2. The problem of this however is, that one has to know the geometrical properties of the structure that is fitted, especially the radius for specifying the fit region. For the simulation this is known, but not for the real filaments. This problem is considered in the next section. The fitted area together with the resulting measured data and fit curve is shown in figure 5.14. Here the best fit result is $\sigma_{circle} = 8.34''$ as the width of the PSF. The error bars on the data were calculated by normalizing the square root of the unnormalized data by the number of summed up elements per radius.

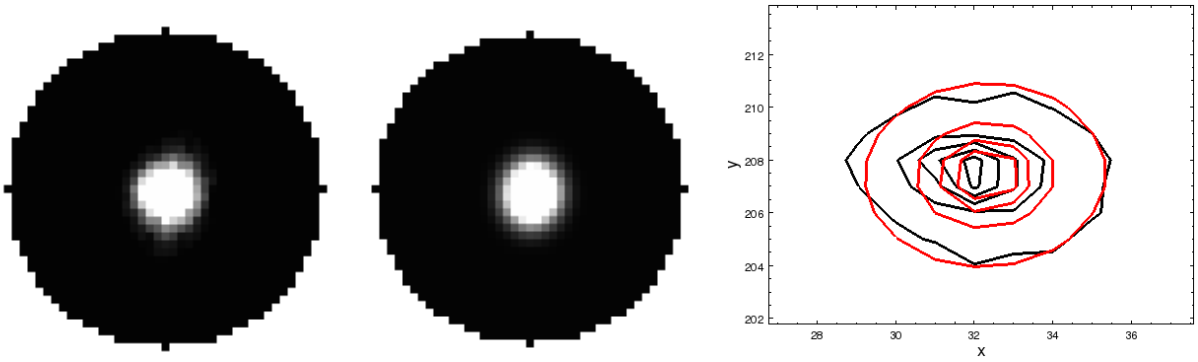

(a) Image of simulated point structure (b) Fit with 2d Gaussian (c) Contour plot of data and fit function

Figure 5.12: Fit of simulated point structure.

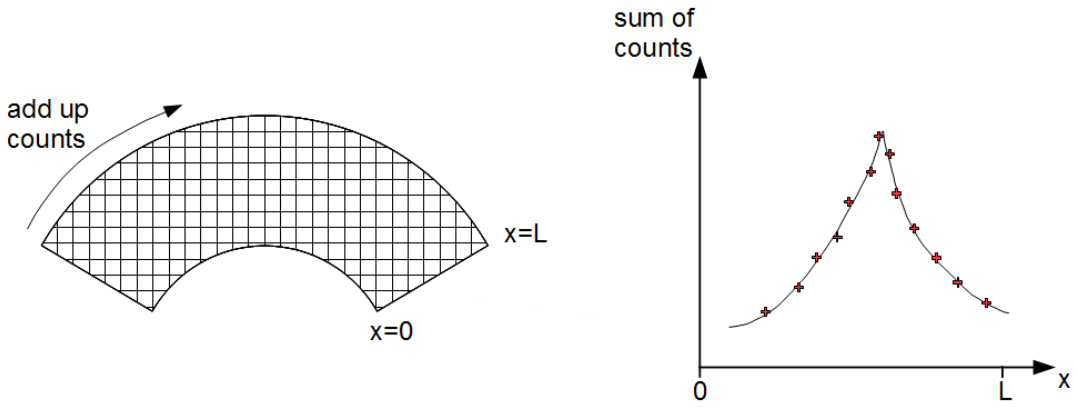

Figure 5.13: Principle of fitting the filament structures. The data of the pixels is summed up along the structure in a pre-defined fit area, sorted by the radius and then normalized by the number of elements per radius to calculate the average counts. By doing this, one gets a one-dimensional projection of the two-dimensional profile.

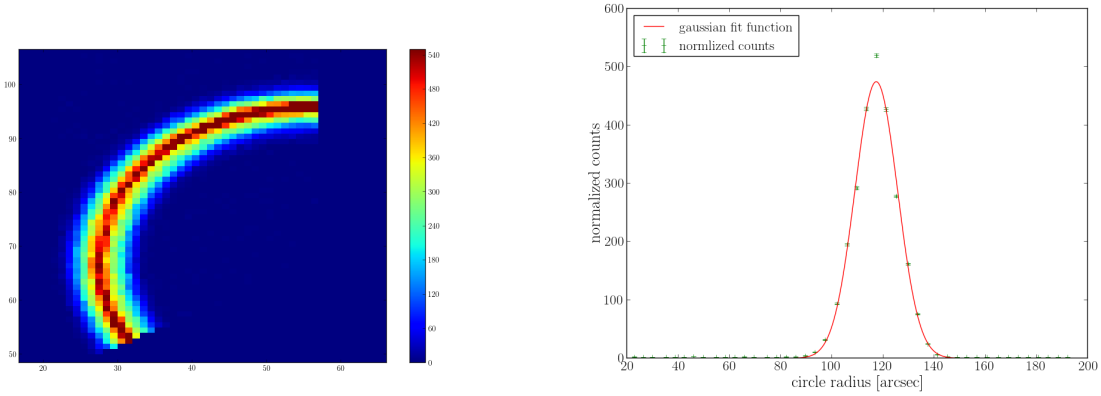

(a) Fit area for fitting a Gaussian to the simulated circle by projecting the data along the circle and normalizing it.

(b) Normalized projected counts and gaussian fit curve

Figure 5.14: Fit of simulated circle structure.

In the fitting of both, the point at the position of the NW filament and the circle, the statistics of the fit were not good, with the reduced statistics being much higher than 1. Therefore, calculation of errors was not possible. This is most likely due to the not entirely gaussian peak with a maximum too high to fit into a gaussian curve. This can be seen well in figure 5.14 where the gaussian curve fits all points well except the one at the peak maximum. Attempts to fit only the inmost 5 data points with a gaussian also showed no good results for fitting the data point at the curve maximum. Therefore it is reasonable to assume that the problem arises because of the maximum.

Comparing the estimated size of the small simulated point PSF for the structure near the CCO to the PSF curve given by the Chandra X-Ray Center given in the *Proposers' Observatory Guide* (Chandra X-ray Center 2013), it can be seen that the value of $\sigma = 0.75''$ obtained for the EER of the PSF is in the correct range for the EER given in Chandra X-ray Center (2013), while still a bit too high. However, it is unlikely that this small PSF size will even have a visible influence in structures with a size of more than 10 arcsec. For the bigger structures, simulated at the position of the NW filament, the *CIAO* tool *psfsize_srcs* was used as comparison. It takes the coordinates, the energy and the EEF as parameter and then produces a region file containing a circle region with the EER corresponding to the EEF as radius that can be loaded for example in *DS9*. For the coordinates of the point simulation on the left,

the synchrotron peak energy of 1.75keV and an EEF of 0.46 results in an EER of 9.9 arcsec. Comparing this to the fitted EER of $\sigma_{avg} = 9''$ and $\sigma_y = 9.6''$ for the simulation with *MARX*, shows that the fitted PSF size is in the same range as the value given by *CIAO* and only slightly smaller. The simulation most likely puts too much counts into the peak maximum, since this is the main difference in figure 5.14 compared to the expected gaussian shaped curve, making the peak higher and the width smaller. With the difference in size between the *CIAO* value and the fitted value being only small, it can be concluded that the simulated image of the PSF can be used in the *Sherpa* fittings in the next chapter, where an image of the PSF is needed to account for the PSF size.

Chapter 6

Fitting of the Filaments

In this chapter the obtained data are used to study a few selected shock filaments in HESS J1731-347. As introduced in section 4.7 in the simple assumption of mono-energetic electrons, the emission profile is given by an exponential function. Therefore the filaments are studied with the assumption of an exponential emission profile.
In section 6.1 the filament structures are fitted with a two-dimensional exponential fit function, mainly to determine the geometrical shape of the structures. The simulated image of the PSF from section 5.3 is used to consider the effects of the PSF in the fit. The result is used in section 6.2 to collect and average the filament emission data in the image using the geometrical properties of the filament structures. The fit function used is a convolution of an exponential profile and a gaussian PSF as it is expected in the image data.
In section 6.3 the same data is fitted again, however here it is considered that the image is a two-dimensional projection of the three-dimensional SNR. First a simulated emission profile, considering this projection effect, is compared to the real emission profile, to test two different geometrical models from the fit in section 6.1 for one of the shock filaments. After this a fit of the emission profile is done with a fit function from integration the three-dimensional emission along the line of sight.

6.1 2D fitting with Sherpa

To calculate a lower limit on the magnetic filed strength at the shock front of HESS J1731-347 by using the synchrotron loss time, the width of the synchrotron emission profile has to be known. Therefore the emission profile has to be fitted in the observation image. However, the statistics are very low in the *Chandra* image of HESS J1731-347. In Rottenanger (2013) the emission was summed up along the emission profile to get and average emission profile with better statistics, as explained in section 5.3. The problem of this method is, that the geometrical shape of the shock filament has to be known to collect the data correctly. The mast important value to know is the center of the circular region, which is used to collect the data. Up to now in Rottenanger (2013), the center of the circle was determined in *DS9* by fitting a circle region manually to the shock filament. However, an incorrect center can have a large influence on the resulting emission profile.
The expected emission profile of a shock filament should have an exponentially decreasing synchrotron emission on the *downstream* side (where the shock already has gone through) and should have nearly no synchrotron emission on the *upstream* side and the curve should rapidly decrease towards zero. The reason for this is that, as explained in section 4.7, one would expect an exponential synchrotron emission profile from the electrons, when moving away from the shock and loosing energy through synchrotron emission. For electrons it is impossible to escape in the *upstream* region and therefore there is no syn-

chrotron emission expected on this side of the filament. In Rottenanger (2013), the profiles were nearly symmetric on both sides, which was either due to some non-synchrotron emission on the upstream side or because of the chosen center of the circle. In section 6.3 it is demonstrated how a wrong fit region can lead to emission that seems to originate from the *upstream* region. Fitting the center manually by eye, there are various possibilities to find a circle that looks like if it fits the profile.
In a supernova explosion, the shock front originating from the position of the progenitor star moves radially outside. Therefore in an ideal model with an isotropic supernova remnant, the shock front can be seen as a spherical shell around the remnant. In this case the shock front should be part of a circle with a center at the center of the SNR. In the special case of HESS J1731-347, the CCO is still at the geometrical center of the remnant. In general however, the compact object in the center of the SNR moves away from the center because of the momentum it gets in an inhomogeneous supernova explosion. In Rottenanger (2013), the data was collected with a small circle region with a center far away from the geometrical center of the SNR. This small circle was found to be the best fit for the filament by trying to fit a circle manually to the filament in *DS9*. Physically it is possible for the filament to get a shape like this, because the shock moves through an inhomogeneous medium which can slow down the shock in some parts. However, as explained above, the found emission profiles turned out to be symmetrical and therefore it is possible that the wrong center for the fitting region was chosen.
To obtain results fitted with the physically correct center, the shock filaments were fitted two-dimensionally, with a fit function where the free parameters consist of the center coordinates, the radius and the emission profile, including the width of the profile. In this fit also the influence of the PSF size on the emission profile's width is considered by using the simulated PSF image made in the chapter before. Aside from finding the correct center, the other important task here for the NW filament was to find out whether the best fitted center lies near the filament or near the CCO. The center near the CCO would be evidence for the NW filament to be part of the outer shock front.
For the fitting, a *Sherpa* script was used. In the first step, the script loads the observation image and then selects the fit region with a region selected in *DS9*.
After that, the coordinate system, the fit statistics and the fit algorithm are selected. Image coordinates were selected, which means units in pixels since then the fit gives the results in the coordinates of the binned image. *cstat* statistics were chosen, which are given as (Doe et al. 2014)

$$C = 2\sum_i [M_i - D_i + D_i(\log D_i - \log M_i)] \tag{6.1}$$

with M_i as the model amplitude in pixel i of the image and D_i as the corresponding data counts. The reason for this choice of statistics is, that compared to the often used chi squared, it does not rely on the statistical error of the data. In a chi squared fit as seen also later in section 6.3 an over- or underestimation of the errors on the data will lead to an over- or underestimation of the errors on the fit parameters. Furthermore, chi squared statistics cannot be used for low counts per bin like in the *Chandra* observation of HESS J1731-347 (Doe et al. 2014). As fit algorithm, both the *simplex* method (Nelder-Mead, see Nelder & Mead (1965)) and the *moncar* method (Monte Carlo method, see Storn & Price (1997)) were used separately in fits and the results compared. Both are recommended on the *Sherpa* website (Doe et al. 2014) for complex models with correlated parameters. While the *simplex* method can calculate fit errors and the *moncar* does not and is less time efficient, *moncar* was still also used. The reason for this is, that while both are global fitting methods, the *moncar* method does probe more points of the parameter space to find the best fit statistic. Since the start parameters for the center are at the position of the CCO, this gives the fit a better chance to still decide for the small circle with the center near the filament, like the one chosen in Rottenanger (2013), instead of ending in a local minimum.
The next step was to include the PSF by loading a simulated PSF image made with *MARX*. The images

shown in the chapter before were used for this. *Sherpa* takes the image and does a FFT (Fast fourier transform) of the PSF and the fit model, convoluting them. After that, a user defined fit function is loaded. The two filaments fitted are shown in figure 6.1. While the NW filament is expected to be at the outer shock front where the forward shock lies, it is not known, what the filament near the CCO is. Assuming an age of 2500 y for the remnant as given in chapter 2, a reverse shock already near the CCO would be very unlikely. Still it is very likely, that this emission is caused by high energy electrons, which were accelerated in a shock emitting now synchrotron. As explained above, it is possible that the shape of the filament is due to inhomogeneous medium the shock crossed. Even though these structures are not at the outer shock front, they were still studied, since they could have a smaller width judging from looking at the observation image and the results in Rottenanger (2013) and this could indicate a higher magnetic field strength. The other reason is that they are much nearer at the optical axis of this observation and as shown in section 5.3 the PSF should have nearly no influence here, which gives a much better resolution here than at the position of the NW filament.

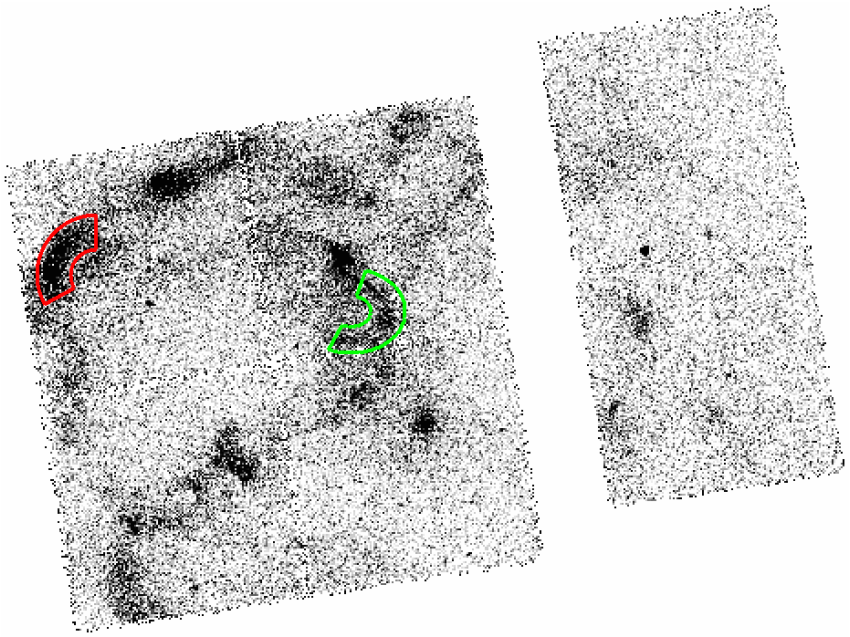

Figure 6.1: The two shock filaments in HESS J1731-347, marked with red and green, that were fitted two dimensional with *Sherpa*.

For the red marked NW filament, the same exponential fit function as in Rottenanger (2013) was used, but transformed into a two dimensional function by transforming the one dimensional x coordinate into a radius $r = \sqrt{x^2 + y^2}$:

$$f(x,y) = A \cdot exp\left(-\left|\frac{\sqrt{(x-x_0)^2+(y-y_0)^2} - r_0}{w_{1/2}}\right|\right) + C \tag{6.2}$$

with A as the function's amplitude, x_0 and y_0 as the center coordinates of the circle, r_0 as the circle radius and $w_{1/2}$ as the width of the emission profile, changing at the maximum amplitude of the profile. C is a constant that represents the background. As shown later in section 6.2, the background can in average be approximated as a constant. Each one of these parameters was fitted and the function was written so that the width $w_{1/2} = w_2$ if $\sqrt{(x-x_0)^2+(y-y_0)^2} > r_0$, for *upstream* and else $w_{1/2} = w_1$ for *downstream*.

Concerning the green marked structure near the CCO, in Rottenanger (2013) it was suspected that fitting this filament with an elliptical fit function could give better results, since the structure looks more

elliptical than circular. Therefore the fitting of this structure was not done with equation 6.2 but with an elliptical function. The two dimensional gaussian ring defined in Xu et al. (2013) was used by leaving the elements making the ring elliptical unchanged and changing the gaussian to an exponentially decreasing function with an absolute value as argument, as in equation 6.2. This gives

$$f(x,y) = A \cdot exp\left(-\left|\frac{(1-k)\sqrt{(x-x_0)^2+(y-y_0)^2}}{w}\right|\right) + C \tag{6.3}$$

$$k = \frac{ab}{\sqrt{a^2(y-y_0)^2 + b^2(x-x_0)^2}}$$

with a as the radius in x direction and b as the radius in y direction. Depending on the fit result, one will be the major half axis of the ellipse and the other the minor half axis. It was fitted in a similar way as the red marked NW filament with two widths, but with the condition $\frac{(x-x_0)^2}{a^2} + \frac{(y-y_0)^2}{b^2} > 1$, which comes from the equation of the ellipse.

After loading the fit function, the script does the fit and plots the fitted function with the best fit parameters together with the residuals and also a contour plot of the fit. The last step of the script is to calculate the parameter errors for a one sigma confidence level in case of the *simplex* fits.

The regions selected for the fit are shown in figure 6.2. For the NW filament, the fit area was limited to only the brighter part since the part following on the north east has less average counts and seems to make a curve of 180 degrees, so it could be a different structure.

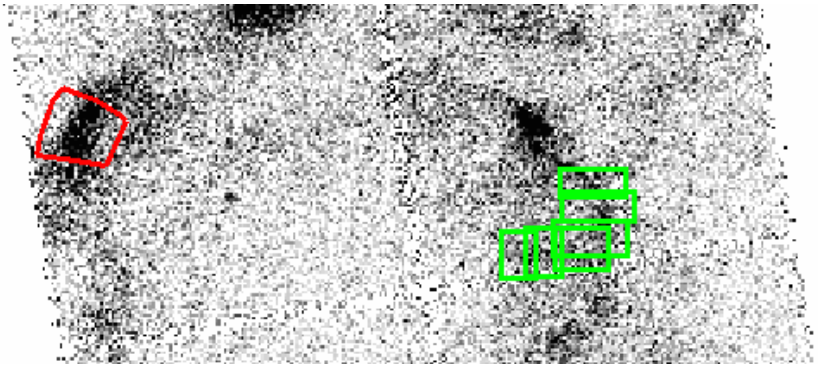

Figure 6.2: Selected fit regions for the 2D fit of the two shock filaments in *Sherpa*.

Both the NW filament and the filament near the CCO were fitted 8 times with the combinations shown in table 6.1. The background was not subtracted here, because the logarithm in the cash statistics does

Table 6.1: Fit combinations used for fitting the NW filament and the filament near the CCO in *Sherpa*

image	VFAINT cleaning applied?	fit algorithm
counts	yes	moncar
		simplex
	no	moncar
		simplex
exposure corrected	yes	moncar
		simplex
	no	moncar
		simplex

not allow negative counts. Therefore the background is included in the constant in the fit function. As seen in the next section, where the background is fitted, on length scales like 100 arc seconds it is about constant in average, while a small gradient can be seen on larger scales, but does not have much influence.

However the not exposure corrected background has also a big negative peak at the chip edges, while the exposure corrected one does not have this due to the correction. The exposure corrected image was normalized by multiplying it with the average pixel values in the exposure map, to have comparable values to the count values in the counts image. For the filament near the CCO, the start parameters were determined with an elliptical region laid on the structure in *DS9*. The NW filament was fitted with a circle as start parameter that has the center at the CCO and a radius big enough to reach the filament on the outer shock front. The shock front that causes the shock filament should also have its origin at the CCO, if it is really a part of the outer shock front and the shock front is not distorted.
For both filaments, in three out of the four possibilities shown in table 6.1 the *moncar* and *simplex* method had about the same geometrical results. However for the NW filament in the *VFAINT* cleaned counts image and for the filament near the CCO in the *VFAINT* cleaned exposure corrected image, the results were greatly different when comparing the *moncar* and *simplex* result in this case. In general, of the eight fit possibilities for the two structures, only two results for each structure have an acceptable reduced statistics and Q-value (probability of getting the same or higher reduced statistic, assuming that the model is true and the fit results are the correct values): For the NW filament the *simplex* fits for the *VFAINT* cleaned exposure corrected and the counts image, and in case of the filament near the CCO the *moncar* and the *simplex* fit with the *VFAINT* cleaned exposure corrected image.These four results are shown in table 6.2 and in figure 6.3 showing the fit regions, a contour plot and the residuals. In all other fits the Q-value is several magnitudes smaller. Comparing first the results for the NW filament, one can see that, while the widths are similar within the uncertainties, for the exposure corrected image the filament is part of a big circle with its center being near the CCO and for the counts image the filament is part of a small circle which has a center near the filament. All other fits of the NW filament also favor the big circle solution but are not trustworthy because of their low Q-value. One reason could be the above explained difference in background shape when the image is exposure corrected and not exposure corrected. For the counts image there is a chip gap with a negative background peak between the CCO location and the filament which could interfere with the fit which has a constant background included. Looking at the Q-value, it is also less likely for the small circle solution to be correct. However there could also be a local minimum issue with the fits which have the center near the CCO, because the fit starts with these coordinates as start values. Therefore in section 6.3 both solutions will again be compared to see which of the solutions is more likely the correct one.
Looking at the results for the filament near the CCO in figure 6.3, the residuals show that the fit failed, even though the reduced statistics and Q-value in table 6.2 seem acceptable. The two different fits also find two different geometrical shapes for the filament. Studying the residuals in *DS9* shows, that some brighter residuals are nearly as high as the corresponding values in the source. Furthermore the distribution of the residuals is not like for the NW filament fits approximately gaussian and therefore in average zero, but differs from a gaussian distribution, by having a lot of high residuals without the corresponding negative counterparts. With this. it seems as if the structure near the CCO cannot be described with the typical synchrotron shock filament shape explained in section 4.7. The uncertainties for the two widths are also very high compared to the fitted value itself in the *simplex* fit, whereas the small uncertainties for the ellipse itself indicate a correct model.
Still, all four results are used in the next section to fit the filaments one-dimensional like explained in section 5.3, by using the geometrical properties gotten in these two-dimensional fits. This will give a look on the average structure of the filaments, since one of the problems here for the two-dimensional fits is, that a constant maximum amplitude is used in the fit function, while the data itself has no constant amplitude.

Table 6.2: Fit results of fitting the shock filaments two dimensional with sherpa. For comparison: The CCO lies at x=232, y=117 and the shock radius would then be about 880 arc seconds. The Q-value gives the probability of getting the same or higher reduced statistic, assuming that the model is true and the fit results are the correct values. VFAINT means that the *VFAINT* cleaning is applied and EXP means that the image is exposure corrected.

	NW filament		filament near CCO	
image	VFAINT EXP	VFAINT counts	VFAINT EXP	VFAINT EXP
fit algorithm	simplex	simplex	moncar	simplex
reduced statistic	$1,089$	$1,185$	$1,065$	$1,059$
Q-value	$0,074$	$0,0018$	$0,063$	$0,08$
amplitude [counts]	$7.48^{+0.5}_{-0.4}$	$9.3^{+0.7}_{-0.6}$	1.42	$1.87^{+2.6}_{-0.4}$
width 1 [arc seconds]	$19.88^{+3.7}_{-3.8}$	$17^{+2.2}_{-2}$	34.52	$51.84^{+172.8}_{-22}$
width 2 [arc seconds]	$13.84^{+3.3}_{-3}$	$8.52^{+2.3}_{-2.1}$	3.2	$31.32^{+79.6}_{-33.7}$
x center [pixel]	$231.3^{+12.6}_{-12}$	$63.1^{+12.5}_{-4}$	174.3	$197^{+1.3}_{-0.8}$
y center [pixel]	$107.1^{+31.2}_{-26.1}$	$192.4^{+3.7}_{-6.7}$	174	$176.1^{+0.6}_{-4.9}$
radius [arc seconds]	$900^{+44.5}_{-48.3}$	$149.5^{+45.2}_{-34.4}$		
constant [counts/pixel]	$0.45^{+0.25}_{-0.3}$	$0.86^{+0.17}_{-0.19}$	1.32	$0.52^{+0.6}_{-2.7}$
semi x [arc seconds]			162	$65.2^{+4.2}_{-6.4}$
semi y [arc seconds]			135.5	$66^{+3.1}_{-3.8}$

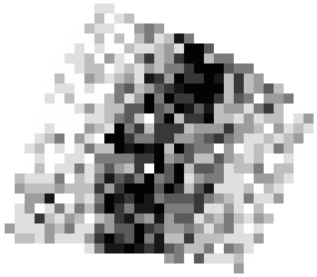

(a) Fit region for NW filament in *VFAINT* cleaned count image.

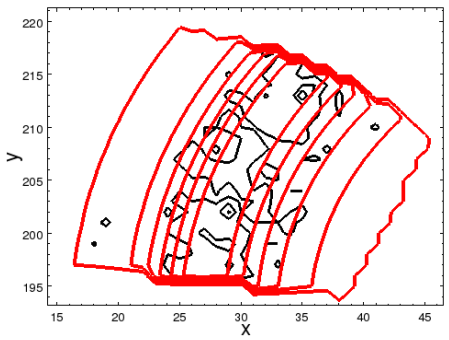

(b) Contour plot of fit and data, fitted with *simplex*.

(c) Residuals

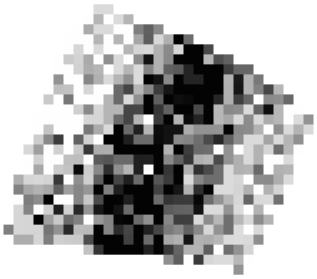

(d) Fit region for NW filament in *VFAINT* cleaned exposure corrected image.

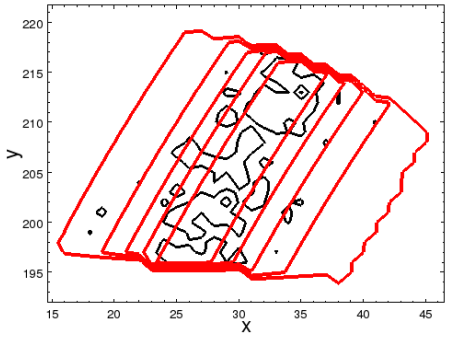

(e) Contour plot of fit and data, fitted with *simplex*.

(f) Residuals

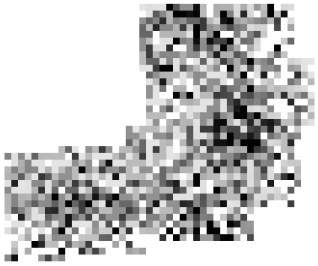

(g) Fit region for filament near CCO in *VFAINT* cleaned exposure corrected image.

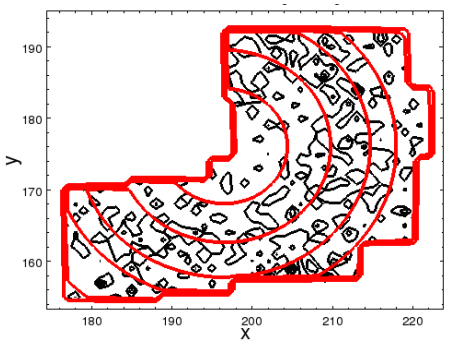

(h) Contour plot of fit and data, fitted with *simplex*.

(i) Residuals

(j) Fit region for filament near CCO in *VFAINT* cleaned exposure corrected image.

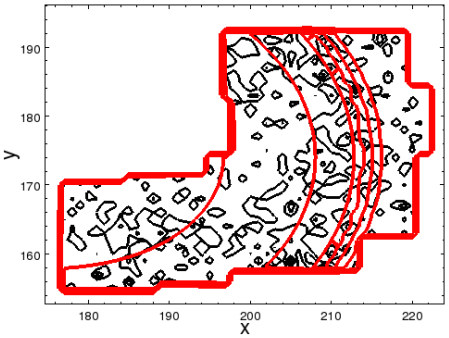

(k) Contour plot of fit and data, fitted with *moncar*.

(l) Residuals

Figure 6.3: Two dimensional fits of two shock filaments with *Sherpa*.

6.2 Fit with Convolution of an Exponential Profile and the PSF

In this section, like in Rottenanger (2013), the shock filaments in HESS J1731-347 are fitted one dimensional after the data is collected and normalized with the method explained in section 5.3. However, a few changes are applied, which should give more accurate results. The studied filaments are the same as in section 6.1, seen in figure 6.1. Instead of finding the center of the circle laid through the NW filament by hand in *DS9*, as done in Rottenanger (2013), here the fitted center found in section 6.1 is used. In addition, not a circular fit region is used for the filament near the CCO, like in Rottenanger (2013), but the elliptical fit results from section 6.1 are used. The most important change is the use of the exponential fit function (Rottenanger 2013), convoluted with a gaussian PSF. This takes into account the influence of the PSF on the filament width, which could be relevant for the NW filament. The width of the PSF is fixed in the fit, so the fit result is the width of the emission profile. For the PSF, the value of $\sigma = 9.9''$ for the NW filament and $\sigma = 0.75''$ for the filament near the CCO is used (see section 5.3). We also take into account the background in the observation. For this the background image is fitted in the same way as the filaments, to get a model for the background emission, which can be used in the actual fit of the filaments. The fit itself is done in *Python* with the *lmfit* package.
To perform the fitting, first the exponential function $f(x)$ of the source has to be convoluted with a normalized gaussian $g(x)$ representing the PSF:

$$f(x) = A \cdot \exp\left(-\left|\frac{x - x_0}{w}\right|\right) + B \qquad g(x) = \frac{1}{\sqrt{2\pi}\sigma}\exp\left(-\frac{(x - x_0)^2}{2\sigma^2}\right) \tag{6.4}$$

A is the amplitude, x_0 the position of the curve's maximum, w the width of the emission profile and σ the standard deviation of the gaussian as its width. B is a constant representing the background in the image, which is a reasonable approximation, as shown below. Since this fit is one-dimensional, the PSF is also one-dimensional here and not two-dimensional like in section 5.3 and 6.1. The following integral calculates $h(r)$ as the fit function:

$$h(r) = \int_{-\infty}^{\infty} f(x) \cdot g(r - x)dx = \frac{A}{\sqrt{2\pi}\sigma}\int_{-\infty}^{\infty} \exp\left(-\left|\frac{x - x_0}{w}\right|\right) \cdot \exp\left(-\frac{(r - x - x_0)^2}{2\sigma^2}\right) dx + B \tag{6.5}$$

This can be integrated by splitting the integral in two regions and considering the absolute value, with one going from minus infinity to zero and the other from zero to infinity. This results in

$$\begin{aligned} h(r) = \frac{A}{2}\Bigg(&\left(1 + \operatorname{erf}\left(\frac{(x_0 - r)w - \sigma^2}{\sqrt{2}\sigma w}\right)\right) \cdot \exp\left(\frac{r}{w}\right) \\ &- \left(\operatorname{erf}\left(\frac{(x_0 - r)w + \sigma^2}{\sqrt{2}\sigma w}\right) - 1\right) \cdot \exp\left(\frac{2x_0 - r}{w}\right)\Bigg) + B \end{aligned} \tag{6.6}$$

which is the fit function used for the fit of the filaments. In equation 6.6 the amplitude not only depends on A but also on the width w because of the error function. The emission profile is fitted with two functions like equation 6.6, with two different widths for each side and with the condition to change at the maximum. Therefore the amplitudes of both functions have to be the same at the maximum. With the first function $h_1(r)$ like equation 6.6 having an amplitude factor A_1 and a width w_1 and the second function $h_2(r)$ having an amplitude factor A_2 and a width w_2, with the condition $h_1(x_0) \stackrel{!}{=} h_2(x_0)$ this

gives:

$$A_2 = \frac{A_1 \left(\mathrm{erf}\left(\frac{\sigma}{\sqrt{2}w}\right) - 1 \right) \cdot \exp\left(\frac{x_0}{w_1} - \frac{x_0}{w_2}\right)}{\mathrm{erf}\left(\frac{\sigma}{\sqrt{2}w_2}\right) - 1} \tag{6.7}$$

This condition was therefore included in the fit function.

The selection and collection of the data in the image is done as in Rottenanger (2013). In *Python*, the area of the data to fit is selected by specifying a center of the circle or ellipse and an inner and outer radius as well as a range for the angle between 0 and 2π. The *Python* script then goes through the image and collects only the data contained in the by angle and radius specified area. The data with the same radius is summed up and afterwards divided by the number of summed up elements per radius, to get a curve with the average emission profile. The reason for this normalizing of the profile is that the theory expects a plane shock front. Here however, the shock is curved in the image and contains more pixels in the outer regions of the synchrotron structure than on the inner regions. Still, to have good statistics, the data of the filaments has to be summed up along this curved structure. In this case the curvature could act as a further compression additional to the normal shock compression of the medium. Therefore the emission is normalized, to get the emission profile of a plane filament structure. The difference between normalizing the data and not normalizing it was studied in Rottenanger (2013) and the result was that the influence is small.

For the NW filament, which is on the edge of the CCDs, it was ensured that only the pixels on the CCDs were collected. In the case of the elliptical filament near the CCO, the data was also selected and sorted with a radius. For that, not the image itself, but the elliptical coordinates of the pixels relative to the selected center were stretched to a circle by dividing the y coordinate by the ratio of the length of the two axes of the ellipse.

The collected data was then fitted with the *Python* package *lmfit*. It can use different fit methods provided by *scipy.optimize* but was tested most with the least square method. Compared to *scipy.optimize* it adds a lot of features. The fit parameters and results are not just numbers, but objects with different attributes like for example the reduced statistics, that can be called with a command. Another feature is the possibility to add boundaries to the fit parameters, which is not possible in the *scipy.optimize* package alone. These were programmed like the boundaries in the *Minuit* (James & Roos 1975) fit routine developed at CERN.

First the background was fitted to get a model for the fit function for the filaments. This is important because the background is also exposure corrected when the image including the background is exposure corrected. Therefore a comparison of both the exposure corrected and the not corrected background was done to see the influence of the exposure correction. For the filament near the CCO the background was assumed to be constant. This assumption is reasonable since the radius of the filament structure is small compared to the whole image size and the filament is near the optical axis. The background emission itself should be constantly distributed in the image for long enough exposure times and the vignetting correction should not have much effect on the background at this position in the image. The exposure correction of the background even has the advantage of correcting the exposure at the chip gap near the structure.

In case of the NW filament however, for the big circle model obtained from the two-dimensional fit, the filament radius is with about 900 arc seconds nearly as big as two chip edges together which is about 1000 arc seconds. With this long distance and the position of the filament on the outer part of the *ACIS-I* region, the vignetting correction could have a noticeable effect on the background. Furthermore a direct line from the position of the CCO, which is near the fitted center for the big circle model, to the NW filament has to cross the center of the *ACIS-I* region where all CCDs meet and the biggest chip gap lies.

A comparison of corrected and uncorrected background therefore shows if the exposure correction really corrects this big chip gap and also how this gap could have influenced the two-dimensional fit of the uncorrected image leading to the small circle solution for the NW filament. The fit of the background is shown in figure 6.4. The image of the 2005 *Blank Sky* background was used in two different versions: Both images scaled to the observation of HESS J1731-347, but one is exposure corrected and the other is not. The same center and radius as shown in table 6.2 for the big circle model of the NW filament was used for the selection of the fit area. The error bars in figure 6.4, 6.5 and 6.6 are calculated by assuming that the data is Poisson distributed and therefore the error is the square root of the unnormalized counts C. The errors f for the unnormalized exposure corrected counts $F = C/Exp$, with Exp as the exposure map, were calculated as relative errors by using the error σ on the counts:

$$\frac{\sigma}{C} = \frac{\sqrt{C}}{C} = \frac{1}{\sqrt{C}} \stackrel{!}{=} \frac{f}{F} \quad \Longleftrightarrow \quad f = \frac{F}{\sqrt{C}} \tag{6.8}$$

The counts C, flux F as well as the corresponding errors σ and f were then normalized by dividing them by the number of summed up elements per radius.

As fit function for the averaged background a straight line is assumed, which is a good approximation as seen in figure 6.4. The plotted data shows the averaged background emission from near the CCO up to behind the NW filament and therefore shows about the range of 1000 arc seconds. In figure 6.4(a) the not exposure corrected count background is shown together with a fit of the background. The fit covers roughly the same range as the small circle filament model given in table 6.2. Figure 6.4(b) shows the exposure corrected background with a fit of the background. The fit range used is the same range as in the fit of the NW filament in the big circle model, given by a range of about 400 arc seconds. The fit results are shown in table 6.3. Comparing the background curves in figure 6.4(a) and 6.4(b), one can observe the differences of exposure correcting the background or not. The uncorrected background shows the big chip gap in the left part and also the influence of the outer end of the CCD is visible on the very right. In the exposure corrected background the curve is flat and these influences are not visible. Another difference, probably caused by the vignetting correction, is that the sign of the gradient in counts changes: In the uncorrected background in figure 6.4(a) the average number of counts slightly decreases going from left to right which means from the CCO to the NW filament. In the exposure corrected background in figure 6.4(b) the counts slightly increase in this direction. The same is shown in table 6.3 by the slope parameters of the fitted line. However, these slope parameters also show, that it is reasonable to approximate the background in the fits of the NW filament in both the big and small circle case as a constant. The peak value in the emission curve of the NW filament is of the order of 5 counts in the uncorrected image and $5{\cdot}10^{-7}$ exposure corrected counts in the exposure corrected image. The background constant is about one order of magnitude lower than these values and the slope value in both cases even several orders of magnitude lower. Even when multiplying the slopes given in table 6.3 by the fit range of about 150 arc seconds in case of the small circle model or 400 arc seconds in case of the big circle model, the change in the background constant would still be one order of magnitude lower than the constant itself and would not really have an influence on the fit of the filament. Therefore the background is approximated with a constant in the fit.

As already discussed in section 6.1 the effect of the big chip gap seen in figure 6.4(a) could be the reason for the fit to select the small circle model when fitting the structure. However this is still only a difference of about 0.1 counts in average compared to the background on the CCDs and therefore it is also possible that it is not the reason but for example a local minimum problem.

The fit results with the fitted widths and the fit area for the NW filament and the filament near the CCO can be seen in figure 6.5 and 6.6. The same center, radius and ellipse axes as shown in table 6.2 were used for the selection of the fit area. For the fit of the filaments, the *VFAINT* exposure corrected image

Table 6.3: Fit result for fitting the background in the exposure corrected and uncorrected scaled 2005 *Blank Sky* background image with a straight line. As fit range in the uncorrected image roughly the fit results of the small circle model from table 6.2 were used and for the exposure corrected image the range of the big circle result.

	background constant	background slope
uncorrected average background	0.38	-0.0001
exposure corrected average background	2.56E-8	1.4E-11

was used.

From the model for synchrotron shock filaments introduced in section 4.7, on the *downstream* region an exponential decay is expected, while there should be no emission present in the *upstream* region. However, it is unlikely for the filaments to have a perfect shape with no inhomogeneous parts on the *upstream* region. Therefore, when summing up the emission along the filaments, these inhomogeneities will lead to the shift of some *downstream* emission to the *upstream* side of the curve. Therefore emission is also in the *upstream* region of the curve to some degree, but most of it should not be real.

For the filament structure near the CCO, the two-dimensional fit in section 6.1 suggested two different models. As already suggested in Rottenanger (2013), there are two different possible shapes for the filament near the CCO. One model describes a small filament with a strong curvature which was found in the *simplex* fit in table 6.2 and the other one, obtained with *moncar*, describes a long filament which starts in the upper CCD, crosses the chip gap and continues in the lower CCD. The fit of the model with the long filament is shown in figure 6.5(b). The emission curve is similar to what expected, with small emission on the *upstream* side and a wider emission on the *downstream* side. The curve looks similar to the one found with a similar model in Rottenanger (2013). As calculated in Rottenanger (2013), a width this big for the *downstream* region suggests a lower limit for the magnetic field much lower than 12μG. However, the shock front should be much further outside in the remnant. Therefore the shock conditions do not necessarily apply here and it could be possible for the magnetic field strength to be lower than the 12μG from the shock compressed medium. Still, as implied by the residuals of the two-dimensional fit, another possibility is that the model is wrong in some way and the emission curve does not correctly represent the structure in the image.

The fit with the model for the smaller filament structure is shown in figure 6.5(d). The emission looks very symmetric which should not be possible in theory. The width of the *upstream* emission, which is nearly as wide as the emission in the *downstream* region, suggests that the emission is summed up with the wrong model. However, for both emission curves in figure 6.5, these arguments assume that the same emission curve is expected here as at the outer shock front. Since the outer shock front is not near the position of these structures, it is difficult to exactly determine what to expect here for the emission curve.

The fits of the NW filament are shown in figure 6.6. The fit with the small circle model is shown in figure 6.6(b). The residuals, which show systematics, the high χ^2 and also the fact that boundaries had to be used for several fit parameters for the fit to work, suggests that used fit function is not a good model for the data. Also the peak of the data is not represented very well by the fit curve. The fit using the big circle model is shown in figure 6.6(d) and does fit the emission curve well, with some residual around the peak. Assuming that there is no error in summing up the emission of the filament and that the correct physics is applied, another explanation is needed. Comparing the curves for the NW filament with the projection model proposed by Berezhko & Völk (2004) and Ballet (2004), shows intriguing similarities to their curves. The model is studied in the next section. The filament near the CCO is not further studied, since the projection model can only be applied to a filament at the outer shock front.

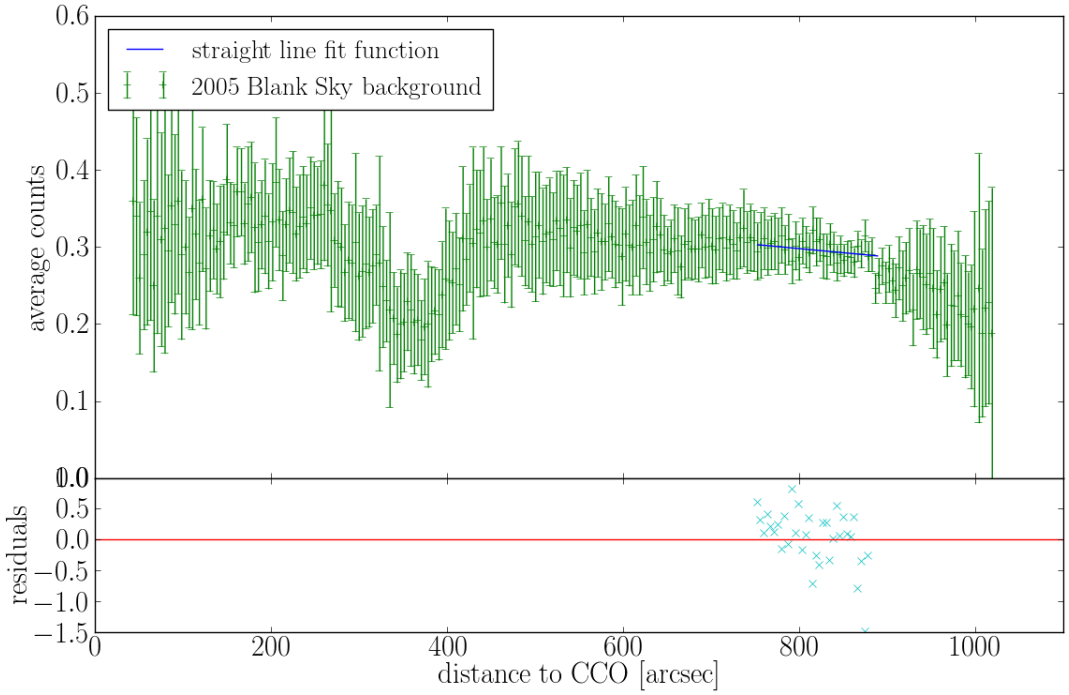

(a) Average background in the not exposure corrected 2005 *Blank Sky* background image. The fit range is roughly the same range that is used to fit the NW filament in the small circle model.

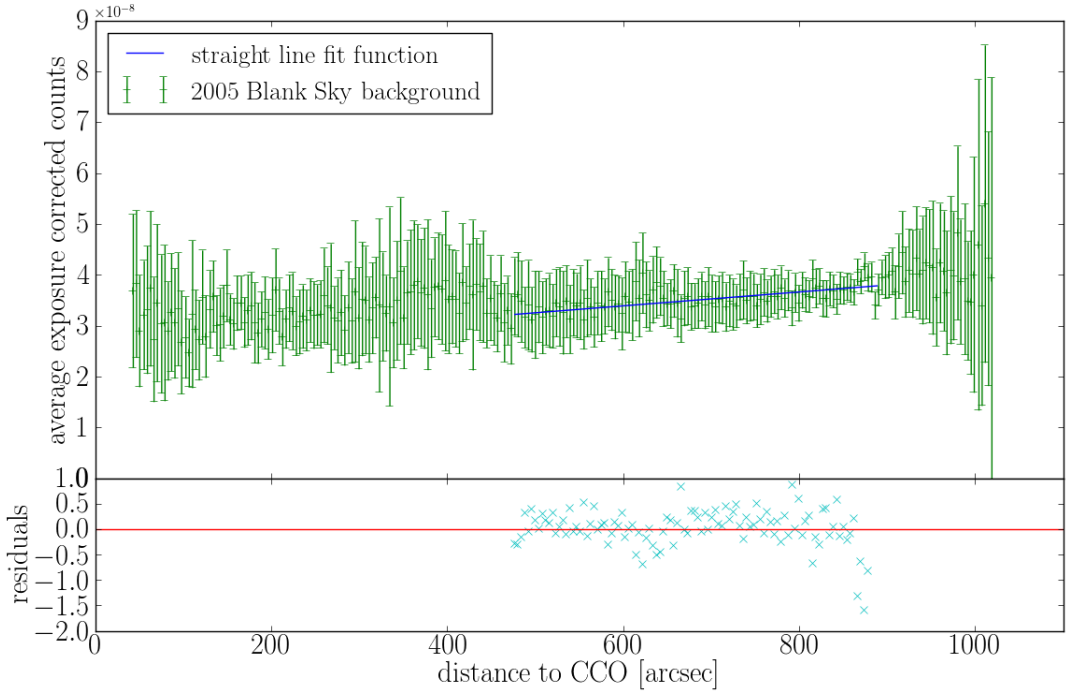

(b) Average background in the exposure corrected 2005 *Blank Sky* background image. The fit range is the same range that is used to fit the NW filament in the big circle model.

Figure 6.4: Average background in the 2005 *Blank Sky* background image with one exposure corrected and the other not. The background data was collected with the big circle model for the NW model from table 6.2. The background was fitted with a straight line in the fit range for the radius used to fit the NW filament in the small circle and in the big circle model.

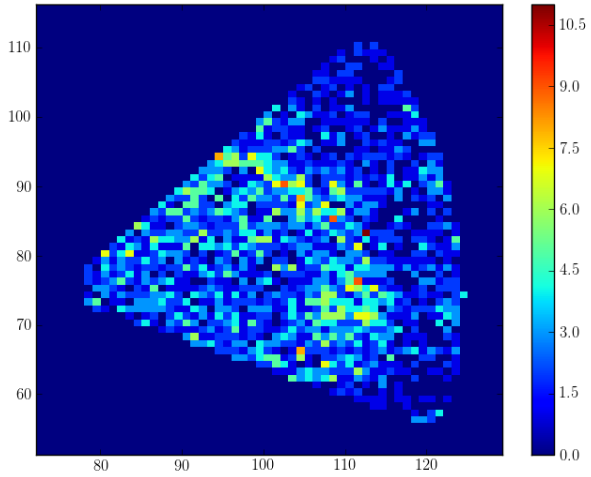

(a) Fit region for filament near CCO in *VFAINT* exposure corrected image.

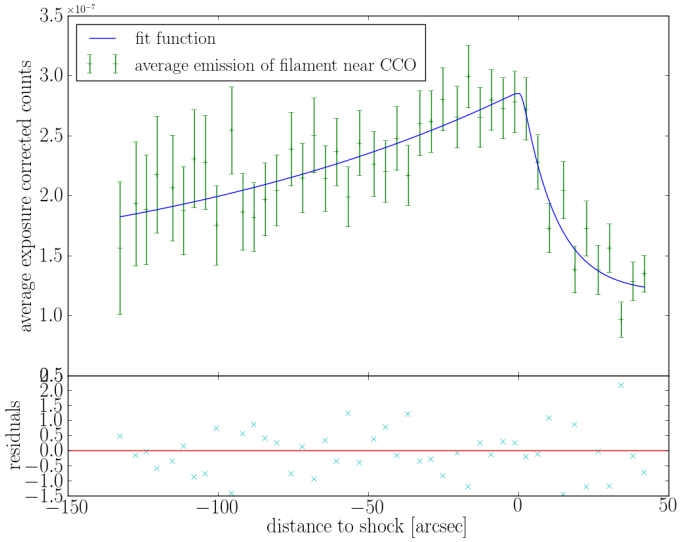

(b) $w_{left} = 136.3''$, $w_{right} = 11.4''$, reduced $\chi^2 = 0.67$.

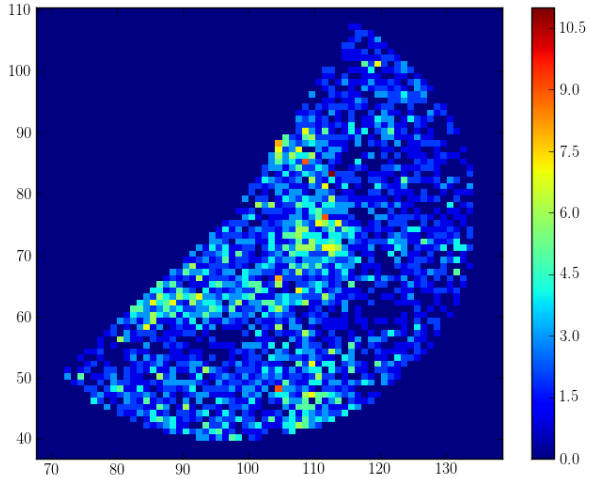

(c) Fit region for filament near CCO in *VFAINT* exposure corrected image.

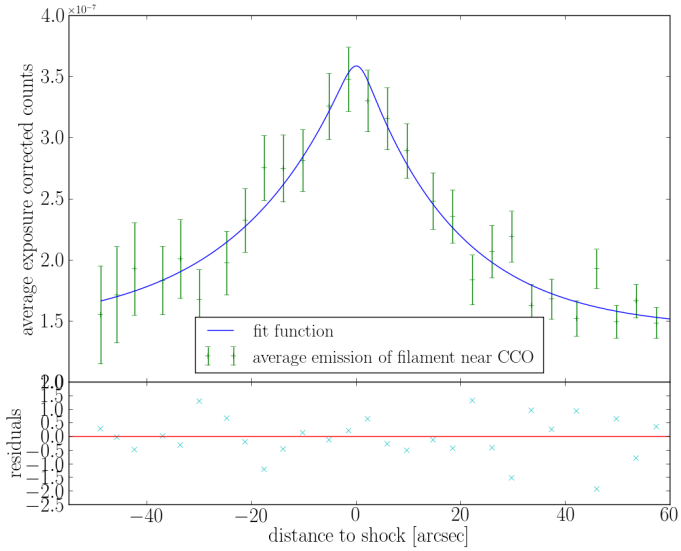

(d) $w_{left} = 21.28''$, $w_{right} = 17.97''$, reduced $\chi^2 = 0.8$.

Figure 6.5: Fit of the shock filament near the CCO with equation 6.6. On the left side of the maximum is the *downstream* side (behind the shock) and on the right side is the *upstream* side (before the shock). In (a) and (b), the fit result when using the results of the *moncar* fit in table 6.2 can be seen together with the fit region. In (c) and (d) the same is shown for using the fit results of the *simplex* fit in table 6.2

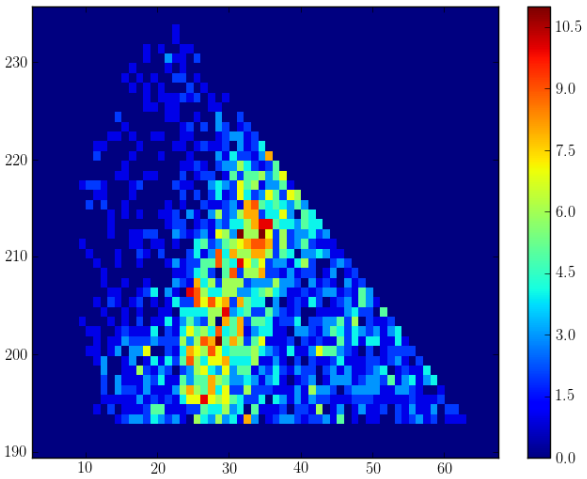

(a) Fit region for NW filament in *VFAINT* exposure corrected image.

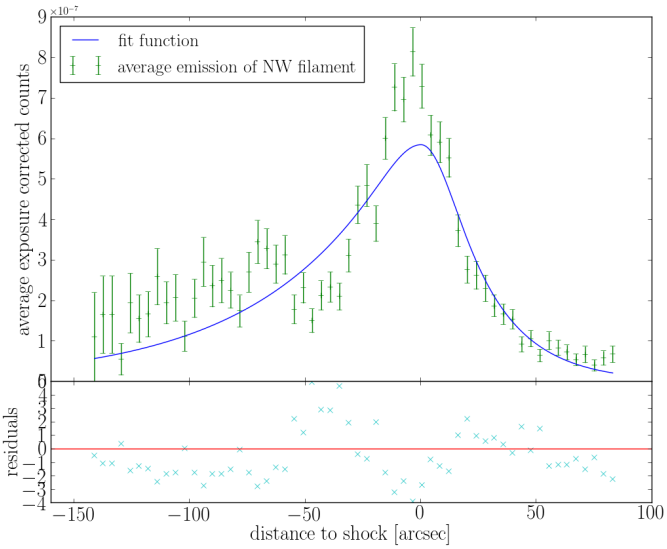

(b) $w_{left} = 57''$, $w_{right} = 22.2''$, reduced $\chi^2 = 4.05$.

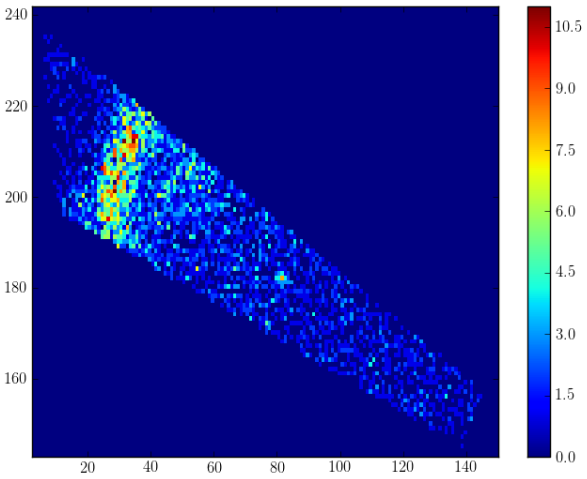

(c) Fit region for NW filament in *VFAINT* exposure corrected image. The circular shape of the filament is deformed due to the different range of the axes.

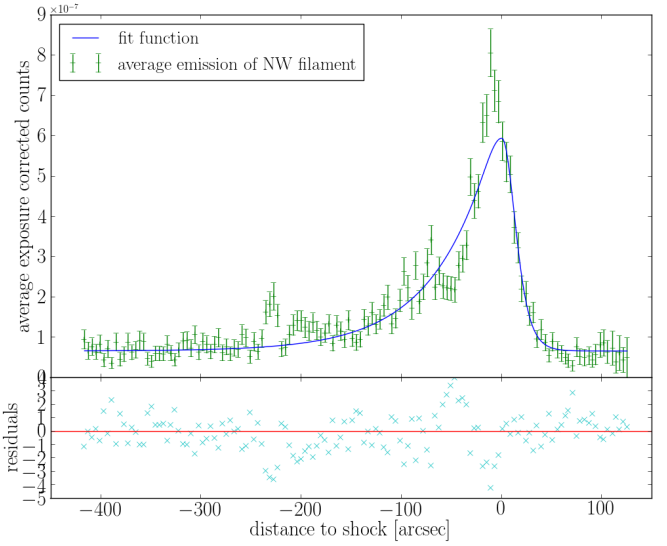

(d) $w_{left} = 58.1''$, $w_{right} = 9.2''$, reduced $\chi^2 = 2.02$.

Figure 6.6: Fit of the NW shock filament with equation 6.6. On the left side of the maximum is the *downstream* side (behind the shock) and on the right side is the *upstream* side (before the shock). In (a) and (b), the fit result for the small circle solution in table 6.2 can be seen together with the fit region. In (c) and (d) the same is shown for the big circle solution in table 6.2.

6.3 Projection Effect on the Image

In the previous section, it was found that an exponential profile, convolved with a Gaussian PSF, is not a good model for the NW synchrotron shock filament since the peak of the emission profile is not represented well. Therefore in this section we use models proposed by Berezhko & Völk (2004) and Ballet (2004).

In section 6.1, two different models for the NW filament with two different centers for the curved profile were found. However, assuming that the NW filament is at the outer shock front of the SNR, it is impossible that the center of the small circle filament is the center of a sphere projected onto the image. Most likely the position of the CCO or near the CCO corresponds to the center of the spherical SNR, as indeed suggested by the best fit "big circle solution" for the NW filament. Therefore it does only make sense to fit a projection formula to the emission profile in the frame of the big circle model.

The projection of the three-dimensional SNR on a image plane can be obtained as shown in figure 6.7, assuming that the distance between the image plane and the SNR is much bigger than the shock radius R of the SNR. The projection is then parallel to the optical axis in z direction and the emission is summed up in the image plane along this direction.

To simulate this, a sphere was first constructed in *Python* with the same size as the models for the filament suggest, and then filled radially symmetric with an exponential profile (see equation 6.4). For the width of the profile the result of Berezhko & Völk (2004) and Ballet (2004) were used. They both found that the intrinsic width of the exponential profile without projection is $\sim 1/7$ of the observed width on the image. Since the profile was fitted separately and it was only tested if the projected profile approximately looks like the measured profile, a width of 50 arc seconds was assumed for the simulated profile, divided by 7. When projecting the sphere, this results in a 7 times wider profile on the image plane, which is 50 arc seconds. This should be in the same range as the width of the observed emission profile. Everything more distanced from the center than the radius was set to zero.

The simulation allows to compare the real data with the simulated projection curve and to determine if

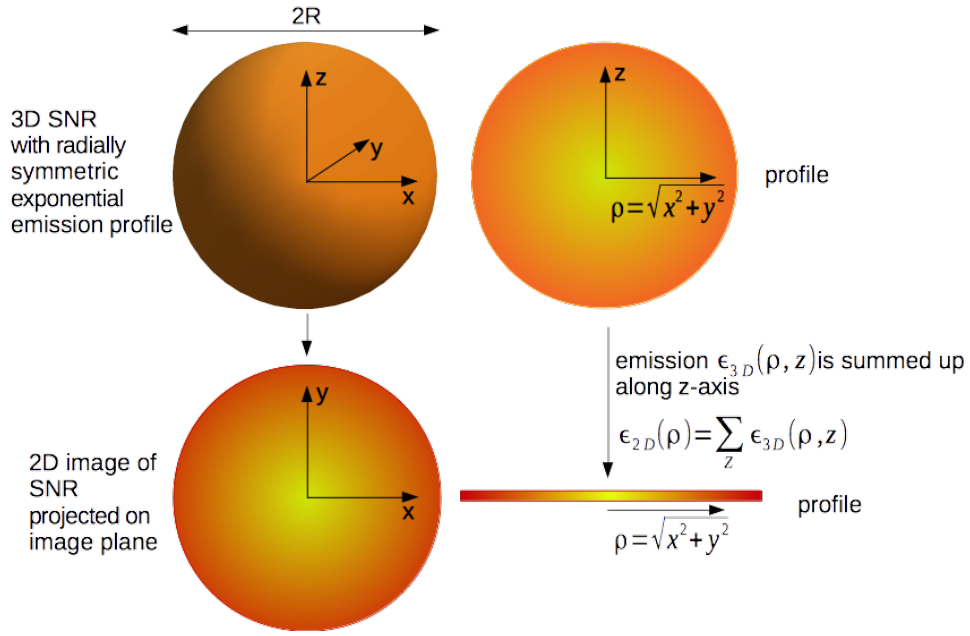

Figure 6.7: The projection of the three-dimensional SNR on a image plane, assuming that the distance between the image plane and the SNR is much bigger than the shock radius R of the SNR. The projection is parallel to the optical axis in z direction and the emission is summed up in the image plane along this direction.

the profile collected with the model of a small circle could be an effect of the projection. To this aim, a big sphere and a small sphere were created and projected on a plane. As shown in figure 6.8, collecting each of these projections with the wrong model widens either the *upstream* or the *downstream* side of the emission profile.

The data for the emission profile to compare with the simulated data was extracted from the exposure

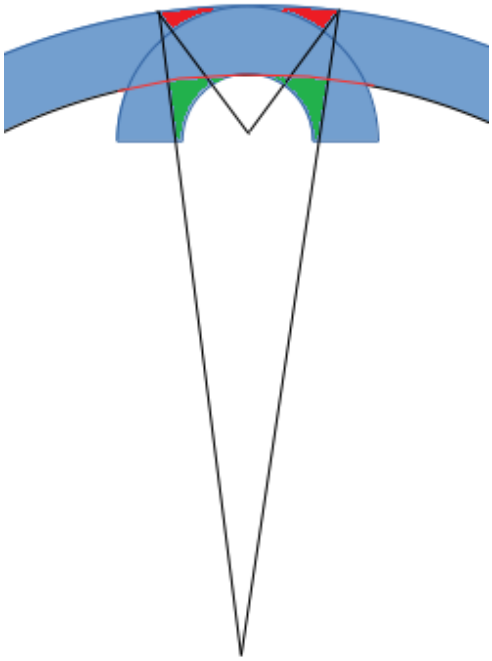

Figure 6.8: The effect of summing up a big or small circle filament with the wrong model. Collecting the small circle filament with a big circle model leads to an increase of emission on the *downstream* region (green), while collecting the data of a big circle filament with a small circle model leads to an increase of emission on the *upstream* side (red).

corrected image, used in section 6.2. For the center of the big circle we used the coordinates of the CCO with $x = 232$, $y = 117$ and a radius of $r = 880''$. These are still within the confidence boundaries of the 2d fit and this also changed the shape of the simulated projection profile even more towards the shape of the image profile. The resulting curves can be seen in figure 6.9. Figure 6.9(a) shows the measured emission together with that of a projected small sphere and a projected big sphere, when all are collected with the model for the small circle. Comparing the *downstream* side, one can see that the choice of model for the simulated data does not have much influence when collecting the data with the small circle model. The curve for the simulated small circle, collected with the small circle also correctly goes to zero at the shock front, as expected from theory. On the *upstream* side however the real data as well as the big circle simulated data collected with the small circle model, both show a wide emission which is not expected in theory. As explained above one would expect some inhomogeneities in the structure of the real data, because it is unlikely for the filament structure to have a perfect circular structure. However, this emission is much too wide to be caused by these inhomogeneities and also in the simulated data such structures should not be present. Therefore this is evidence that the real data is collected with the wrong model, as shown in figure 6.8, and that the measured emission profile, collected with the small circle model, is indeed an effect of the projection.

In figure 6.9(b) the data is collected using the big circle model. In case of the big circle simulation, the collected profile describes the measured data much better on the *downstream* side. However while it is

a good representation of the real data near the shock front, going further away the real data gets lower than the simulated curve. This is most likely due to the not perfect isotropic three-dimensional structure of HESS J1731-347.
For the *upstream* side, as expected from theory, there is no emission present in the curve for the simulated big circle. However the real data shows some emission in this region. Comparing the *upstream* emission in figure 6.9(b) with the one in figure 6.9(a) shows that the proportions are very different. While on the first look the emission seems to have a comparable width, one has to consider that for the big circle model the distance to the center is about 900 arc seconds while in the small circle model the distance is only about 150 arc seconds. Furthermore in the case of the big circle model, because of the smaller curvature, there is much more emission summed up per radius. This way there is easily summed up a lot of emission in the *upstream* region from the inhomogeneous structure of the filament.

The next step was to actually fit the profile with a mathematical model for the projection effect. Berezhko & Völk (2004) and Ballet (2004) already did this and used different fit functions. They both start with a function of the form $f(\rho) = \int_0^a \epsilon(r)dz$ with $\epsilon(r = \sqrt{\rho^2 + z^2})$ as the spherically symmetric emissivity of the SNR and $f(\rho = \sqrt{x^2 + y^2})$ as the surface brightness, being the on the plane projected emissivity profile. The coordinate systems used are shown in figure 6.7. The integral limit a for the height of the sphere is given as $\sqrt{R^2 - \rho^2}$ with R as the shock radius. Both use an exponentially decreasing function of the form $\epsilon(r) = E \cdot \exp((r - R)/w)$ with w as the width of the function.
The difference between their two fit functions comes from the way how they approximated the integral. While Ballet (2004) developed r for ρ close to R, Berezhko & Völk (2004) developed r for z close to a. According to Ballet (2004) this leads to their curve representing the peak better, while the curve of Berezhko & Völk (2004) is more accurate nearer to the center. However, the difference between both curves for the representation of the peak is not big. Since Berezhko & Völk (2004) say that their curve is accurate to about one percent for $w \ll 0.1R$ their function is used for the fit, because like shown in figure 6.6(d) a much bigger range of the profile than just the peak is fitted. The condition of $w \ll 0.1R$ should be fullified here since R is about 900 arc seconds and w should be in the range of 10 arc seconds. The fit function relative to the projection from Berezhko & Völk (2004) is given by

$$f(\rho) = \frac{2ERw}{\sqrt{R^2 - \rho^2}} \left(1 - \frac{R^2 - 2\rho^2}{R^2 z} - e^{-z}\left[1 - \frac{R^2 - 2\rho^2}{R^2 z} + \frac{(z+2)}{2}\left(\frac{2\rho^2 - R^2}{R^2}\right)\right]\right) \tag{6.9}$$

with $z = (R^2 - \rho^2)/(Rw)$.
The emission profile of the NW filament with the CCO as center, fitted with equation 6.9 plus a fit constant, is shown in figure 6.10. We used again the *lmfit* package. The best fit result for the width is $w = 13.29^{+1.64}_{-1.42}$ arc seconds with a reduced χ^2 of $150.5/135 = 1.11$. It is several times smaller than the width gotten in section 6.2. This was expected since the fit in section 6.2 does not consider that the observed profile is a projection. The error is the one sigma confidence interval calculated by *lmfit*.
The first try to fit the projection profile resulted in a reduced χ^2 of $216.8/135 = 1.6$. This is not a very good result, considering that the fit itself when comparing the data and fit curve showed only a few data points where the difference between fit curve and data was several times the error bar. The residuals (see figure 6.10) also show no systematics which indicate a wrong model for the data. A reason for this could be an underestimation of the errors on the measured data. The error is the square root of the exposure corrected counts which is normalized, however these counts are an average over the area shown in figure 6.6(c). As can be seen there, the two dimensional image of the data shows a very inhomogeneous distribution of the events. Therefore taking the average of this region could actually underestimate the error of the individual data points of the shock filament in the *Chandra* image. This would also underestimate the errors of the fit results. Therefore, the errors on the data were enhanced by 20% to consider this. This value was found by trying different enhancements and comparing the χ^2.

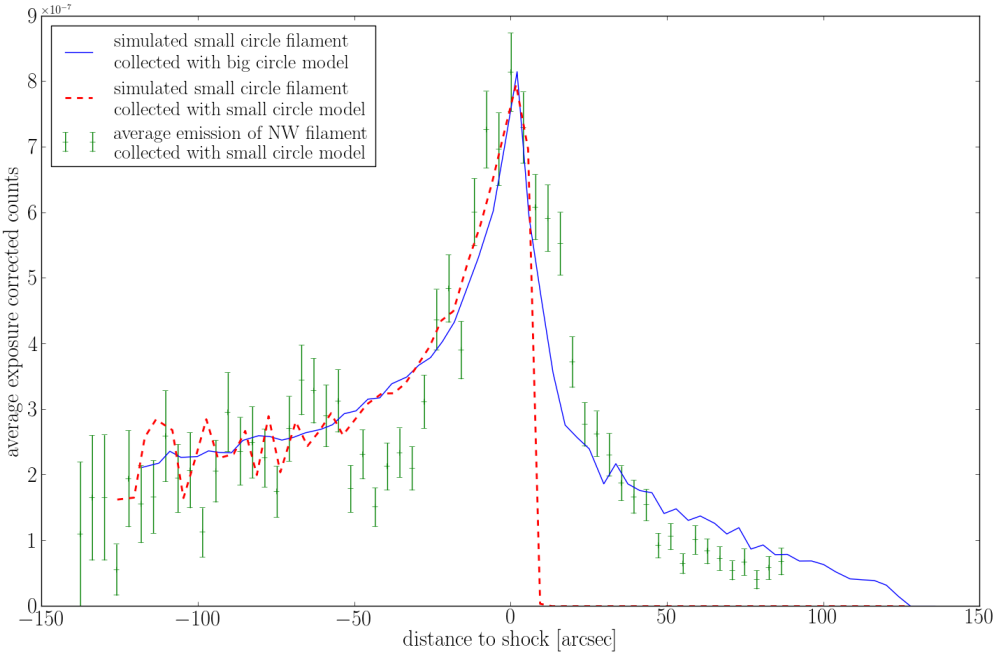

(a) Profiles collected with small circle model. The red dashed line is the profile for a simulated small sphere with the center near the filament projected on the image plane and the blue line is the profile of a simulated big sphere with the center at the CCO. The x-axis shows the full radius of about 150 arc seconds from the maximum to the center.

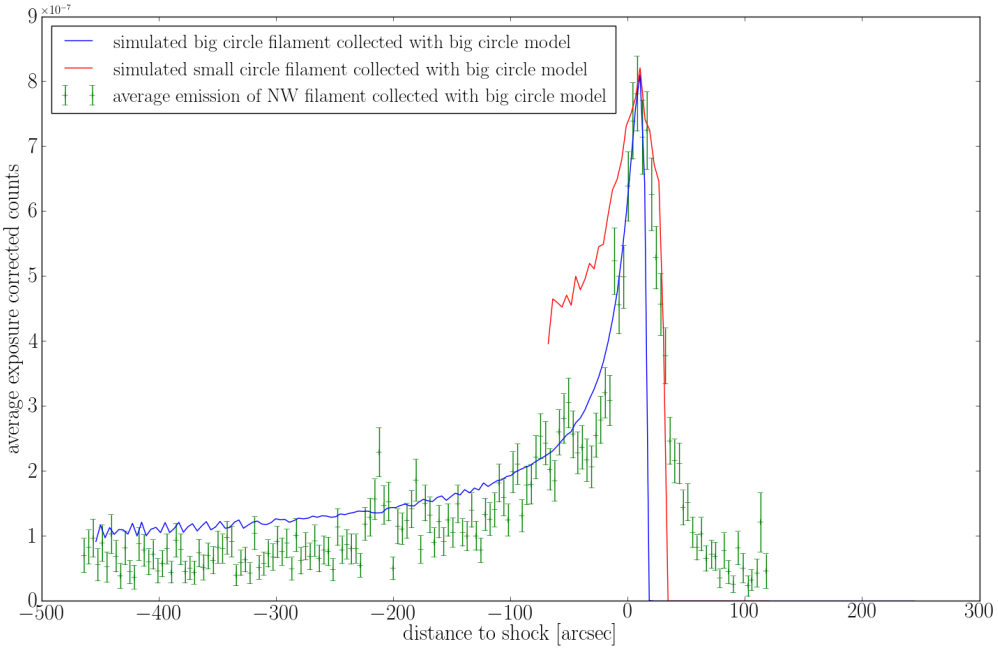

(b) Profiles collected with big circle model. The blue line shows the profile of a simulated big sphere with center near the CCO projected on the image plane and the red line shows the profile of a simulated small sphere. The x-axis shows only 500 arc seconds of the 880 arc second radius from the CCO to the maximum. The curve for the small sphere shows too much *downstream* emission and is obviously the wrong model here.

Figure 6.9: Emission profiles of the NW shock filament collected with the small circle model which has the center near the shock filament and collected with the big circle model which has the CCO as center. For comparison the profiles of simulated big circle and small circle filaments are shown which are collected with the same model as the real data.

Since the fit curve has a very specific form with the rapid decrease towards zero after the peak maximum

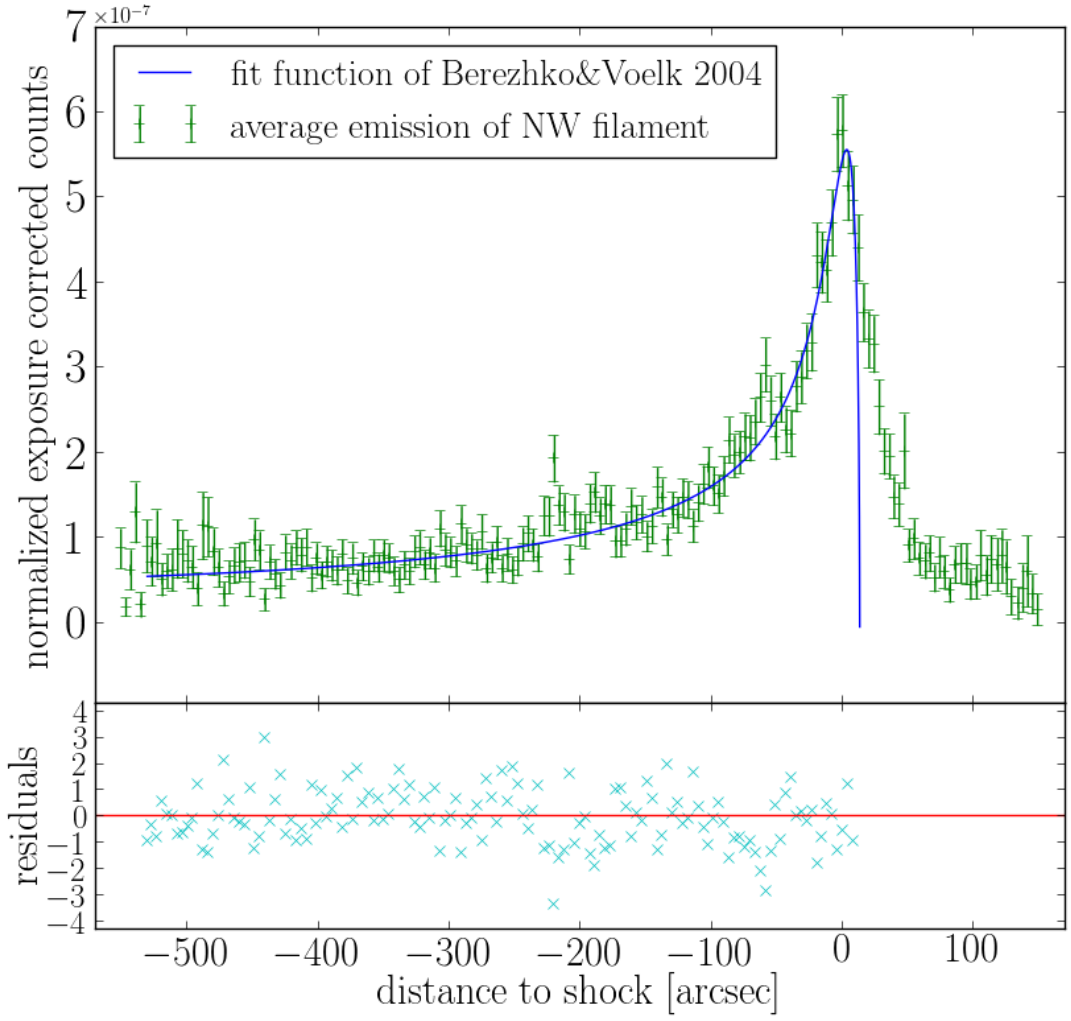

Figure 6.10: Emission profile of the left shock filament with the CCO as center, fitted with the fit function of Berezhko & Völk (2004). Best fit width $w = 13.29^{+1.64}_{-1.42}$ arc seconds, reduced $\chi^2 = 150.5/135 = 1.11$. The residuals are shown in the bottom.

and not considering emission right of the peak, the fitted data had to be limited. Therefore the fit region was selected only up to a few data points right of the maximum, for the curve to be able to find the peak maximum.

The fit constant in this fit is negative with a value of about -5 x 10^{-8} even tough the background is still included in the fitted data. This is similar to the simulated curve seen in figure 6.9(b) where the simulated curve is higher than the measured data nearer to the center. This is most likely due to the fact, that the fit function expects a perfectly isotropic SNR, which is not the case in HESS J1731-347, leading to a slightly different emission curve.

To consider these inhomogeneities, a second fit of the emission profile was done, using only data near the peak maximum for the fit. As already mentioned in section 6.1, and also visible in figure 6.10 as a little peak, there is a structure directly behind the northern part of the NW filament. Under the assumption that this structure is not part of the filament, the distance of about 70 arc seconds from the filament's

peak maximum to this structure was used as a scale for the inhomogeneities in the region of the shock front. To stay in a homogeneous region, only about 50 arc seconds to the shock front were used for the fit, which does not include the little peak from the other structure. The second fit of the data is shown in figure 6.11. The best fit result for the width is here $w = 10.35^{+1.69}_{-1.39}$ arc seconds with a reduced χ^2 of $12.2/10 = 1.22$. The errors were still enhanced by 20% and no fit constant was used. One can see the effect, also visible in the simulated curve in figure 6.9(b), that the theoretical curve is higher than the measured data in regions far away from the shock front. Therefore this seems to be the better fit and the lower width obtained here is used for the calculation of the lower limit on the magnetic field strength at the shock front of HESS J1731-347 in the next chapter. In these fits, the fit function was not convolved

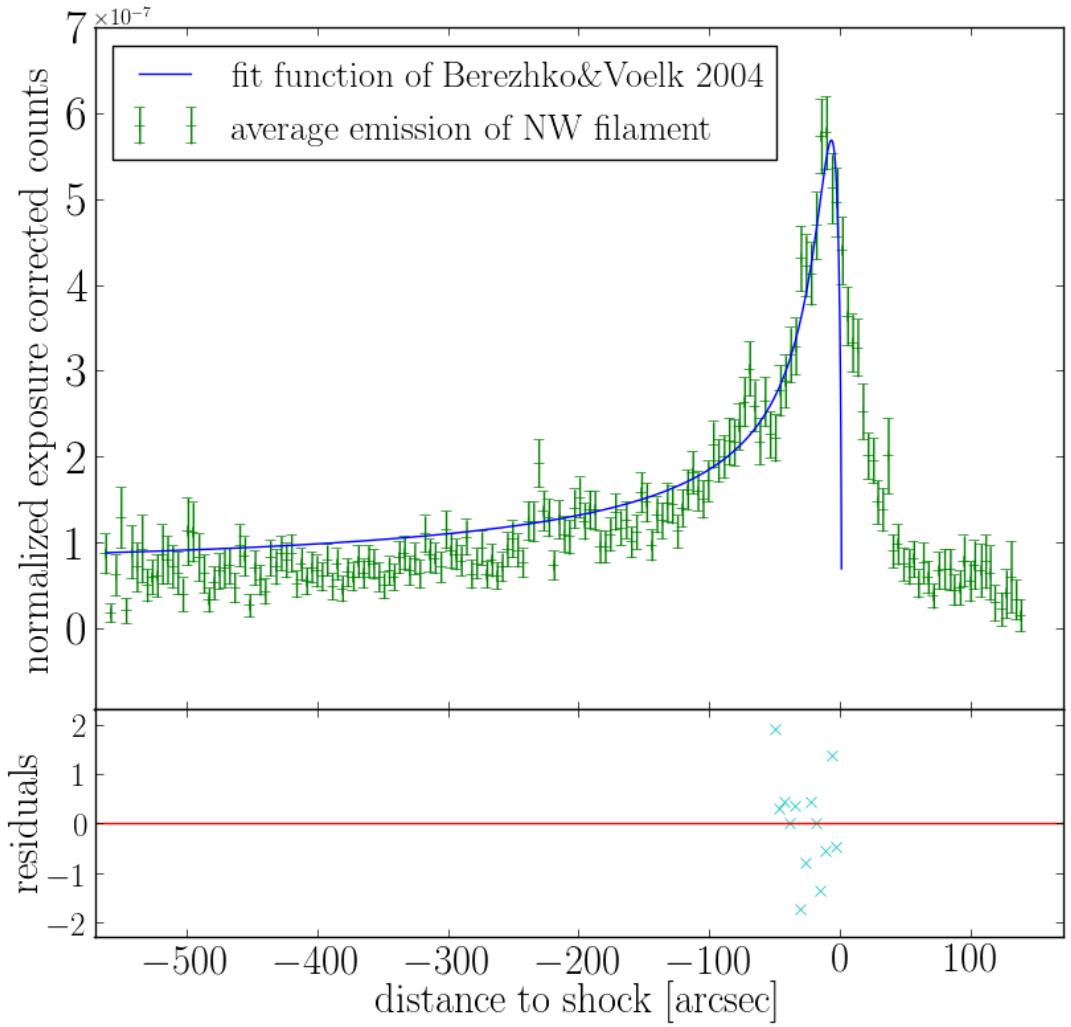

Figure 6.11: Emission profile of the left shock filament with the CCO as center, fitted with the fit function of Berezhko & Völk (2004). Here only the data up to a distance of about 50 arc seconds to the shock front is used. Best fit width $w = 10.35^{+1.69}_{-1.39}$ arc seconds, reduced $\chi^2 = 12.2/10 = 1.22$. The residuals are shown in the bottom.

with the PSF. The Gaussian PSF with a width of about 10 arc seconds and the projection curve plotted with the best fit parameters can be seen in figure 6.12. It can already be seen that the PSF is much less wide than the projection curve. Knowing from the fit in figure 6.11 that the width is 10.35 arc seconds,

it can be estimated that the width of the projected peak is in the range of 70 arc seconds, since the fitted width is about 1/7 of the projected width. The width of the PSF as standard deviation is given at the height of about 0.6 times the amplitude. This gives a FWHM/2 of 11.8 arc seconds for σ=10 arc seconds. The projection curve in equation 6.9 is calculated from an exponential curve. Assuming the projection curve as an exponential curve with a width of 70 arc seconds gives a FWHM/2 of 48.5 arc seconds. Comparing these two numbers, it is unlikely that the influence of the PSF on the emission curve is higher than the confidence intervals on the best fit result for the width. In case of two gaussian functions which are convoluted, the new width in this case would be given as $\sqrt{48.5^2 + 11.8^2} = 49.9$. Even if the PSF would have a significant influence on the width of the curve, it would be no problem when calculating a lower limit on the magnetic field on the shock front using the width of the curve. The limit gets lower if the curve gets wider, therefore it is impossible to overestimate the lower limit by not considering the PSF.

On the *upstream* side, less wide than the *downstream* side and in which no emission curve should be present, the PSF could have a noticeable influence. However, the emission on the *upstream* side is still too wide to be only caused by the PSF. It is theoretically possible to see synchrotron emission on the *upstream* side, if particles leave the shock on the *upstream* side. However this is not possible for electrons but only for heavier particles like protons and this emission region would only be up to about 0.1 pc wide (Ballet 2004), which corresponds to about 6.5 arc seconds here for a distance of 3.2 kpc. In figure 6.11 the width of the curve in the *upstream* region is several times this value.

Since the projection curve in equation 6.9 is imaginary in the *upstream* region due to the $\frac{1}{\sqrt{R^2-\rho^2}}$ part, the convolution of the projection and the PSF would still be imaginary on the *upstream* side and could not be used for fitting. It is also not possible to fit the part of the curve right of the peak maximum with just a gaussian PSF, since as seen in figure 6.12 the peak maxima of both curves are not at the same position, even when using the same center coordinate. In figure 6.12 it can be also seen, that the PSF is by far not wide enough to be alone responsible for the wide *upstream* emission. By simulating a big circle filament like explained above and adding an *upstream* emission, it was made sure that the emission in the *upstream* region is also not a projection effect of an emission curve with a width of 0.1 pc on the *upstream* side caused by particles radiating there. This would not lead to such a wide curve. One of the reasons for a deviation from the theoretical curve on the *upstream* side apart from the PSF and an *upstream* synchrotron emission could be the not perfectly spherical shape of the shock front. This makes the curve wider on the *upstream* side when collecting the data. This not perfectly spherical shape could for example originate from small-scale density inhomogeneities of the surrounding interstellar medium (Berezhko & Völk 2004). In Berezhko & Völk (2004) a similar curve with also emission on the *upstream* side was found for Cassiopeia A. Another reason which could also lead to a not perfectly spherical shape when collecting the data for the fit, is the uncertainty in the center coordinate. Here exactly the CCO coordinates were assumed as the center, since they show better results for the emission curve compared with the projection as the originally found coordinates in the two dimensional fit and also it is assumed that the shock originated from the position of the CCO. However the same argumentation as with the PSF can be applied here: The emission profile can only get wider by collecting the data with another center than the correct one. This makes it impossible to overestimate the lower limit on the magnetic field.

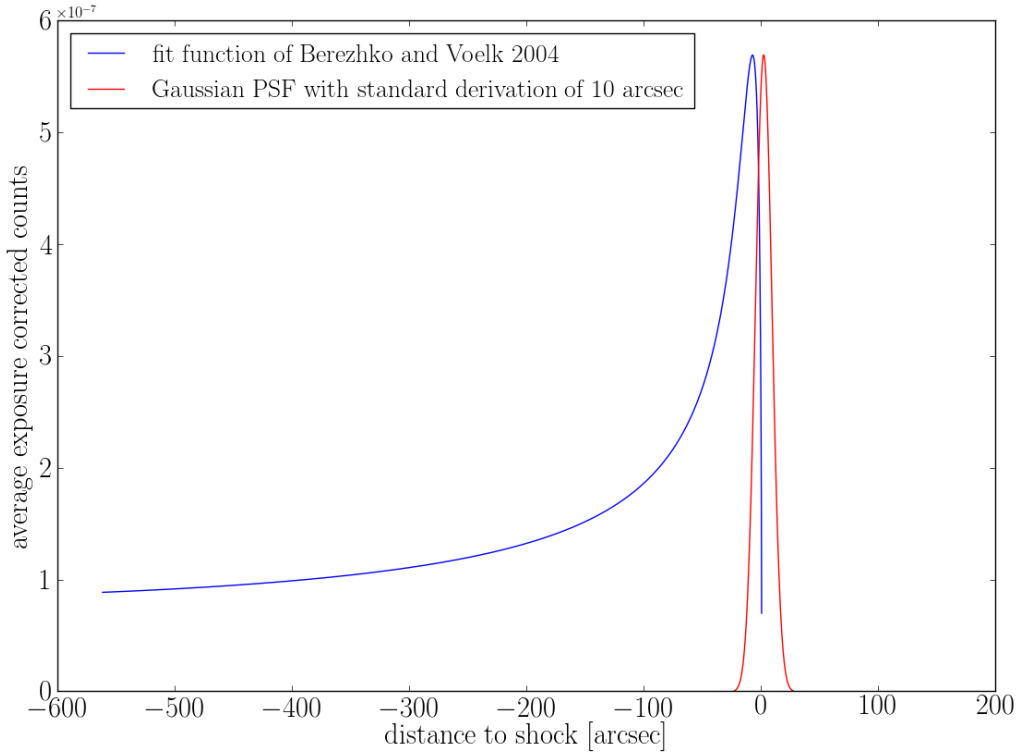

Figure 6.12: Fit function used in the fit of the emission profile plotted with the best fit parameters. For comparison also the gaussian PSF is plotted with a width of 10 arc seconds and the same center as the fit function.

Chapter 7

Results

7.1 A lower limit on the magnetic field strength at the shock front

All the work done up to now aims at estimating the width of the shock filament at the shock front of SNR HESS J1731-347. The best fit value for the width obtained, considering the effect of the three dimensional SNR being projected on a two dimensional image, is $w = 10.35^{+1.69}_{-1.39}$ arc seconds. This value can be used to get a lower limit on the magnetic field strength at the shock front. A limit significantly higher than the $\sim 12\mu$G originating from a compression of the interstellar medium by factor 4 due to the shock wave at the shock front is needed to accelerate cosmic rays up to the *knee* in the comic ray spectrum (Bell et al. 2013). According to theory, magnetic field amplification is due to cosmic rays escaping the shock in the *upstream* region (Ellison 2000), and especially protons because of their large gyroradius (Bell et al. 2013). An amplified magnetic field strength, higher than 12μG, would therefore provide evidence that it is possible, in HESS J1731-347, to accelerate hadronic cosmic rays at the shock front.
In this chapter a lower limit on the magnetic field strength is calculated in different ways and the results compared with that of other SNR. The calculation is based on the principle of accelerated high energy electrons radiating synchrotron in the amplified magnetic field at the shock front. While they move away from the shock front, they radiate and loose energy, as seen in the resulting emission curve in figure 6.10. The electron motion is a combination of diffusion (see section 4.5) and advection (electrons and shock move relatively away from each other) and it is expected that both effects are of the same order for loss-limited electrons (Ballet 2004). Loss-limited means that the loss time

$$\tau_{loss} = \frac{3m_e^2c^3}{4\sigma_T U_{mag} E_0} \tag{7.1}$$

is less than the acceleration time of the electrons. While this equation is for one electron, the emission curve in figure 6.10, which is the exponential emission curve at the shock front projected on the image, is the combined X-ray synchrotron emission of a ensemble of electrons with different energies. However as introduced in section 4.7 the calculation here will be done under the assumption of mono-energetic electrons. *Chandra* has a limited energy range for detecting the radiation. Therefore the width of the curve, which gives the width at 1/e of the maximum, is used as a length scale for the distance to the shock front where only a fraction of 1/e of the electrons have enough energy left for radiating synchrotron detectable by *Chandra*. The loss time τ_{loss} can be used as a time scale for this to occur. Since τ_{loss} depends on the magnetic field strength B, because of $U_{mag} = \frac{B^2}{2\mu_0}$, and the loss time and the width of the curve are connected by the speed of the electrons, they can be used to calculate a lower limit on the

magnetic field strength at the shock front. The result hereby depends on how the electron moves away from the shock front. In Rottenanger (2013) the magnetic field was calculated in the pure advection case. However, as stated above, the movement of the electrons most likely also includes diffusion. This is considered in Berezhko et al. (2003). They used the result of the one-dimensional transport equation for the cosmic ray distribution function under the assumption of a plane shock and the steady state case, which is given as (Berezhko et al. 2003)

$$f_i(x,p) = f(x=0,p)\exp\left(-\frac{|x|}{l_i}\right). \tag{7.2}$$

This function describes the distribution of the cosmic rays with momentum p in the *upstream* ($i = 1$ and $x < 0$) and the *downstream* region ($i = 2$ and $x > 0$). In the mono-energetic case this is independent of p and just describes the exponential distribution at the shock front for a specific electron energy. The width l_i of the curve is given by

$$l_i = \frac{2\kappa_i}{u_i}\left[1-(-1)^i\sqrt{1+\frac{4\kappa_i}{u_i^2\tau_i}}\right]^{-1} \tag{7.3}$$

with κ_i as the cosmic ray diffusion coefficient for electrons in the Bohm limit (see section 4.5) $\kappa(p) = \frac{vpc}{3eB}$ (Berezhko & Völk 2007) where e is the electron charge, v the particle velocity and p the momentum of the particle. The quantity u_i is the relative plasma speed with respect to the shock front and τ_i is the loss time of the cosmic rays. Cosmic ray electrons mainly suffer synchrotron losses (Berezhko et al. 2003) and τ_2 for the *downstream* side is therefore the same loss time as in equation 7.1. For electrons, equation 7.2 describes the same curve as the X-ray synchrotron emission curve in case of a specific electron energy E_e: At $x = l_2$, only 1/e of the electrons with initially momentum $p_e \sim E_e$ still have this momentum due to synchrotron losses. Therefore both the synchrotron and the comic ray distribution have about the same width in case of electrons and the width in equation 7.3 can be treated as the width of the synchrotron curve in figure 6.10.

For the *downstream*, side equation 7.3 can be written as (Berezhko & Völk 2004)

$$l_2 = \frac{2l_{d2}}{\sqrt{1+\frac{4l_{d2}}{l_{c2}}}-1} \tag{7.4}$$

with $l_{d2} = \kappa(p)/u$ as the diffusion length and $l_{c2} = \tau(p)u$ as the convection length. The velocity of the *downstream* plasma with respect to the shock front is $u = V_s/\sigma$, the shock speed V_s divided by the compression ratio σ. The loss time is $\tau(p) = 9m_e^2c^2/(4r_0^2B^2p)$ with m_e as the electron mass and r_0 is the classical electron radius.

The characteristic synchrotron frequency of radiation by an electron is (Ballet 2004):

$$\nu_{sync} = 1.82\cdot 10^{15} B_{\mathrm{mG}} E_{\mathrm{erg}}^2 \mathrm{Hz} \tag{7.5}$$

Using this relation as $\nu \propto Bp^2$, equation 7.4 can be written as

$$l_2 = \frac{\sqrt{\kappa\tau}}{\sqrt{1+\delta^2}-\delta} \tag{7.6}$$

with

$$\delta^2 = \frac{l_{c2}}{4l_{d2}} = 0.12\left(\frac{c}{r_0\nu}\right)\left(\frac{V_s}{\sigma c}\right)^2. \tag{7.7}$$

By inserting the loss time τ and the Bohm diffusion coefficient κ into equation 7.6 and solving it to B, one gets for the *downstream* magnetic field B_d (Berezhko & Völk 2004)

$$B_d = \left(\frac{3m_e^2c^4}{4er_0^2l_2^2}\right)^{1/3} (\sqrt{1+\delta^2} - \delta)^{-2/3}\mathrm{G}. \tag{7.8}$$

Equation 7.8 is valid when both diffusion as well as convection are involved to a fair amount. However, there are two extreme cases possible where mainly only one of the processes is involved. Which one of these three cases applies depends on the value of δ^2.

In the case of very strong losses is $4l_{d2} \gg l_{c2}$ (Berezhko & Völk 2004). It means that the electrons already lose much energy during the acceleration process when they diffuse away from the shock in the *downstream* region. Since this happens very fast, the shock nearly stays at the position where it was when the electron moved through it and the convection does not have much influence here. With the diffusion length being much bigger than the convection length, $\delta \approx 0$ and $l_2 \approx \sqrt{\kappa\tau}$, which means for the *downstream* magnetic field:

$$B_{d,\text{strong losses}} \approx \left(\frac{3m_e^2c^4}{4er_0^2l_2^2}\right)^{1/3} \mathrm{G} \tag{7.9}$$

Because of Bohm diffusion, this result depends not on the particle energy and is also independent of the shock velocity and compression ratio. This is expected, since in the case of strong losses, the shock does not move far while the electrons loose their energy.

The other extreme case is given for very weak losses when $4l_{d2} \ll l_{c2}$. Then the emission curve is a result of the shock and electrons moving away from each other relatively because of the shock moving away from the electrons, while the electrons slowly lose their energy. This happens after the acceleration, when the electrons are not longer accelerated and therefore the diffusion movement during the acceleration and also afterwards has nearly no influence here. With $4l_{d2} \ll l_{c2}$, it can be seen from equation 7.4, by doing a Taylor approximation, that in this case $l_2 \approx l_{c2} = \tau u = \tau\frac{V_s}{\sigma}$. By combining the loss time τ and the typical synchrotron frequency from equation 7.5 the *downstream* magnetic field can then be calculated as:

$$B_{d,\text{weak losses}} \approx \left(\frac{l_{2,\text{pc}}}{1.8\cdot 10^{-}3\cdot E_{\text{keV}}^{1/2}\cdot\frac{V_{s,1000}}{\sigma}}\right)^{-2/3} \mathrm{mG} \tag{7.10}$$

The width of the curve $l_{2,\text{pc}}$ is used here in units of pc instead of cm like in the equations 7.8 and 7.9. $V_{s,1000}$ is the shock speed in units of 1000 km/s.

The resulting magnetic field strength at the shock front of HESS J1731-347 for the three cases explained are shown in figure 7.1. The distance used to calculate the width of the filament was $d = 3.2$ kpc (Abramowski et al. 2011). An estimated error of 0.5 kpc was used. With this, the width of the filament was calculated trigonometrically with the fitted width l_2 as $l_{2,\text{pc}} = d \cdot \sin(l_{2,\text{arcsec}})$. The fitted lower and upper limit on the width was used as an average error of 1.54 arc seconds. In equation 7.8 and 7.10, the synchrotron energy is used for the calculation of the magnetic field strength. The energy is the peak energy of the synchrotron spectrum fitted in figure 5.8, representing the energy of the mono-energetic electrons, about 1.75 keV. The last parameter needed for the calculation is the shock velocity. However, this has not been measured yet. Therefore a range of 1000 km/s to 5000 km/s, in steps of 1000 km/s, has been used here. These are typical shock velocities in supernova remnants.

In Abramowski et al. (2011), a shock velocity of 3000 km/s was calculated, following Truelove & McKee (1999), by estimating the density of the surrounding medium of HESS J1731-347. It is also possible to calculate a shock velocity using the Sedov-Taylor solution, describing the propagation of a blast wave during the second phase of the SNR evolution (see section 4.2). The radius of the SNR as a function of

the time t is then given as (Taylor 1950)

$$R(t) = S(\gamma)\frac{E_0}{\rho_0}^{1/5} t^{2/5} \tag{7.11}$$

with E_0 as the energy released by the supernova explosion, $S(\gamma)$ as a function of the specific heats ratio and ρ_0 as the density of the medium. This was done in Fukuda et al. (2014), where they calculated a shock velocity of 2100 km/s, assuming a distance of 5.2 kpc and using the same density of the surrounding medium as in Abramowski et al. (2011). Both results are in the velocity range selected for the calculation of the magnetic field value. Comparing the results of the different models in figure 7.1, it can be seen

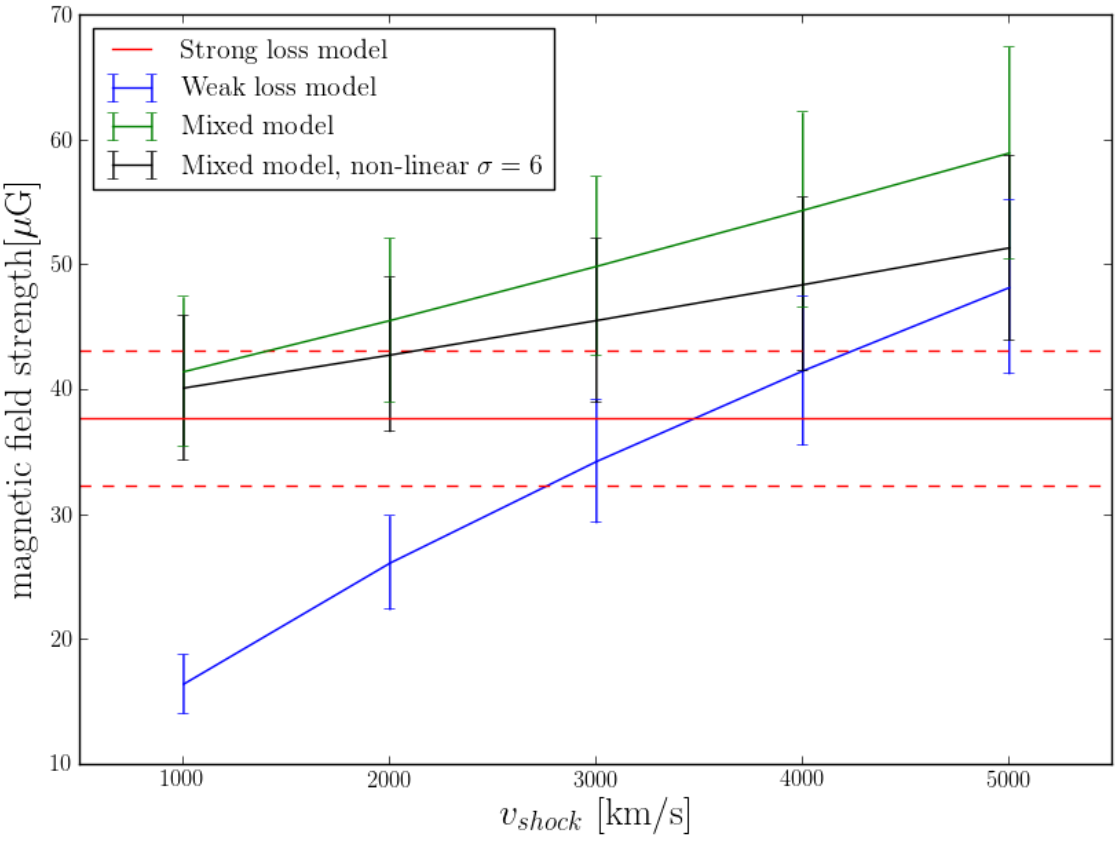

Figure 7.1: Lower limit for the magnetic field strength at the shock front of HESS J1731-347 if the distance is 3.2 kpc. The case of strong losses, weak losses and also the case where both diffusion and convection are involved (mixed case) are shown in dependance of the shock velocity. Also for assuming a non-linear shock compression at the shock front a mixed case curve is shown calculated for a non-linear shock compression ratio of 6.

that the difference in field strength depends strongly on the shock velocity. Like explained above, the result of the strong loss model is independent of the shock velocity and therefore constant. In case of the weak loss model, for small velocities the magnetic field strength is much lower than for the strong loss model, but for the high velocities the value gets higher than that of the strong loss model. This can be explained by the fact that the length scale for the losses is constant. While the strong loss model is not influenced by the velocity, with the weak loss model, a shorter electron loss time and therefore stronger losses, implying a stronger magnetic field, are needed to achieve the same length scale with a higher shock

velocity.
The results of the mixed model, including both convection and diffusion, are for all shock velocities higher than for the strong and weak loss model. However, the curve shows similarities to the explanation above, with the results being nearer at the strong loss model for low velocities and being nearer at the weak loss model for the high shock velocities. This shows the smaller influence of the convection at low velocities and the lower influence of diffusion for higher shock velocities.
The magnetic field values suggest that the magnet field is amplified at the shock front. Even for a shock velocity of 1000 km/s the value of the weak loss model minus the statistical uncertainty gives a value slightly higher than 12 μG. This is however much lower than the estimated shock velocity for a distance of 3.2 kpc, which gives a lower limit of 34.4 μG for 3000 km/s in case of the weak loss model. For the mixed model and a shock velocity of 3000 km/s, the lower limit could be higher than 50 μG within the statistical uncertainty for a distance of 3.2 kpc.
The length scale for the losses given in arc seconds is very sensitive to the distance of HESS J1731-347. As stated above a recent calculation of Fukuda et al. (2014) shows that the distance of HESS J1731-347 could be 5.2 kpc. However, since $B \propto l_2^{-2/3}$ the influence of the difference in distance on the magnetic field value is not that big. The results for a distance of 5.2 kpc are shown in figure 7.2. For the distance, again a uncertainty of 0.5 kpc was assumed. The curves for the different models in figure 7.2 show the same characteristics and shapes as the curves in figure 7.1, but the lower limit for the magnetic field strength is lower. For a shock velocity of 2100 km/s the lower limit for the weak loss model is still higher than 17 μG even within the statistical uncertainty. Therefore even with a bigger distance of 5.2 kpc the results still show the possibility for amplification of the magnetic field strength at the shock front.
It is not known which one of these 3 models is the most precise to describe the loss process in HESS J1731-347 at the shock front. However, the limits given above are the ones for the model giving the lowest magnetic field limit for the estimated shock velocities. Assuming one of the other models as the best match for HESS J1731-347 would lead to an even higher lower limit for the magnetic field strength at the shock front.
The compression ratio of 4 assumes a linear shock compression. It is expected however, that the shock acceleration of comic rays in SNR shocks happens nonlinearly (Ellison 2000). In this case, the shock compression is nonlinear due to a modified shock structure caused by the the back pressure of the accelerated particles (Ellison 2000). Assuming a nonlinear compression ratio of 6, like the one chosen in Berezhko & Völk (2004) for Cas A, the calculated results for the lower limit with the mixed model from equation 7.8 can be seen in figure 7.1 and figure 7.2. The strong loss model is independent of the shock compression and in the weak loss model the loss process should not be influenced by the nonlinear effects, since the electrons are already away from the shock front when the losses mainly happen. The weak loss model assumes that the synchrotron loss time is much bigger than the acceleration time. The shock compression in equation 7.8 only influences the plasma and electron velocity in the *downstream* region in the rest frame of the shock. This results in lower magnetic field values compared to the linear shock compression of 4 as seen in figure 7.1 and figure 7.2. For the same length scale of the losses, with a lower electron velocity the loss time is higher. This requires a less high magnetic field strength as seen in equation 7.1.
For other SNRs a lower limit for the magnetic field strength at the shock front was calculated in the same way as in this work in Ballet (2004) and Berezhko & Völk (2004). A comparison of the calculated magnetic field values, together with some properties of the SNR is given in table 7.1. A comparison of the magnetic field values shows that the value calculated for HESS J1731-347 is the smallest among the results. It is more than 10 times smaller than the value calculated in Berezhko & Völk (2004) for Cas A. However, comparing the width of the filaments together with the SNR age to the magnetic field value implies that the magnetic field gets smaller with higher age of the SNR. In this case, HESS J1731-347

follows this trend, being the oldest SNR, if its age is of at least 2500 years. This dependency on the SNR age was also a result of Bamba et al. (2005), where it was suggested that the emission filaments get wider, the older the SNR becomes. Since the filament width is connected with the magnetic field value through the synchrotron loss time, a wider filament leads to a lower magnetic field value.

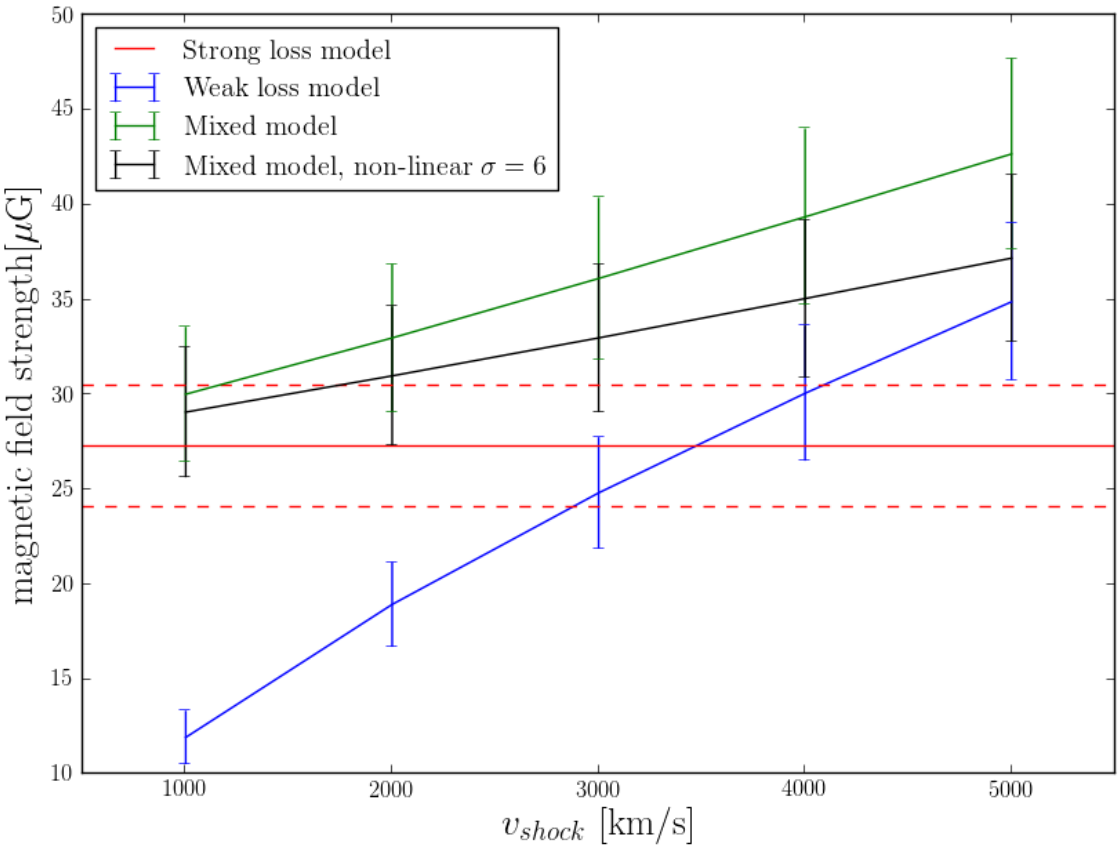

Figure 7.2: Lower limit for the magnetic field strength at the shock front of HESS J1731-347 if the distance is 5.2 kpc.

Table 7.1: Comparison of the in Berezhko & Völk (2004) and Ballet (2004) calculated lower limits for the magnetic field for different SNR with the here calculated limits for HESS J1731-347. The values are taken from the corresponding publications. $E_{\text{X-ray}}$ means the cut-off energy in the synchrotron spectrum and the model is given in the syntax corresponding to the explained models above. The width gives the length scale of the synchrotron losses in the emission profile when considering that the observed profile is a projection. In the case of Berezhko & Völk (2004) the value given is the observed profile width divided by 7 and for Ballet (2004) the observed width is divided by 4.6.

Source	Distance (kpc)	Age (yr)	v_{shock} (km/s)	width (pc)	$E_{\text{X-ray}}$ (keV)	Model	Magnetic field (μG)	From
Cas A	3.4	320	5000	0.0036	2.7	strong loss	470	Berezhko&Völk
Cas A	3.4	320	5200	0.01	1.2	strong loss	230	Ballet
Kepler	4.8	400	5400	0.015	0.9	strong loss	180	Ballet
Tycho	2.3	430	4600	0.01	0.29	strong loss	250	Ballet
SN 1006	2.2	1000	2900	0.04	3	strong loss	87	Ballet
G347.3-0.5	1.3	1620	4000	0.054	2.6	strong loss	79	Ballet
HESS J1731-347	3.2	2500	3000	0.16	1.75	strong loss	37.7	this work
Cas A	3.4	320	3000	0.0036	2.7	mixed, $\sigma = 6$	550	Berezhko&Völk
HESS J1731-347	3.2	2500	3000	0.16	1.75	mixed, $\sigma = 6$	45.6	this work

Chapter 8

Discussion and Outlook

In this work, a lower limit for the magnetic field at the shock front of HESS J1731-347 was calculated for different velocities of the shock front and source distance. This was done by analyzing the X-ray synchrotron emission, observed in a *Chandra* image. The two dimensional fit results as well as the comparison of the simulated emission profiles suggest that the best model for the morphology of the NW synchrotron shock filament is given by a circle with center at the CCO, suggesting that the filament is part of the outer shock front. The comparison of the small circle model, assumed in Rottenanger (2013), with the simulated projection curves showed that this model is not the best one for the filament.
Concerning the X-ray structures near the CCO, the study of the emission profiles projected along an ellipse proposed different possibilities: A very broad filament and therefore a very low magnetic field of less than 12 μG, but also the possibility that the two-dimensional fit of the structures failed, as implied by the residuals, and the data is therefore wrong collected, making it broader. However, the results are not conclusive, since the structures are near the CCO and not at the outer shock front, making unclear what kind of emission profile is expected.
The fit of the NW filament with an exponential profile, convolved with a Gaussian to consider the PSF, showed that this model is not well representing the emission profile projected along a circle. An improved function, which takes into account that the three-dimensional SNR is projected on a two-dimensional image plane, provides a much better model. The model assumes an exponential emission profile at the shock front as intrinsic profile, before it is projected onto the image plane.
The best fit result for the width of the profile is given as $w = 10.35^{+1.69}_{-1.39}$ arc seconds. With this, the lower limit for the magnetic field strength at the shock front was calculated using the model of Berezhko & Völk (2004). For a distance of 3.2 kpc and a calculated magnetic field strength of at least 34.4 μG for a shock velocity of 3000 km/s, it can be concluded that the magnetic field is amplified at the shock front of HESS J1731-347. For a distance of 5.2 kpc however, the results give a magnetic field of only about 19 μG. This is still higher than 12 μG and fulfills the condition for amplification, but the result is not that convincing. The determination of the distance with future measuring is essential. In case of a distance of 3.2 kpc and a shock velocity of 3000 km/s, it can be safely concluded that there are hadronic particles present at the shock front which are accelerated and amplify the magnetic field.
Coming back to question of the origin of the TeV γ-rays observed in HESS J1731-347 introduced in the introduction in chapter 1, this result for the magnetic field strength can now be compared with different models published for the spectral energy distribution, proposing either the leptonic or the hadronic scenario. In Abramowski et al. (2011) a leptonic model was found, requiring a magnetic field strength of 25 μG and a hadronic model with a magnetic field strength of 50 μG. The lower limit for the magnetic field strength calculated in this work is at least in the range of 25 μG and is about 50 μG when assuming the mixed model, including both diffusion and convection, with a linear shock compression of factor 4.

However, according to Abramowski et al. (2011), the hadronic model would need a one magnitude lower shock velocity than 3000 km/s, which would also have a big impact on the results of this work and would result in a decrease of the magnetic field values.
In a recent study of an observation of HESS J1731-347 with *Fermi* was done in Yang, Rui-zhi et al. (2014). The distance assumed by the authors is the same as in Abramowski et al. (2011) (d∼3.2 kpc). The leptonic model requires a magnetic field of about 28 μG, which is very close to the lower limit calculated in this work of 29.3 μG for the weak loss model within the statistical uncertainty and for a shock velocity of 3000 km/s. The hadronic model requires a magnetic field of more than 70 μG, which is slightly higher than the highest lower limit from this work for the mixed model and a shock velocity of 5000 km/s. In Yang, Rui-zhi et al. (2014) it is discussed that for the hadronic model a higher shock velocity is needed, which would be in agreement with the results of this work. However, this would be a problem, because a velocity of 5000 km/s is very high considering the estimated age of HESS J1731-347 and would be more fitting for a very young SNR as seen in table 7.1. The results of this work therefore favor the leptonic scenario, which describes that the origin of the observed γ-rays from HESS J1731-347 is dominated by inverse compton radiation from scattering between accelerated TeV electrons and CMB photons.
One very important, but still unmeasured parameter in all this is the shock velocity. The first *Chandra* observation of HESS J1731-347 used in this work was done in 2008. An observation for example in 2015 would be 7 years later. *Chandra* has the highest spatial resolution of all X-ray telescopes. With 7 years between the observations, the resolution of *Chandra* of about 0.5 arc seconds would be enough to roughly measure the shock velocity in units of 1000 km/s by comparing the two images. One pixel of the *ACIS-I* has also the size of about 0.5 arc seconds. For a distance of the remnant of 3.2 kpc this corresponds to about 0.013 pc. Comparing this value with the distance traveled by the shock in these 7 years, shows that the difference of one pixel for the position of the shock in an unbinned image corresponds to a shock velocity of about 1000 km/s. For two pixels the result would be about 2000 km/s and for three pixels about 3000 km/s. To have the least possible influence of the PSF on the structures, the optical axis of the observation would have to be exactly on the shock position. One problem however could be the PSF of the previous observation of 2008, which has a size of about 10 arc seconds at the position of the shock. While the PSF should only broaden the emission profile and not move the emission maximum that was fitted in this work, the influence of the PSF on the position of the maximum could still be too high, considering that the comparison of the images would be on a length scale of 0.5 arc seconds. Measuring the shock velocity could also help to define a distance. If the result is already 3000 km/s for a distance of 3.2 kpc, it would be unlikely for the distance to be 5.2 kpc with a shock velocity near 5000 km/s, which would be very high given the estimated age of the remnant.

Bibliography

Abramowski, A., Acero, F., Aharonian, F. A., et al. 2011, Astronomy astrophysics, 531, A81

Aharonian, F. A., Akhperjanian, A. G., de Almeida, U. B., et al. 2008, Astronomy astrophysics, 477, 353

Arnaud, K., Smith, D. R., & Siemiginowska, A., eds. 2011, Handbook of X-ray Astronomy (Cambridge Observing Handbooks for Research Astronomers) (Cambridge University Press)

Arnaud, K. A. 1996, 101, 17

Baade, W. & Zwicky, F. 1934, Proceedings of the National Academy of Science, 20, 259

Ballet, J. 2004, in COSPAR Meeting, Vol. 35, 35th COSPAR Scientific Assembly, ed. J.-P. Paillé, 765

Bamba, A., Yamazaki, R., Yoshida, T., Terasawa, T., & Koyama, K. 2005, The Astrophysical Journal, 621, 793

Bell, A. R., Schure, K. M., Reville, B., & Giacinti, G. 2013, Monthly Notices of the Royal Astronomical Society, 431, 415

Berezhko, E. G., Ksenofontov, L. T., & Völk, H. J. 2003, Astronomy & Astrophysics, 412, L11

Berezhko, E. G. & Völk, H. J. 2004, Astronomy & Astrophysics, 419, L27

Berezhko, E. G. & Völk, H. J. 2007, The Astrophysical Journal Letters, 661, L175

Bohm, D., Guthrie, A., & Wakerling, R. K. 1949, McGraw-Hill, 77

Bothe, W. & Kolhörster, W. 1929, Z. Phys., 56, 751

Chandra X-ray Center. 2013, The Chandra Proposers' Observatory Guide, Version 16

Davis, J. E. 2001, The Astrophysical Journal, 548, 1010

Doane, N. 2008, PhD thesis, University of Wisconsin, Madison

Doe, S., Nguyen, D., Refsdal, B., & Siemiginowska, A. 2014, Sherpa: CIAO's modeling and fitting package, `http://cxc.harvard.edu/sherpa4.4/`

Ellison, D. C. 2000, in American Institute of Physics Conference Series, Vol. 528, Acceleration and Transport of Energetic Particles Observed in the Heliosphere, ed. R. A. Mewaldt, J. R. Jokipii, M. A. Lee, E. Möbius, & T. H. Zurbuchen, 383–389

Fermi, E. 1949, Phys. Rev., 75, 1169

Fruscione, A., McDowell, J. C., Allen, G. E., et al. 2006, Society of Photo-Optical Instrumentation Engineers (SPIE) Conference Series, 6270

Fukuda, T., Yoshiike, S., Sano, H., et al. 2014, The Astrophysical Journal, 788, 94

Hardy, J. W. 1998, Adaptive Optics for Astronomical Telescopes (Oxford Series in Optical Imaging Sciences), first edition edn. (Oxford University Press)

Hess, V. F. 1912, Phys. Z., 13, 1084

Hickox, R. C. & Markevitch, M. 2006, The Astrophysical Journal, 645, 95

Inan, U. S. & Golkowski, M. 2011, Principles of Plasma Physics for Engineers and Scientists, har/psc edn. (Cambridge University Press)

James, F. & Roos, M. 1975, Comput. Phys. Commun., 10, 343

Klochkov, D., Pühlhofer, G., Suleimanov, V., et al. 2013, Astronomy & Astrophysics, 556, A41

Longair, M. S. 2011, High Energy Astrophysics, 3rd edn. (Cambridge University Press)

Matthiae, G. 2010, New Journal of Physics, 12, 075009

Nelder, J. A. & Mead, R. 1965, The Computer Journal, 7, 308

Nichols, J. S., Henden, A. A., Huenemoerder, D. P., et al. 2010, The Astrophysical Journal Supplement Series, 188, 473

Pejcha, O. & Thompson, T. A. 2012, The Astrophysical Journal, 746, 106

Rosswog, S. & Brüggen, M. 2007, Introduction to High-Energy Astrophysics, 1st edn. (Cambridge University Press)

Rottenanger, S. 2013, Bachelorarbeit, Universität Tübingen

Schroeder, D. J. 1999, Astronomical Optics, Second Edition, 2nd edn. (Academic Press)

Storn, R. & Price, K. 1997, J. of Global Optimization, 11, 341

Tanaka, T., Uchiyama, Y., Aharonian, F. A., et al. 2008, Astrophys.J., 685, 988

Taylor, G. 1950, Proceedings of the Royal Society of London. Series A. Mathematical and Physical Sciences, 201, 175

Tian, W. W., Leahy, D. A., Haverkorn, M., & Jiang, B. 2008, The Astrophysical Journal Letters, 679, L85

Truelove, J. K. & McKee, C. F. 1999, The Astrophysical Journal Supplement Series, 120, 299

Vikhlinin, A. 2014, REDUCING ACIS QUIESCENT BACKGROUND USING VERY FAINT MODE, `http://cxc.harvard.edu/cal/Acis/Cal_prods/vfbkgrnd/index.html`

Wise, M. W., Davis, J. E., Huenemoerder, D. P., Houck, J. C., & Dewey, D. 2003, MARX 4.0 Technical Manual

Xu, T., Cheng, I., Long, R., & Mandal, M. K. 2013, EURASIP J. Image and Video Processing, 2013, 3

Yang, Rui-zhi, Zhang, Xiao, Yuan, Qiang, & Liu, Siming. 2014, AA, 567, A23

Acknowledgment

I want to thank Andrea Santangelo for letting me continue in the HEA group to do my master thesis. Your support and guidance helped me a lot, especially during finishing the thesis.

Furthermore I want to thank Gerd Pühlhofer and Dmitry Klochkov for supervising my thesis and for helping me when I encountered problems. Sharing your knowledge with me did help a lot and I learned many useful things from you.

Last but not least, I want to thank my family and my fiancée Melanie for their continuous support during my bachelor and master thesis and the rest of the time studying physics, and also for bearing with me during hard times.